

# Important Notice

This copy may be used only for the purposes of research and private study, and any use of the copy for a purpose other than research or private study may require the authorization of the copyright owner of the work in question. Responsibility regarding questions of copyright that may arise in the use of this copy is assumed by the recipient.

UNIVERSITY OF CALGARY

Stability and Accuracy Analysis of Space-frequency Wavefield Extrapolators  
for Depth Migration

by

Kun Liu

A THESIS

SUBMITTED TO THE FACULTY OF GRADUATE STUDIES  
IN PARTIAL FULFILMENT OF THE REQUIREMENTS FOR THE  
DEGREE OF MASTER OF SCIENCE

DEPARTMENT OF GEOLOGY AND GEOPHYSICS

CALGARY, ALBERTA

April, 2005

© Kun Liu 2005

UNIVERSITY OF CALGARY  
FACULTY OF GRADUATE STUDIES

The undersigned certify that they have read, and recommend to the Faculty of Graduate Studies for acceptance, a thesis entitled "Stability and Accuracy Analysis of Space-frequency Wavefield Extrapolators for Depth Migration" submitted by Kun Liu in partial fulfilment of the requirements of the degree of Master of Science.

---

Supervisor, Dr. J. C. Bancroft  
Department of Geology and Geophysics

---

Co-supervisor, Dr. H. D. Geiger  
Department of Geology and Geophysics

---

Dr. G. F. Margrave  
Department of Geology and Geophysics

---

Dr. R. H. Johnston  
Department of Electrical and Computer Engineering

---

Date

## **Abstract**

Stability and accuracy are major concerns when designing recursive wavefield extrapolators implemented in the space-frequency domain. In this thesis, a common set of tools has been developed and utilized to conduct a comprehensive stability and accuracy analysis of selected space-frequency extrapolators. The analysis shows that the Hale extrapolator is superior over a limited-aperture Rayleigh extrapolator spatially tapered by either a Hanning or a Gaussian window. A key merit of the Hale extrapolator is that it preserves as much of the phase and amplitude of the propagating wavefield as possible, yet attenuates propagating waves where the extrapolator has significant phase error.

A new adaptive tapering scheme is proposed and compared with conventional tapering methods using both simple and complex models. The results show that adaptive tapering can be applied in the first extrapolation step to improve the image at shallow depth from a common-source migration.

## **Acknowledgements**

I would like to extend my gratitude to my supervisor, Dr. John C. Bancroft, for his patient guidance and generous help throughout my entire Master study. I also thank my co-supervisor, Dr. Hugh D. Geiger, for his innovative ideas, beneficial comments and strong support of my research. I'm grateful to all the faculty members, staff and students in the CREWES Project and the department who offered tremendous help to me during the past years. The sponsors of CREWES Project are greatly appreciated for their financial support.

Special thanks to Dr. Gary F. Margrave and the POTSI Project who provided the Linux Clusters, Mr. Kevin Hall and Mr. Henry Bland who helped solve computer problems, Dr. Rolf Maier who proofread my thesis, Dr. Yanpeng Mi who made Marmousi dataset available, Mr. Xinxiang Li who is always ready to help, and Dr. Helen Isaac who helped with the data processing.

Finally, I would like to sincerely thank my wife, Tao Cheng, who always supports me and encourages me to overcome all difficulties.

**Dedication**

**To my beloved wife Tao Cheng**

## Table of Contents

Approval Page.....	ii
Abstract.....	iii
Acknowledgements.....	iv
Dedication.....	v
Table of Contents.....	vi
List of Tables .....	vii
List of Figures and Illustrations .....	viii
Chapter One: INTRODUCTION .....	1
1.1 Wavefield extrapolation techniques.....	1
1.2 Stability and accuracy of space-frequency extrapolators.....	3
1.3 Adaptive tapering for the first extrapolation step .....	9
1.4 Contribution of the thesis.....	10
1.5 Structure of the thesis.....	11
Chapter Two: REVIEW OF WAVEFIELD EXTRAPOLATORS.....	12
2.1 One-way wave propagation .....	12
2.2 Rayleigh extrapolator.....	15
2.3 Hale extrapolator.....	22
2.4 Nautiyal extrapolator .....	28
2.5 Common-source migration and imaging condition .....	30
2.6 Chapter summary .....	32
Chapter Three: STABILITY AND ACCURACY OF THREE EXTRAPOLATORS .....	34
3.1 Three extrapolators in the wavenumber-frequency domain .....	34
3.2 Stability analysis .....	37
3.3 Accuracy analysis .....	42
3.4 Zero-offset impulse responses .....	55
3.5 Prestack synthetic test.....	58
3.6 Marmousi synthetic test.....	62
3.7 Computation costs.....	69
3.8 Chapter summary .....	71
Chapter Four: ADAPTIVE TAPERING IN WAVEFIELD EXTRAPOLATION.....	73
4.1 Adaptive tapering for the first extrapolation step .....	76
4.2 Synthetic tests .....	77
4.3 Chapter summary .....	82
Chapter Five: CONCLUSIONS AND FUTURE WORK.....	83
REFERENCES .....	87

### **List of Tables**

Table 1: Tools of stability and accuracy analysis in this thesis and their purposes.....	71
Table 2: Comparison of stability, accuracy and efficiency of various extrapolators. More stars is better. ....	72

## List of Figures and Illustrations

Figure 1.1: Comparison of the images of the 2-D SEG-EAGE salt model from (a) nonrecursive Kirchhoff migration; (b) wavefield-continuation migration based on recursive wavefield extrapolation (Soubaras, 2002).....	2
Figure 1.2: Schematic implementation of a 2-D $x$ - $\omega$ (space-frequency) extrapolation. ....	3
Figure 2.1: (a) Amplitude and (b) phase spectra of the desired extrapolator in the $k_x$ - $\omega$ domain. Wavenumber and phase are normalized by the factors of $2\pi/\Delta x$ and $2\pi$ , respectively. ....	14
Figure 2.2: (a) Amplitude and (b) phase spectra of a 19-point Rayleigh extrapolator in the $k_x$ - $\omega$ domain. The parameters are the same as those in Figure 2.1. ....	20
Figure 2.3: (a) Amplitude and (b) phase spectra of a 19-point Rayleigh extrapolator at the frequency of 31.25 Hz (blue lines). The evanescent boundaries are at $k_x=\pm 0.25$ . The dashed red lines are the amplitude and phase spectra of the desired extrapolator....	21
Figure 2.4: Amplitude spectrum of a 200-point Rayleigh extrapolator at the frequency of 31.25 Hz (blue lines). The close-up of (a) is shown in (b). The evanescent boundaries are at $k_x=\pm 0.25$ . The dashed red lines are the desired amplitude spectrum. ....	21
Figure 2.5: (a) Amplitude and (b) phase spectra of a 19-point Hanning-tapered Rayleigh extrapolator in the $k_x$ - $\omega$ domain. The parameters are the same as those in Figure 2.1. ....	22
Figure 2.6: (a) Amplitude and (b) phase spectra of a 19-point Hanning-tapered Rayleigh extrapolator at the frequency of 31.25 Hz (blue lines). The evanescent boundaries are at $k_x=\pm 0.25$ . The dashed red lines are the amplitude and phase spectra of the	

desired extrapolator.....	22
Figure 2.7: (a) Amplitude and (b) phase spectra of a 19-point Hale extrapolator in the $k_x$ - $\omega$ domain. The parameters are the same as those in Figure 2.1.....	27
Figure 2.8: (a) Amplitude and (b) phase spectra of a 19-point Hale extrapolator at the frequency of 31.25 Hz (blue lines). The evanescent boundaries are at $k_x=\pm 0.25$ . The dashed red lines are the amplitude and phase spectra of the desired extrapolator....	27
Figure 2.9: Phase spectra of a 19-point Hale extrapolator (a) in the $k_x$ - $\omega$ domain and (b) at the frequency of 31.25Hz. All the values outside the evanescent boundaries are zeroed.....	27
Figure 2.10: (a) Amplitude and (b) phase spectrum of a 19-point Nautiyal extrapolator in the $k_x$ - $\omega$ domain. The parameters are the same as those in Figure 2.1.....	30
Figure 2.11: (a) Amplitude and (b) phase spectra of a 19-point Hale extrapolator at the frequency of 31.25 Hz (blue lines). The evanescent boundaries are at $k_x=\pm 0.25$ . The dashed red lines are the amplitude and phase spectra of the desired extrapolator....	30
Figure 2.12: Schematic implementation of a wavefield-continuation migration based on the wavefield extrapolation. (a) Forward extrapolate the source wavefield by modeling; (b) backward extrapolate the receiver wavefield; (c) the horizontal reflector is imaged by applying imaging condition (figure courtesy Bancroft).....	31
Figure 3.1: 3-D plot of various band-limited extrapolators in the $k_x$ - $\omega$ domain. Amplitude spectra are on the left, and phase spectra are on the right. (a) The desired extrapolator (from equation (2.21)); (b) the Hanning edge-tapered Rayleigh extrapolator; (c) the Hale extrapolator; (d) the Nautiyal extrapolator. An operator length of 19 points is used by operators (b), (c) and (d) in the space domain. The	

phase spectrum of the Hale extrapolator is zeroed outside the evanescent boundaries (see discussion in Section 2.3)..... 35

Figure 3.2: 3-D plot of various band-limited extrapolators in the  $k_x$ - $\omega$  domain. The figures on the left are the amplitude spectra and on the right are the phase spectra. (a) The desired extrapolator; (b) the Hanning edge-tapered Rayleigh extrapolator; (c) the Hale extrapolator; (d) the Nautiyal extrapolator. An operator length of 39 points is used by operators (b), (c) and (d) in the space domain. The phase spectrum of the Hale extrapolator is zeroed outside the evanescent boundaries..... 36

Figure 3.3: Amplitude spectra of the Rayleigh extrapolators at the frequency of 31.25 Hz (only positive wavenumbers are plotted). The evanescent boundary is at  $k_x=0.25$ . The dashed red lines are the amplitude spectra of the desired extrapolator. (a) 19-point Hanning-tapered (thick green line) and truncated extrapolator (thin blue line); (c) 39-point Hanning-tapered (thick green line) and truncated extrapolator (thin blue line); (e) full-aperture extrapolator. The figures on the right ((b), (d) and (f)) show the amplification of the wavefield energy after 100 extrapolation steps..... 39

Figure 3.4: Amplitude spectra of the Hale extrapolators at the frequency of 31.25 Hz (blue lines - only positive wavenumbers are plotted). The evanescent boundary is at  $k_x=0.25$ . The dashed red lines are the amplitude spectra of the desired extrapolator. (a) 19-point extrapolator; (c) 39-point extrapolator. Figures on the right ((b) and (d)) show the amplification of the wavefield energy after 100 extrapolation steps..... 40

Figure 3.5: Amplitude spectra of the Nautiyal (Gaussian tapered) extrapolators at the frequency of 31.25 Hz (blue lines - only positive wavenumbers are plotted). Evanescent boundary is at  $k_x=0.25$ . The red dashed lines are the amplitude spectra of

the desired extrapolator. (a) 19-point extrapolator; (c) 39-point extrapolator. Figures on the right ((b) and (d)) are the amplification/attenuation of the wavefield energy after 100 steps extrapolations..... 41

Figure 3.6: Amplitude spectra of the full Hanning-tapered Rayleigh extrapolator at the frequency of 31.25 Hz (blue lines). The evanescent boundary is at  $k_x=0.25$ . The red dashed lines are the amplitude spectra of the desired extrapolator. (a) The 39-point Rayleigh extrapolator; (b) the attenuation of the wavefield energy after 100 extrapolation steps. .... 42

Figure 3.7: Amplitude errors of (a) the full-aperture Rayleigh extrapolator, the 19-point (b) Hanning-tapered Rayleigh extrapolator, (c) Hale extrapolator, and (d) Nautiyal extrapolator. The dashed red lines are the evanescent boundaries. .... 45

Figure 3.8: Phase errors of (a) the full-aperture Rayleigh extrapolator, the 19-point (b) Hanning-tapered Rayleigh extrapolator, (c) Hale extrapolator, and (d) Nautiyal extrapolator. The dashed red lines are the evanescent boundaries. The phase error spectrum of the Hale extrapolator is zeroed outside the evanescent boundaries (see discussion in Section 2.3). .... 46

Figure 3.9: Amplitude errors of (a) the full-aperture Rayleigh extrapolator, the 39-point (b) Hanning-tapered Rayleigh extrapolator, (c) Hale extrapolator, and (d) Nautiyal extrapolator. The dashed red lines are the evanescent boundaries. .... 47

Figure 3.10: Phase errors of (a) the full-aperture Rayleigh extrapolator, the 39-point (b) Hanning edge-tapered Rayleigh extrapolator, (c) Hale extrapolator, and (d) Nautiyal extrapolator. The dashed red lines are the evanescent boundaries. The phase error spectrum of the Hale extrapolator is zeroed outside the evanescent boundaries (see

discussion in Section 2.3). .....	49
Figure 3.11: Amplitude (left) and phase (right) error contours for the 39-point Hanning edge-tapered Rayleigh extrapolator ((a) and (b)), Hale extrapolator ((c) and (d)), Nautiyal extrapolator (e) and (f), and full Hanning-tapered Rayleigh extrapolator. Frequency is normalized by multiplying $\Delta x/v$ . .....	54
Figure 3.12: Impulse responses (zero-offset migration) of (a) the phase-shift operator and (b) the 200-point full-aperture Rayleigh extrapolator.....	55
Figure 3.13: Impulse responses of the 19- and 39-point Hanning edge-tapered Rayleigh extrapolators (a and b), Hale extrapolators (c and d), Nautiyal extrapolators (e and f), and full Hanning-tapered Rayleigh extrapolators (g and h).....	57
Figure 3.14: (a) A constant velocity earth model containing 17 dipping events. For a better comparison, reflectors are symmetric with $x=0$ . (b) Synthetic common-source gather of the model with the source located at $x=0$ . .....	59
Figure 3.15: Migration of prestack synthetic data by using (a) the full-aperture Rayleigh extrapolator, the 39-point (b) Hanning edge-tapered Rayleigh extrapolator, (c) Hale extrapolator, (d) Nautiyal extrapolator, and (e) full Hanning-tapered Rayleigh extrapolator. ....	61
Figure 3.16: Marmousi velocity model. There is also a density model not shown here. .	62
Figure 3.17: Pseudo-reflectivity of Marmousi model. Black arrows indicate the structures that impose challenges to the imaging techniques. The imaging target (reservoir) is denoted by red circle. ....	63
Figure 3.18: Common-source migration of Marmousi dataset using (a) the full aperture (512-point) Rayleigh extrapolator, the 39-point (b) Hanning edge-tapered Rayleigh	

extrapolator, (c) Hale extrapolator, (d) Nautiyal extrapolator and (e) full Hanning-tapered Rayleigh extrapolator. All the figures are displayed using identical scaling values. ....	66
Figure 3.19: Comparison of the major faults of images in Figure 3.18. (a) Pseudo-reflectivity; (b) images from the full-aperture Rayleigh extrapolator; images from the 39-point (c) Hanning edge-tapered Rayleigh extrapolator, (d) Hale extrapolator, (e) Nautiyal extrapolator and (f) full Hanning-tapered Rayleigh extrapolator. ....	68
Figure 3.20: The comparison of image target (reservoir). (a) Pseudo-reflectivity; image from (b) the full-aperture Rayleigh extrapolator and (c) the 39-point Hale extrapolator. ....	69
Figure 3.21: Computation costs of the three extrapolators. ....	70
Figure 4.1: The discontinuities in the first extrapolation step. ....	74
Figure 4.2: (a) Synthetic section padded with zero traces on each side. (b) The wavefield in Figure 4.2a is upward extrapolated using a Rayleigh extrapolator. Without any treatment of the truncations, artifacts occur on the output section. ....	75
Figure 4.3: The effects of conventional tapering. (a) After a Hanning taper to the extrapolator, artifacts 2 have been removed. (b) After applying Hanning tapers to both data and extrapolator, most of the artifacts are removed. ....	75
Figure 4.4: Conventional tapering may cause accuracy loss. ....	76
Figure 4.5: The adaptive tapering schemes that are dependent on the output point locations. ....	77
Figure 4.6: (a) Conventional extrapolation with separate data and extrapolator tapers; (b) Extrapolation with the adaptive taper. In order to make a better comparison, figures	

are displayed with a less clip value (therefore stronger amplitudes) than the one used in Figure 4.3. .... 78

Figure 4.7: The results from first (backward) extrapolation step of a Marmousi common-source gather (shot point at 5000m) with (a) conventional tapering and (b) adaptive tapering. Difference ((b) minus (a)) is plotted in (c). The common-source gather is padded with zero traces on both sides and zeros in the bottom (for fast Fourier transform). .... 80

Figure 4.8: Shallow images of Marmousi dataset generated by (a) conventional tapering and (b) adaptive tapering. Difference ((b) minus (a)) is plotted in (c). All the figures are displayed using identical scaling values. .... 81

## Chapter One: INTRODUCTION

### 1.1 Wavefield extrapolation techniques

In recent years, wavefield-continuation seismic imaging methods<sup>1</sup> have found wide application as computational power has steadily increased and as exploration for oil and gas extends to areas with strong lateral variations in seismic velocity. The essential component of a wavefield-continuation imaging method is recursive wavefield extrapolation based on the one-way wave equation (Berkhout, 1981), where the term recursive implies that the output wavefield from the last extrapolation step is used as the input wavefield to the next extrapolation step. Wavefield extrapolation techniques enable geophysicists to predict wavefields in the subsurface by propagating the recorded seismic wavefields through an appropriate subsurface velocity model.

Wavefield-continuation imaging methods typically demonstrate a superior capability for imaging complex structures compared to nonrecursive ray-based methods such as diffraction-stack or Kirchhoff migration. A widely agreed explanation (Bevc and Biondi, 2002) is that recursive extrapolators provide a more accurate solution to the wave equation over a wider range of velocities and seismic frequencies. Therefore, they can more easily handle complex wave phenomena such as multiple arrivals and complicated scattering. Figure 1.1 shows an example where the wavefield-continuation migration better images the salt structure and sub-salt features than does the nonrecursive Kirchhoff migration (Soubaras, 2002).

---

<sup>1</sup> They are also called “wave-equation” seismic imaging methods or “wave-equation” migration methods. To avoid confusion with other wave-equation based methods (e.g., nonrecursive Kirchhoff migration), I use “wavefield-continuation” seismic imaging methods or “wavefield-continuation” migration methods in this thesis. This definition was also used by Biondi (2003).

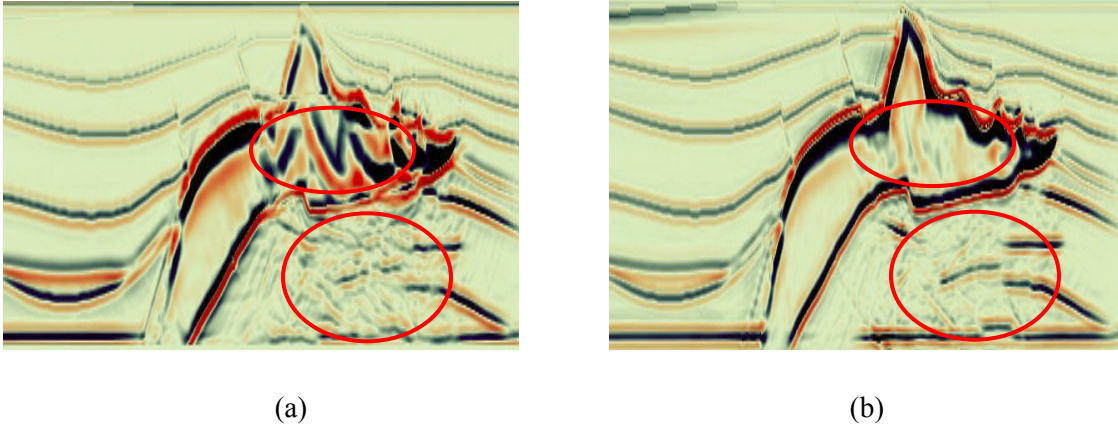


Figure 1.1: Comparison of the images of the 2-D SEG-EAGE salt model from (a) nonrecursive Kirchhoff migration; (b) wavefield-continuation migration based on recursive wavefield extrapolation (Soubaras, 2002).

Many algorithms have been developed that fall into the general category of recursive wavefield extrapolation, such as finite-difference (Claerbout, 1985), space-frequency extrapolation (Berkhout, 1981), phase-shift-plus-interpolation (PSPI) (Gazdag and Sguazero, 1984), split-step Fourier (Stoffa et al., 1990), non-stationary phase shift (NSPS) (Margrave and Ferguson, 1999; Ferguson and Margrave, 2002), and recursive Kirchhoff or Rayleigh<sup>2</sup> extrapolation (Bevc, 1997; Margrave and Daley, 2001; Geiger et al., 2002), to name a few. These recursive extrapolation methods can be categorized into two major groups, implicit and explicit. A typical example of implicit extrapolation is the well-known 45-degree finite-difference method for depth migration (Claerbout, 1985), where the implicit filtering is implemented by solving a linear system of coupled equations for the filtered output points. In contrast, explicit methods approximate the extrapolation operator as finite impulse response filters (Berkhout, 1981). Recursive Rayleigh extrapolation and the family of wavenumber-frequency extrapolations, such as

---

<sup>2</sup> In this thesis, I refer to “recursive Kirchhoff” as “recursive Rayleigh”, and the “Kirchhoff extrapolator” as the “Rayleigh extrapolator”; first, to avoid confusion with the industry standard usage of “Kirchhoff” as a synonym for “diffraction stack”; and second, because the one-way “Kirchhoff extrapolator” is more correctly a discrete formulation of the Rayleigh II integral (Berkhout, 1982, p. 124-127).

PSPI and NSPS methods, are considered to be explicit methods.

## 1.2 Stability and accuracy of space-frequency extrapolators

Explicit wavefield extrapolation methods can be implemented in the space-frequency domain as convolutional filters. Figure 1.2 schematically illustrates the typical implementation of a 2-D  $x$ - $\omega$  (space-frequency) domain extrapolator<sup>3</sup>. At each frequency  $\omega$ , the output wavefield  $\hat{p}(x, z, \omega)$  is obtained by convolving the input wavefield  $\hat{p}(x, z = 0, \omega)$  with an extrapolator that can accommodate local velocity variations. Since the extrapolation is implemented in the space domain, it has attractive advantages compared to  $k_x$ - $\omega$  (wavenumber-frequency) domain extrapolation methods. The most important merit is that it can handle strong lateral velocity variations more simply. Moreover, it can provide protection from spatial wrap-around artifacts that typically appear with  $k_x$ - $\omega$  extrapolation methods.

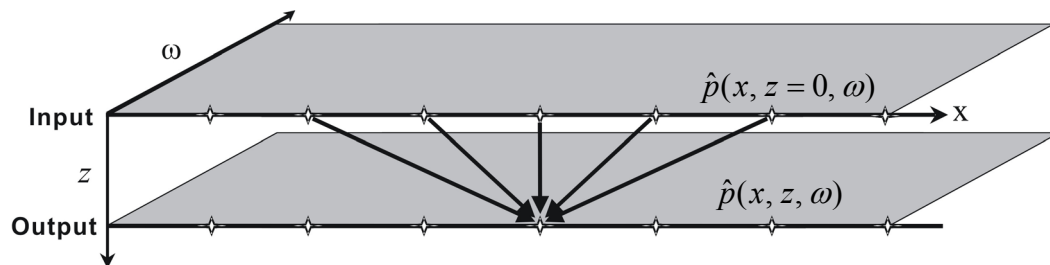


Figure 1.2: Schematic implementation of a 2-D  $x$ - $\omega$  (space-frequency) extrapolation.

Although these are desirable advantages, stability and accuracy are always major concerns when designing  $x$ - $\omega$  extrapolation schemes. Unlike implicit extrapolations,

---

<sup>3</sup> The term “space-frequency extrapolation” refers to all the explicit extrapolation methods that are implemented in the space-frequency domain.

which are unconditionally stable (Godfrey et al., 1979; Claerbout, 1985), explicit extrapolators implemented in the  $x$ - $\omega$  domain are not stable unless special care is taken in their design and implementation. In general, instability results from the spatial truncation of the extrapolation operators, either for the purpose of decreasing the computational cost or due to the inevitable finite aperture of the survey. Specifically, truncation of the spatial aperture of extrapolators causes oscillation in the wavenumber domain, and instability arises when any part of the amplitude spectrum exceeds one (see Maeland, 1994; Thorbecke et al., 2004). Recursive application of the spatially truncated extrapolator tends to amplify the wavefield energy with increasing depth, distorting the final image. Instability is also a result of the Gibbs' phenomena. As shown in Chapter 2, the derivative of the desired extrapolator contains discontinuities in the  $k_x$ - $\omega$  domain. According to the definition of the Gibbs' phenomena, a Fourier transform to the  $x$ - $\omega$  domain does not reconstruct the desired extrapolator at these discontinuities, even if the spatial extent is infinite. Instead, amplitude overshoot occurs around the discontinuities which will also cause instability. In this thesis, I define a stability condition in which no amplitude at any frequency should grow with depth. Thus, the stability condition is not automatically fulfilled with  $x$ - $\omega$  extrapolators.

Another important factor is accuracy, which in general is a measurement of how well the designed extrapolator approximates the desired ideal extrapolator. Accuracy is affected by parameters such as extrapolation aperture and is compromised if the amplitude and phase spectra of the extrapolator deviate from those of the desired operator.

Many efforts have been devoted to stabilize  $x$ - $\omega$  extrapolators without sacrificing accuracy. Holberg (1988) and Blacquière et al. (1989) suggested a constrained non-linear least-square method to design 2-D and 3-D stable extrapolators, respectively. Hale (1991) showed that the recursive application of non-linear least-square optimized extrapolators may still result in instability and/or exponential decay of the seismic wavefield with depth. In addition, the nonlinear algorithm is usually expensive and can be trapped in a local minimum (Thorbecke et al., 2004). As an alternative, Hale (1991) designed a stable explicit extrapolator using a modified Taylor series method. Although the Hale extrapolator is sufficiently stable<sup>4</sup>, Hale's method is based on the Taylor series expansion about wavenumber zero; therefore, it is not accurate for propagating the wavefield at high angles (i.e. at high wavenumbers). An additional drawback is that the Hale extrapolator is designed in the  $k_x$ - $\omega$  domain; thus it does not handle irregular acquisition geometry as well as, for example, the recursive Rayleigh extrapolator. In addition, the artifacts caused by the nature of the extrapolator design make it suboptimal (see Chapter 3).

A more straightforward way to stabilize the  $x$ - $\omega$  extrapolator, as well as to accommodate irregular geometry, is to taper the extrapolator in the space domain with a window function. A successful example was shown by Nautiyal et al. (1993), who used a Gaussian window to taper a Rayleigh extrapolator. However, as discussed in Chapter 3, the phase accuracy and steep-dip imaging capabilities of the Nautiyal extrapolator are inferior to the Hale extrapolator.

---

<sup>4</sup> Etgen (1994) stated that instability is also a function of the degree of lateral velocity variation and the persistence of velocity features with depth. Even the Hale extrapolator becomes unstable with some laterally-varying velocity models. Thus, strictly speaking, the Hale extrapolator is unconditionally stable only with constant velocity model. Since the instability discovered by Etgen is not directly related to the extrapolator design, it will not be discussed further in this thesis.

Other extrapolators have also been designed that demonstrate interesting stability and accuracy features. Soubaras (1996) suggests equiripple polynomial expansion combined with Laplacian synthesis, while Thorbecke and Rietveld (1994) and Thorbecke et al. (2004) suggest an optimized weighted least-squares method.

The  $x$ - $\omega$  extrapolation methods mentioned in the previous paragraph were tested for stability and accuracy by their authors. These analyses vary greatly, depending on the author and the time of the publication. By examining the literature, we can make the following observations on previous stability and accuracy analyses:

1. Many tools have been developed for the stability and accuracy analysis of extrapolation methods. One of the standard tools is the zero-offset constant velocity impulse response test. There are, however, other quantitative tools that are more effective but have seen limited use. To date, there has not been a study that compares the stability and accuracy of various extrapolators using a common set of tools, especially tools that quantitatively evaluate the performance of the extrapolators. A complete set of tools is required in order to undertake a fair comparison between various extrapolation methods, and to develop an understanding of the important factors affecting stability and accuracy. This is especially important for the evaluation of newly developed methods, in particular when the goal is to show whether these new methods have superior capabilities compared to older established methods.
2. The display methods used in the literature are not consistent. The selection of model parameters varies, which makes an unbiased comparison difficult. In

addition, the quality of images varies widely. For example, Hale (1991) shows a figure of an impulse response test which appears to be free from artifacts. However, as shown in Chapter 3, the nature of the design of Hale's method introduces artifacts that are clearly evident in a display with more dynamic range.

3. Many of the published stability and accuracy analyses are limited to simple constant velocity models. These are suitable for illustrating basic characteristics such as the angular aperture of the extrapolator. However, the behaviour of extrapolators in a complex model (e.g. the Marmousi model) is not easy to predict based on these simple constant velocity tests.
4. The stability and accuracy of some extrapolators have not been rigorously investigated. A recursive Rayleigh extrapolator proposed by Margrave and Daley (2001) as a part of the research at POTSI (*Pseudodifferential Operator Theory and Seismic Imaging*) Project has attractive advantages such as the capability to handle irregular acquisition geometry and rough topography (Margrave and Geiger, 2002). However, the stability and accuracy of this extrapolator was not sufficiently addressed in the 2001 paper, nor in subsequent papers (Geiger et al., 2002; Margrave and Geiger, 2002).
5. The newly developed recursive Rayleigh extrapolator has not been compared to a similar method introduced by Nautiyal et al. (1993). Nautiyal et al. (1993) suggest tapering the extrapolator in the space domain with a Gaussian window to stabilize the extrapolator. However, they in turn did not compare their extrapolator with the Hale extrapolator (Hale, 1991), which is widely considered one of the standard

explicit extrapolation methods.

Motivated by these observations, this thesis seeks to examine the stability and accuracy of different extrapolation methods using a common set of tools. It would be ideal to compare all the extrapolators that have been introduced in the literature. However, given the main objective of developing a more sophisticated method for stability and accuracy analysis, I have limited this study to three extrapolators: the recursive Rayleigh extrapolator, the Nautiyal extrapolator and the Hale extrapolator. This choice of extrapolators is based on the following considerations:

1. As a part of the fundamental research under the POTSI Project, the performance of the recursive Rayleigh extrapolator is still under active investigation. It would be valuable to evaluate the stability and accuracy of the Rayleigh extrapolator and compare its performance against other extrapolators.
2. A Nautiyal extrapolator is equivalent to a recursive Rayleigh extrapolator multiplied by the product of a spatial Gaussian window and a boxcar function. The Nautiyal extrapolator is most closely related to the Rayleigh extrapolator, thus it is an obvious candidate for comparative analysis.
3. Hale's 1991 paper made significant contribution to the development of the explicit extrapolator. However, the 2-D Hale extrapolator (1991) has been rarely duplicated for comparison in later publications. Possible explanations are (i) calculation of the extrapolator requires symbolic differentiation that is not generally available; (ii) there is a derivation error in his paper (as pointed out in Chapter 2); and (iii) recent research efforts have focused on 3-D extrapolators

(e.g., Notfors, 1995; Mittet, 2002). Despite these factors, it is still worthwhile to develop the 2-D Hale extrapolator as a “benchmark” for comparison of extrapolators.

4. These three extrapolators have never been compared together and applied to a common complex model. The Marmousi model (Versteeg and Grau, 1991) is a good candidate for comparative analysis, because this model is considered to be a challenge to modern imaging methods.

To make the comparison fair, the three extrapolation methods used in the thesis are implemented in Matlab<sup>®</sup> and applied to simple and complex synthetic datasets.

### **1.3 Adaptive tapering for the first extrapolation step**

In wavefield extrapolation, the surface data are typically padded by adding a number of zero traces (null data) to each side, such that the reflection energy can be extrapolated beyond the original aperture. This procedure introduces two kinds of truncations that need to be addressed. One truncation is the survey truncation caused by the finite acquisition survey, i.e. there will be a discontinuity between the null data and the acquired data. The second truncation results from the spatial limitation of the extrapolator aperture, given that extrapolator truncation is typically desired to decrease computational cost. To properly extrapolate surface data with zero-padding, an adaptive tapering scheme is proposed to handle truncations dynamically. As will be shown in Chapter 4, the adaptive tapering scheme can be combined with stable extrapolators to achieve a more optimal image.

## 1.4 Contribution of the thesis

The contributions of this thesis are as follows:

1. The three extrapolators studied in this thesis are coded and implemented for various tests. The codes developed for this study will be made available to colleagues and used as a basis for further research. In addition, the parallel Matlab<sup>®</sup> implementation used for migration of the Marmousi dataset provides an alternative to a parallel implementation using C and MPI (*Message Passing Interface*). Although the latter is more efficient, the former is easier to implement and takes advantage of Matlab's powerful visualization capability. These features have greatly facilitated debugging and comparative evaluation of Matlab<sup>®</sup> and C-MPI codes.

The Rayleigh extrapolator and the Nautiyal extrapolator are completely coded in Matlab<sup>®</sup>. The coefficients of the Hale extrapolator are computed using Maple<sup>®</sup> because it requires symbolic differentiation, and the extrapolator is then used in the Matlab<sup>®</sup> codes for prestack and poststack tests.

2. I develop an intuitive way to visualize various wavefield extrapolators.
3. I conduct a comprehensive stability and accuracy analysis of the three extrapolators using a common set of tools, including 3-D error plots, error contours, zero-offset impulse response, prestack dip accuracy and complex imaging using the Marmousi dataset. This leads to a better understanding of the stability and accuracy problems, and a more effective evaluation of various extrapolators.

4. I document the derivation error in Hale's paper and the artifacts from the Hale extrapolator that were not described in his paper.
5. In chapter 3 of this thesis, I show that the Rayleigh extrapolator is not sufficiently stable for the large number of extrapolation steps that are typically required to image modern datasets. However, its application can be limited to the first few extrapolation steps to regularize the data. Other more stable extrapolation methods that require regularized data can be used for the remaining steps.
6. A new adaptive tapering method is presented that dynamically tapers the edges of the extrapolator and survey. This method is designed to handle the truncation problems for the first extrapolation step where data are padded with zero traces.

## 1.5 Structure of the thesis

In Chapter 2, I provide a brief theoretical review of wavefield extrapolation, starting with the scalar wave equation. I then derive various wavefield extrapolators in the  $k_x$ - $\omega$  and  $x$ - $\omega$  domains.

In Chapter 3, I develop a comprehensive methodology for stability and accuracy analysis of the selected recursive extrapolators. The Rayleigh extrapolator, the Nautiyal extrapolator and the Hale extrapolator are evaluated using a common set of tools and then applied to the common-source prestack depth migration of the Marmousi dataset.

In Chapter 4, I introduce a new adaptive tapering scheme, which is then used to create more optimal images of the Marmousi dataset. The final conclusions are made in Chapter 5.

## Chapter Two: REVIEW OF WAVEFIELD EXTRAPOLATORS

The essential component of most modern wavefield-continuation migration methods is wavefield extrapolation based on the one-way wave equation. In this chapter, I introduce the one-way wave equation and provide basic derivations of the three extrapolators selected for stability and accuracy analysis. A derivation error in Hale's paper (1991) is identified and corrected by equation (2.30) in Section 2.3.

The imaging condition and the implementation of the common-source migration, one of the typical wavefield-continuation migration methods, are briefly described at the end of this chapter.

### 2.1 One-way wave propagation

In a homogenous medium, the 2-D acoustic scalar wave equation can be expressed as

$$\nabla^2 p = \frac{1}{v^2} \frac{\partial^2 p}{\partial t^2}, \quad (2.1)$$

where  $p=p(x, z, t)$  is the pressure wavefield and  $v$  denotes the velocity. The  $z$ -axis increases downward, and  $\nabla^2 p = \frac{\partial^2 p}{\partial x^2} + \frac{\partial^2 p}{\partial z^2}$  is the Laplacian with respect to  $x$  and  $z$ .

Assuming a constant velocity, after a 2-D Fourier transform of equation (2.1) with respect to  $x$  and  $t$ , we obtain the 2-D Helmholtz equation

$$\frac{\partial^2 \hat{p}(k_x, z, \omega)}{\partial z^2} = -\left(\frac{\omega^2}{v^2} - k_x^2\right) \hat{p}(k_x, z, \omega), \quad (2.2)$$

where  $\omega$  is the angular frequency,  $k_x$  is the horizontal wavenumber, and  $\hat{p}$  indicates any Fourier transform of the pressure wavefield  $p$ . The Fourier transform variables are specified explicitly. The signs in equation (2.2) depend on the sign convention of the 2-D Fourier transform. I use a 2-D Fourier transform with the following convention:

$$\hat{p}(k_x, z, \omega) = \int_{-\infty-\infty}^{+\infty+\infty} p(x, z, t) e^{i(\omega t - k_x x)} dx dt . \quad (2.3)$$

The analytical solution to the above ordinary differential equation (2.2) is

$$\hat{p}(k_x, z, \omega) = A e^{ik_z z} + B e^{-ik_z z} , \quad (2.4)$$

where  $A$  and  $B$  are the coefficients independent of depth  $z$ , and the vertical component of the wavenumber vector,  $k_z$ , can be expressed as

$$k_z = \sqrt{\frac{\omega^2}{v^2} - k_x^2} . \quad (2.5)$$

Equation (2.5) is known as the dispersion relation of the 2-D scalar wave equation.

The two coefficients  $A$  and  $B$  in equation (2.4) are determined by enforcing two boundary conditions. One boundary condition requires the normal derivative of wavefield be evaluated at  $z=0$ . Since the derivative is generally not available, we assume that the recorded wavefield is strictly an upcoming wave, i.e., reflections, multiple reflections, head waves and mode conversions are not generated (Holberg, 1988). According to our Fourier transform convention (equation (2.3)), the inverse Fourier kernel will be  $e^{-i\omega t}$ . Thus an upward traveling wave  $\hat{p}_u(k_x, z, \omega)$  ( $z$  decreases while  $t$  increases) will have the form  $e^{-i(\omega t + k_z z)}$  in order to keep the phase “ $-(\omega t + k_z z)$ ” constant (Claerbout, 1985), which

results in  $A=0$ . The second boundary condition is that the solution must match the data at  $z=0$ , i.e.,  $B = \hat{p}_u(k_x, z=0, \omega)$ . Therefore, equation (2.4) becomes

$$\hat{p}_u(k_x, z, \omega) = \hat{p}_u(k_x, z=0, \omega)e^{-ik_z z}, \quad (2.6)$$

corresponding to downward extrapolation of upgoing waves. Similarly, the downward extrapolation of downgoing waves  $\hat{p}_d(k_x, z=0, \omega)$  (modeling) can be expressed as

$$\hat{p}_d(k_x, z, \omega) = \hat{p}_d(k_x, z=0, \omega)e^{ik_z z}. \quad (2.7)$$

An alternative way to derive equations (2.6) and (2.7) is to factorize the equation (2.2), and to solve the one-way wave equations

$$\frac{\partial \hat{p}(k_x, z, \omega)}{\partial z} = \pm ik_z \hat{p}(k_x, z, \omega). \quad (2.8)$$

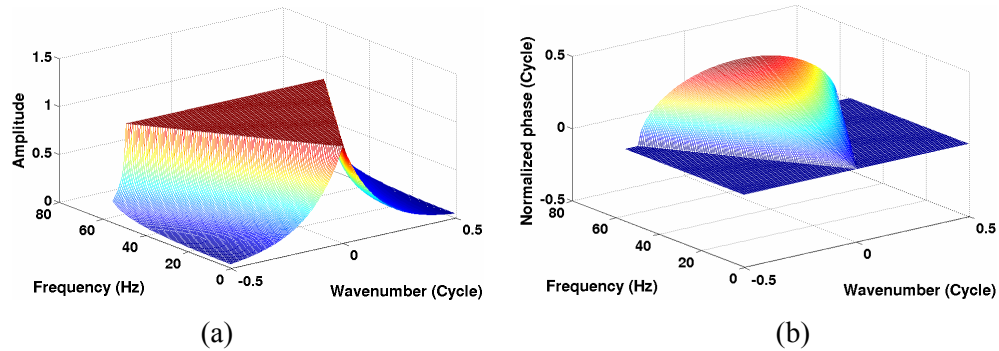


Figure 2.1: (a) Amplitude and (b) phase spectra of the desired extrapolator in the  $k_x$ - $\omega$  domain. Wavenumber and phase are normalized by the factors of  $2\pi/\Delta x$  and  $2\pi$ , respectively.

Equation (2.6) and (2.7) summarize the familiar phase shift method (Gazdag, 1978), where the vertical variation of velocity is accommodated by recursively extrapolating the recorded wavefield through small intervals of constant velocity. The desired band-limited phase-shift operator (extrapolator),  $e^{ik_z z}$ , can be illustrated in the  $k_x$ - $\omega$  domain as in Figure 2.1. A constant velocity of 1250m/s (half-velocity of 2500m/s for

zero-offset extrapolation), a frequency range of 0 to 55Hz, spatial sampling of  $\Delta x = \Delta z = 10\text{m}$  and temporal sampling of 4ms are used for the extrapolator calculation.

## 2.2 Rayleigh extrapolator

The derivation of the Rayleigh extrapolator was described by Margrave and Daley (2001). In order to obtain the wavefield extrapolator in the  $x$ - $\omega$  domain, we inverse Fourier transform equation (2.6) with respect to  $k_x$ ,

$$\hat{p}(x, z, \omega) = \frac{1}{2\pi} \int_{-\infty}^{+\infty} \hat{p}(k_x, z = 0, \omega) e^{ik_x x - ik_z z} dk_x, \quad (2.9)$$

where  $\hat{p}(x, z, \omega)$  is a monochromatic scalar wavefield at position  $(x, z)$ , and  $\hat{p}(k_x, z = 0, \omega)$  is

$$\hat{p}(k_x, z = 0, \omega) = \int_{-\infty}^{+\infty} \hat{p}(x, z = 0, \omega) e^{-ik_x x} dx. \quad (2.10)$$

Inserting equation (2.10) into equation (2.9) and interchanging the order of integration gives

$$\hat{p}(x, z, \omega) = \frac{1}{2\pi} \int_{-\infty}^{+\infty} \hat{p}(\hat{x}, z = 0, \omega) \left[ \int_{-\infty}^{+\infty} e^{ik_x(x-\hat{x}) - ik_z z} dk_x \right] d\hat{x}, \quad (2.11)$$

where  $\hat{x}$  denotes the input coordinate and  $x$  the output coordinate. By defining the 2-D  $x$ - $\omega$  domain extrapolator as

$$W_{2D}(x, z, \nu, \omega) = \frac{1}{2\pi} \int_{-\infty}^{+\infty} e^{ik_x x - ik_z z} dk_x, \quad (2.12)$$

equation (2.11) can be written as

$$\hat{p}(x, z, \omega) = \int_{-\infty}^{+\infty} \hat{p}(\hat{x}, z = 0, \omega) W_{2D}(x - \hat{x}, z, v, \omega) d\hat{x}. \quad (2.13)$$

$W_{2D}$  is called the 2-D  $x$ - $\omega$  domain wavefield extrapolator, and is applied by a 1-D spatial convolution. The analytical form of the 2-D wavefield extrapolator (equation (2.12)) is well known (Robinson and Silvia, 1981). Assuming constant velocity, it can be expressed via the  $z$  derivatives of the 2-D Green's function

$$W_{2D}(x, z, v, \omega) = -2 \frac{\partial}{\partial z} g_{2D}(x, z, v, \omega), \quad (2.14)$$

where the 2-D Green's function is (Zauderer, 1989)

$$g_{2D}(x, z, v, \omega) = \frac{i}{4} H_0^{(1)}(k\rho), \quad (2.15)$$

with  $\rho = \sqrt{x^2 + z^2}$  and  $k = \omega/v$ .  $H_0^{(1)}(u)$  is the zero-order Hankel function of the first kind.

For numerical calculation, the derivative of  $H_0^{(1)}(u)$  is obtained as,

$$\frac{\partial}{\partial u} [H_0^{(1)}(u)] = -H_1^{(1)}(u) = -[J_1(u) + iY_1(u)], \quad (2.16)$$

where  $J_1(u)$  and  $Y_1(u)$  are the first-order Bessel function of the first kind and second kind, respectively. Standard routines for calculating  $J_1(u)$  and  $Y_1(u)$  can be found in the published literature (e.g., Press et al., 1992). Plugging equation (2.15) and (2.16) into equation (2.14), the 2-D extrapolator for constant velocity becomes

$$W_{2D}(x, z, v, \omega) = \frac{i\omega \cos\theta}{2v} H_1^{(1)}\left(\frac{\omega\rho}{v}\right), \quad (2.17)$$

where  $\cos \theta = \frac{z}{\rho}$  is the cosine of the scattering angle.

A final form for equation (2.13) can be developed by substituting equation (2.17) into equation (2.13), yielding

$$\hat{p}(x, z, \omega) = \frac{i\omega}{2} \int_{-\infty}^{\infty} \hat{p}(\hat{x}, z=0, \omega) \frac{\cos \theta}{v} H_1^{(1)}\left(\frac{\omega \tilde{\rho}}{v}\right) d\hat{x}, \quad (2.18)$$

where  $\tilde{\rho} = \sqrt{(x - \hat{x})^2 + z^2}$ . Equation (2.18) represents a spatial convolution of the wavefield with an operator and is interpretable as a wavefield extrapolation operation in the  $x$ - $\omega$  domain that is based on the Rayleigh II integral (Berkhout, 1982). In the context of this thesis, I will call equation (2.18) the *Rayleigh wavefield extrapolation*, and  $W_{2D}$  the *Rayleigh wavefield extrapolator* to avoid confusion with the conventional nonrecursive  $x$ - $t$  domain Kirchhoff migration.

The Rayleigh extrapolator is different from typical  $x$ - $\omega$  extrapolators (e.g., Berkhout, 1981). The traditional  $x$ - $\omega$  extrapolators are usually designed as finite-difference operators and thus assume a uniformly gridded dataset. The Rayleigh extrapolator, on the other hand, is derived from an analytical formula that can be evaluated at any arbitrary spatial location. Therefore, it can easily adapt to irregular geometry and can prove effective for data regularization and in areas of rough topography (Margrave and Geiger, 2002).

Strictly speaking, equation (2.18) holds only for a perfectly homogenous medium. However, notice that the integral for  $W_{2D}$  (equation (2.12)) is over wavenumbers, not spatial coordinates. A simple replacement of constant velocity by lateral variable velocity

in equation (2.18) leads to extrapolators that can approximately accommodate lateral velocity variations. For example, the 2-D Kirchhoff GPSPI (*Generalized Phase Shift Plus Interpolation*) extrapolators are given by,

$$\hat{p}^{GPSPI}(x, z, \omega) = \frac{i\omega}{2v(x)} \int_{-\infty}^{\infty} \hat{p}(\hat{x}, z=0, \omega) \frac{z}{\tilde{\rho}} H_1^{(1)}\left(\frac{\omega\tilde{\rho}}{v(x)}\right) d\hat{x}. \quad (2.19)$$

where the velocity  $v(x)$  is assigned to the output point. Note that the velocity  $v(x)$  is assumed to be a function of the transverse coordinate  $x$ . The velocity variation with depth  $z$  is then accommodated by extrapolating the wavefield in small steps within which the vertical variation of velocity is small enough to be negligible. The desired velocity values for the extrapolator are the ones that can provide the best approximation of the true phase (propagation time) of the seismic wavefield between the input points and the output point.

In addition to the above GPSPI-type extrapolator, other Rayleigh extrapolators have been designed to handle lateral velocity variations: a GNSPS-type (*Generalized Non-Stationary Phase Shift*) extrapolator uses the velocities at the input points; a GSNPS-type (*Generalized Symmetric Non-Stationary Phase Shift*) extrapolator incorporates two extrapolation steps of  $dz/2$  where the first step uses the velocities at the input points (GNSPS-type) and the second step uses the velocity at the output point (GPSPI-type); a GWeyl-type (*Generalized Weyl*- based upon a quantum mechanical idea in Weyl (1931)) extrapolator uses an average of the velocities between each input point and the output point (see, Margrave and Daley, 2001; Geiger et al., 2002).; while the PAVG-type extrapolator (Geiger et al., 2003) uses the velocity calculated as an average slowness along straight raypath between each input point and the output point. In this thesis, I use

the GPSPI-type Rayleigh extrapolator for tests with a heterogeneous medium.

Ideally, the Rayleigh extrapolator should extend to infinity in the lateral coordinates. From equation (2.5) and (2.12), it is evident that the amplitude of the Rayleigh extrapolator in the wavenumber domain is less than one in the evanescent region where  $|k_x| > \omega/v$  or equal to one in the propagating wave region where  $|k_x| < \omega/v$ . However, the extrapolator is usually truncated to a finite length to reduce computational cost (e.g., truncated to 19 points) as shown in Figure 2.2 and a constant frequency extraction from Figure 2.2 as shown in Figure 2.3. This truncation is equivalent to multiplying the extrapolator by a box-car function in the space domain which, in turn, is equivalent to convolving a *sinc* function (the Fourier transform of the box-car function) with the extrapolator in the wavenumber domain. As a result, ripples can be observed in the wavenumber domain where part of the amplitudes of the extrapolator will oscillate about the desired value of one (see Figure 2.2a and Figure 2.3a). The wavefield tends to grow or decay exponentially with the recursive application of the truncated extrapolator. In other words, the recursive Rayleigh extrapolator is unstable by design.

The instability is also a result of the Gibbs' phenomenon. The definition of the Gibbs' phenomenon tells us that "when a waveform that includes a discontinuity (or whose derivative is discontinuous) is Fourier synthesized, the fit is poor near the discontinuity. As the number of frequency components included in the synthesis increases, the region of poor fit becomes narrower, but some overshoot at discontinuities continues" (Sheriff, 2002). In our case, we are seeking an extrapolator in the  $x$ - $\omega$  domain that can best Fourier synthesize the desired extrapolator in the  $k_x$ - $\omega$  domain. Notice that

the derivative of the desired extrapolator contains discontinuities at the evanescent boundaries ( $|k_x|=\omega/v$ ) (see Figure 2.1). According to the definition of the Gibbs' phenomenon, even the Rayleigh extrapolator with an infinite length cannot exactly Fourier synthesize the desired extrapolator. Increasing the length of the Rayleigh extrapolator will narrow the misfit, but the overshoot at evanescent boundaries is still present (see Figure 2.4). The overshoot will cause instability when the extrapolator is applied recursively.

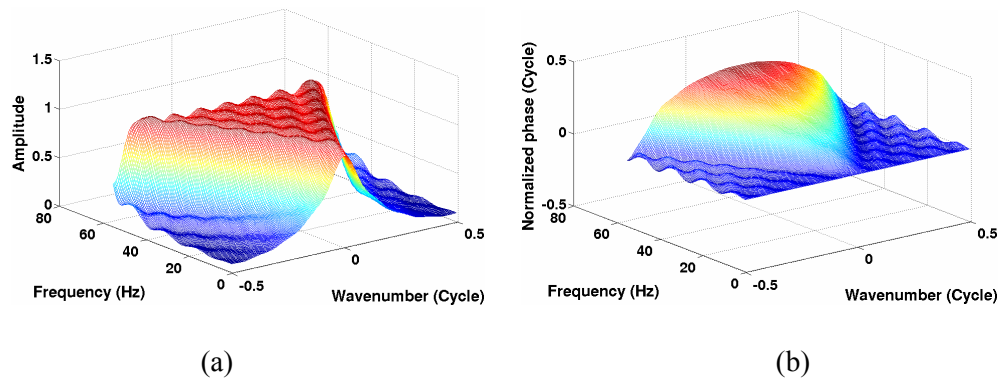


Figure 2.2: (a) Amplitude and (b) phase spectra of a 19-point Rayleigh extrapolator in the  $k_x$ - $\omega$  domain. The parameters are the same as those in Figure 2.1.

Tapering is a standard tool for reducing the ripples associated with the spatial truncation and Gibbs' phenomena (see, Sheriff, 2002, p. 347-348). One of the straightforward tapering schemes is to apply Hanning edge tapers to the Rayleigh extrapolator in the space domain. The half Hanning window used as the edge taper is defined as

$$W_H(n) = 0.5 \mp 0.5 \cos\left(\pi \frac{n}{L+1}\right), \quad (2.20)$$

where  $n=1, \dots, L$ . The plus and minus sign is used for the right and left edge taper, respectively. The taper length  $L$  is empirically chosen to be 5 points for the 19-point

extrapolator.

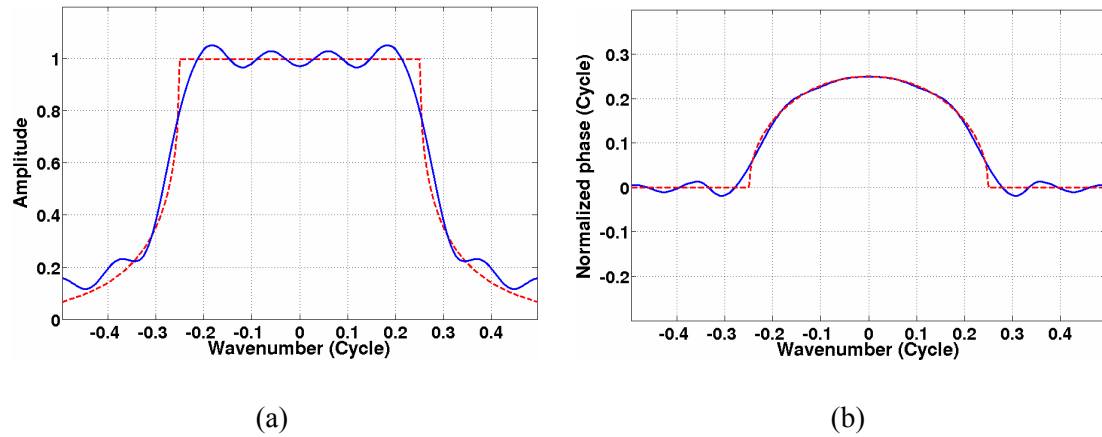


Figure 2.3: (a) Amplitude and (b) phase spectra of a 19-point Rayleigh extrapolator at the frequency of 31.25 Hz (blue lines). The evanescent boundaries are at  $k_x = \pm 0.25$ . The dashed red lines are the amplitude and phase spectra of the desired extrapolator.

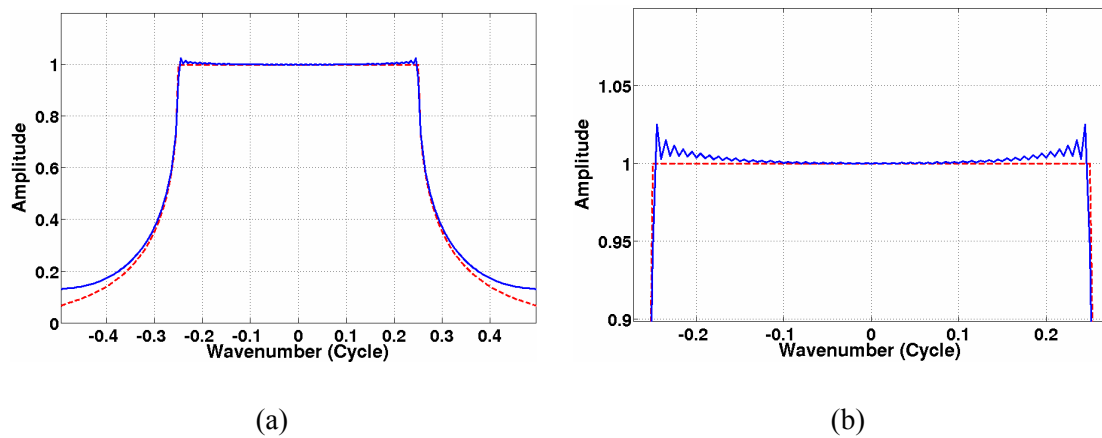


Figure 2.4: Amplitude spectrum of a 200-point Rayleigh extrapolator at the frequency of 31.25 Hz (blue lines). The close-up of (a) is shown in (b). The evanescent boundaries are at  $k_x = \pm 0.25$ . The dashed red lines are the desired amplitude spectrum.

The amplitude and phase spectra of the 19-point Hanning-tapered Rayleigh extrapolator are shown in Figure 2.5 and Figure 2.6. As expected, the ripples in Figure 2.2 and Figure 2.3 are attenuated by the Hanning tapers. However, it is still unstable because some of the amplitudes are bigger than one (Figure 2.6a). A more complete stability analysis of the Rayleigh extrapolator will be shown in Chapter 3.

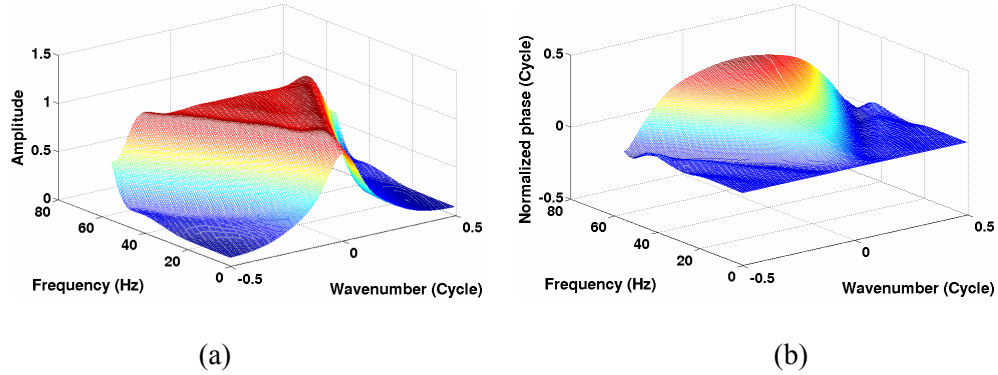


Figure 2.5: (a) Amplitude and (b) phase spectra of a 19-point Hanning-tapered Rayleigh extrapolator in the  $k_x$ - $\omega$  domain. The parameters are the same as those in Figure 2.1.

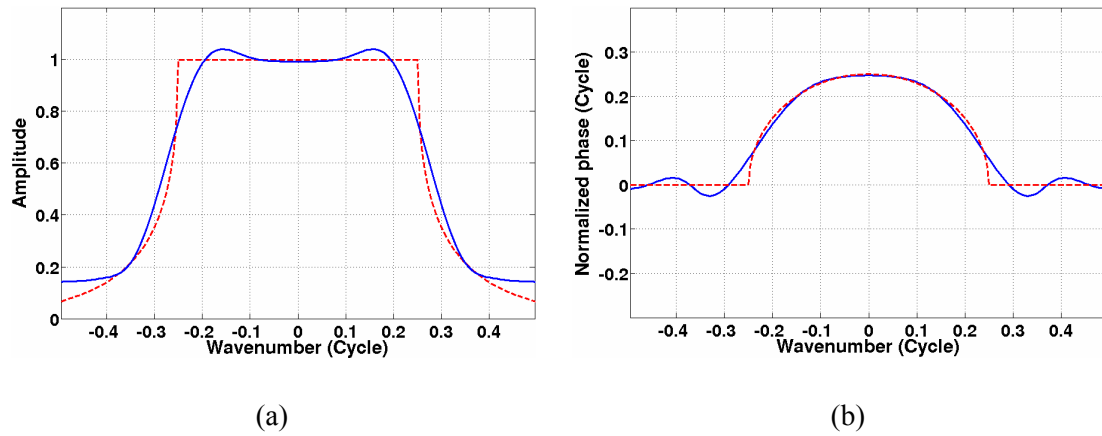


Figure 2.6: (a) Amplitude and (b) phase spectra of a 19-point Hanning-tapered Rayleigh extrapolator at the frequency of 31.25 Hz (blue lines). The evanescent boundaries are at  $k_x = \pm 0.25$ . The dashed red lines are the amplitude and phase spectra of the desired extrapolator.

Alternatively, Hale (1991) and Nautiyal (1993) propose methods to design stable extrapolators. The Hale extrapolator is designed in the wavenumber domain by matching the first few terms of the Taylor series expansion of the desired extrapolator; whereas Nautiyal suggests multiplying the Rayleigh extrapolator by a truncated Gaussian window in the space domain.

### 2.3 Hale extrapolator

Hale (1991) proposed a modified Taylor series method to design explicit

wavefield extrapolators. The method can be viewed as the design of a finite length extrapolation filter  $h(n)$  with a Fourier transform  $H(\hat{k})$  that best approximates the Fourier transform  $D(\hat{k})$  of the desired extrapolator,

$$D(\hat{k}) = e^{ik_z \Delta z} = \exp \left\{ i \left( \frac{\Delta z}{\Delta x} \right) \left[ \left( \frac{\omega \Delta x}{v} \right)^2 - \hat{k}^2 \right]^{1/2} \right\}, \quad (2.21)$$

where  $\omega$  denotes the angular frequency (in radians per unit time),  $v$  denotes velocity,  $\Delta z$  and  $\Delta x$  denote vertical and horizontal spatial sampling intervals. The normalized wavenumber  $\hat{k}$  (in radians per sample) is obtained by multiplying the wavenumber  $k_x$  by  $\Delta x$ .  $D(\hat{k})$  is the familiar filter applied in Gazdag's (1978) phase-shift migration, as illustrated in Figure 2.1. The dependency of  $D(\hat{k})$  on frequency, velocity and depth is suppressed for convenience in this discussion.  $H(\hat{k})$  is subject to the constraint that  $|H(\hat{k})| \leq 1$  for  $|\hat{k}| \leq \pi$ .

The desired transform  $D(\hat{k})$  uniquely depends on the two dimensionless constants  $\Delta z / \Delta x$  and  $\omega \Delta x / v$ . Equation (2.21) indicates that  $D(\hat{k})$  is symmetric with respect to  $\hat{k}$  (both the real and imaginary parts are even), which implies that  $h(n)$  should also be even. Thus, the length of  $h(n)$ , measured by  $N$ , should be odd, with the coefficient index  $n$  bounded by  $-(N-1)/2 \leq n \leq (N-1)/2$ . Moreover, due to the symmetry of  $h(n)$ , it is completely described by  $(N+1)/2$  coefficients.

The extrapolation filter  $h(n)$  is defined by

$$h(n) = \sum_{m=0}^{M-1} c_m b_{mn}, \quad (2.22)$$

where the  $c_m$  is to be determined, the basis function  $b_{mn}$  is chosen as

$$b_{mn} = (2 - \delta_{m0}) \cos\left(\frac{2\pi mn}{N}\right), \quad (2.23)$$

and  $\delta_{m0}$  is the *Kronecker delta function* defined by

$$\delta_{m0} = \begin{cases} 1. & \text{if } m = 0; \\ 0. & \text{otherwise.} \end{cases} \quad (2.24)$$

To ensure the stability of extrapolator (i.e.,  $|H(\hat{k})| \leq 1$ ), the number of weights,  $M$ , in equation (2.22) should be less than the number of filter coefficients  $(N+1)/2$ . The Fourier transform of  $h(n)$  is obtained as

$$H(\hat{k}) = \sum_{m=0}^{M-1} c_m B_m(\hat{k}), \quad (2.25)$$

where

$$B_m(\hat{k}) = (2 - \delta_{m0}) \sum_{n=0}^{(N-1)/2} (2 - \delta_{n0}) \cos\left(\frac{2\pi mn}{N}\right) \cos(\hat{k}n). \quad (2.26)$$

The Taylor series expansion of the desired transform  $D(k)$  and the approximation  $H(\hat{k})$  about 0 (i.e., the MacLaurin series) can be calculated respectively as

$$D(\hat{k}) = D(0) + D'(0)\hat{k} + \frac{D''(0)}{2!}\hat{k}^2 + \dots + \frac{D^{(n)}(0)}{n!}\hat{k}^n + \dots \quad (2.27)$$

and

$$\begin{aligned}
H(\hat{k}) &= H(0) + H'(0)\hat{k} + \frac{H''(0)}{2!}\hat{k}^2 + \dots + \frac{H^{(n)}(0)}{n!}\hat{k}^n + \dots \\
&= \sum_{m=0}^{M-1} c_m B_m(0) + \hat{k} \sum_{m=0}^{M-1} c_m B'_m(0) + \frac{\hat{k}^2}{2!} \sum_{m=0}^{M-1} c_m B''_m(0) + \dots + \frac{\hat{k}^n}{n!} \sum_{m=0}^{M-1} c_m B_m^{(n)}(0) + \dots
\end{aligned} \tag{2.28}$$

Since  $D(\hat{k})$  and  $H(\hat{k})$  are symmetric, the odd derivatives at  $\hat{k} = 0$  in equation (2.27) and (2.28) are all zero.

The conventional way to approximate  $D(\hat{k})$  is to match the first  $(N+1)/2$  even derivatives at  $\hat{k} = 0$  in equation (2.27), which could result in an unstable extrapolation filter. The instability rises when the amplitudes of  $H(\hat{k})$  exceed one due to the truncation of the infinite Taylor series. Instead, Hale suggests matching only the first  $M$  (for  $M \leq (N+1)/2$ ) even derivatives, yielding the following linear system,

$$\sum_{m=0}^{M-1} c_m B_m^{(2l)}(0) = D^{(2l)}(0), \tag{2.29}$$

where,

$$B_m^{(2l)}(0) = \begin{cases} (2 - \delta_{m0}) \left[ 1 + 2 \sum_{n=1}^{(N-1)/2} \cos\left(\frac{2\pi mn}{N}\right) \right] & (l = 0) \\ 2(2 - \delta_{m0})(-1)^l \sum_{n=1}^{(N-1)/2} \cos\left(\frac{2\pi mn}{N}\right) n^{2l} & (l = 1, 2, \dots, M-1) \end{cases}. \tag{2.30}$$

Note that Equation (2.30) corrects Hale's equation (A-6):

$$B_m^{(2l)}(0) = (2 - \delta_{m0})(-1)^l \sum_{n=0}^{(N-1)/2} (2 - \delta_{n0}) \cos\left(\frac{2\pi mn}{N}\right) n^{2l}. \tag{2.31}$$

Hale's equation neglects the fact that the derivative of a constant is zero. However, Hale coded the right formula since I am able to duplicate the figures in his paper using

equation (2.30).

The remaining  $[(N+1)/2]-M$  degrees of freedom are used to achieve the stability of the extrapolation filter. The weights  $c_m$  can be obtained from equation (2.29) by solving the linear system. The extrapolation filter  $h(n)$  is then obtained from equation (2.22).

Since the symbolic differentiation in equation (2.29) is not generally available in Matlab<sup>®5</sup>, I use Maple<sup>®</sup> to compute the coefficients of Hale extrapolators which are then used in the Matlab<sup>®</sup> for poststack and prestack experiments. For tests with a heterogeneous media, a table of GPSPI-type Hale extrapolators is computed where the velocity in Equation (2.21) is assigned to the output point.

A 19-point ( $N=19$ ,  $M \leq 10$ ) Hale extrapolator in the  $k_x$ - $\omega$  domain is illustrated in Figure 2.7. Figure 2.8 shows its spectra at a constant frequency. The blocky appearance of the phase figures (Figure 2.7b and Figure 2.8b) is a result of phase wrapping at  $\pm\pi$  (normalized to  $\pm 0.5$ ) boundaries, which is caused by the notched design of the Hale extrapolator. Since the phase wrap-around happens outside the evanescent boundary ( $k_x = \pm 0.25$  in Figure 2.8b), it will have little impact on the propagating waves. Figure 2.9 shows only the phase spectrum of the Hale extrapolator in the propagating wave region. All the values outside the evanescent boundaries are zeroed for a better illustration. However, the zeroing is only for the display purpose. There is no zeroing in the implementation of the Hale extrapolator.

---

<sup>5</sup> The professional version of Matlab includes a symbolic toolbox that is built on Maple's symbolic engine. Unfortunately, this toolbox was not included in the Matlab version licensed to the University of Calgary when I conducted my thesis research.

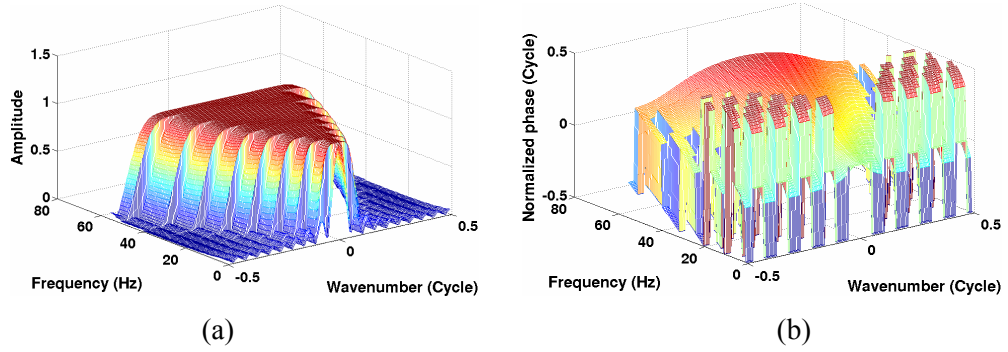


Figure 2.7: (a) Amplitude and (b) phase spectra of a 19-point Hale extrapolator in the  $k_x$ - $\omega$  domain. The parameters are the same as those in Figure 2.1.

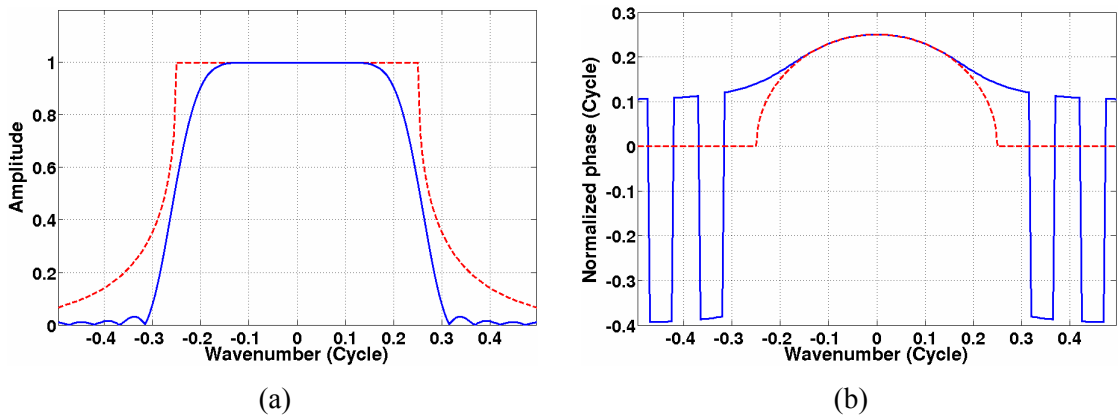


Figure 2.8: (a) Amplitude and (b) phase spectra of a 19-point Hale extrapolator at the frequency of 31.25 Hz (blue lines). The evanescent boundaries are at  $k_x = \pm 0.25$ . The dashed red lines are the amplitude and phase spectra of the desired extrapolator.

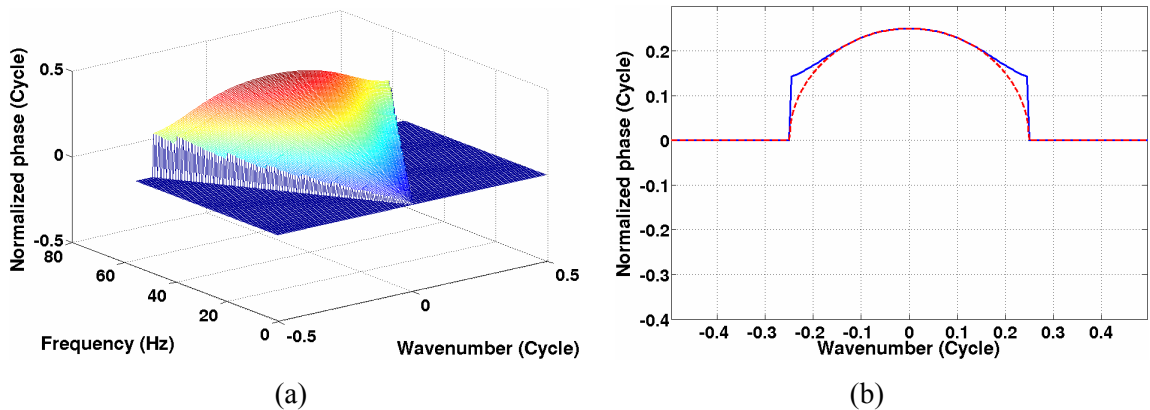


Figure 2.9: Phase spectra of a 19-point Hale extrapolator (a) in the  $k_x$ - $\omega$  domain and (b) at the frequency of 31.25Hz. All the values outside the evanescent boundaries are zeroed.

For given velocity, frequency, and spatial sampling intervals ( $\Delta x$  and  $\Delta z$ ), the

desired  $M$  value is found by testing different  $M$  values until  $|H(\hat{k})| > 1$ . In practice, I consider an extrapolator to be stable when its amplitude is smaller than 1.0001 for all wavenumbers. After 1000 extrapolation steps in a homogenous medium, the amplitude at a single frequency will be amplified to a maximum value of  $1.0001^{1000} = 1.1052$ . This is considered as being “reasonably” stable. The desired error tolerance can be adjusted depending on the number of the extrapolation steps required and the criteria chosen for stability.

Testing different  $M$  values for each frequency can be time-consuming. A shortcut utilized here is to look at the amplitude spectrum of desired extrapolator in the  $k_x$ - $\omega$  domain (Figure 2.1). In Figure 2.1, it can be noticed that the width of propagating wave region (where amplitude equals one) increases with frequency. This can be explained by the fact that the evanescent boundary  $\omega/v$  increases. Therefore, the desired  $M$  value should also increase with frequency. For the whole frequency band, testing for the optimal  $M$  value at later frequency can start with the  $M$  value selected at the previous frequency. The  $M$  value is increased until the extrapolator becomes unstable. In other words, testing for the optimal  $M$  value does not have to start with one (or from  $(N+1)/2$ ) for each frequency. In addition, due to the symmetry of the Hale extrapolator, only the coefficients at positive wavenumbers are calculated to save computation time and storage.

## 2.4 Nautiyal extrapolator

Nautiyal et al. (1993) suggested applying a Gaussian window,

$$T(x) = e^{-\frac{x^2}{2\sigma^2}}, \quad (2.32)$$

to taper the Rayleigh extrapolator<sup>6</sup> in the  $x$ - $\omega$  domain, where  $\sigma$  is a parameter to be chosen to optimize the stability and accuracy.

In this thesis, I use the “*gausswin*” function included in the Matlab<sup>®</sup> Signal Processing Toolbox<sup>®</sup>, where the Gaussian window is defined as

$$W_G(n+1) = e^{-\frac{1}{2} \left( \gamma \frac{n-L/2}{L/2} \right)^2}, \quad (2.33)$$

where  $0 \leq n \leq L$  and  $\gamma \geq 2$ . The parameter  $L$  controls the length of the Gaussian window; while  $\gamma$  is the reciprocal of the standard deviation and controls the shape of the window. Figure 2.10 shows a 19-point Nautiyal extrapolator in the  $k_x$ - $\omega$  domain. Figure 2.11 is sliced from Figure 2.10 at a constant frequency. Unlike the Hale extrapolator, the Nautiyal extrapolator has a phase error at  $k_x=0$  (Figure 2.11b).

Equations (2.32) and (2.33) indicate that the ideal Gaussian window extends to infinity. In practice, the length of the Gaussian window is equal to the length of the extrapolator and therefore must be truncated. Truncation of the Gaussian window also introduces an oscillation to the wavenumber domain and may cause instability. Nevertheless, as shown in Chapter 3, the Nautiyal extrapolator has reasonable stability, i.e. the Gaussian window is effective in attenuating amplitude fluctuations in the wavenumber domain.

---

<sup>6</sup> Nautiyal used the name “spatial wavelet” in his paper which is in fact the Rayleigh extrapolator.

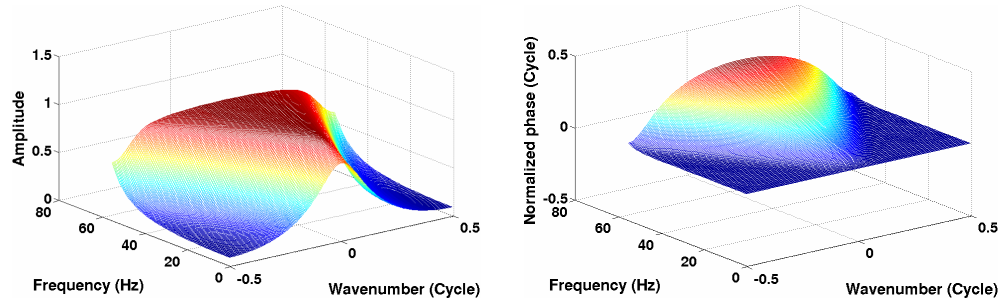


Figure 2.10: (a) Amplitude and (b) phase spectrum of a 19-point Nautiyal extrapolator in the  $k_x$ - $\omega$  domain. The parameters are the same as those in Figure 2.1.

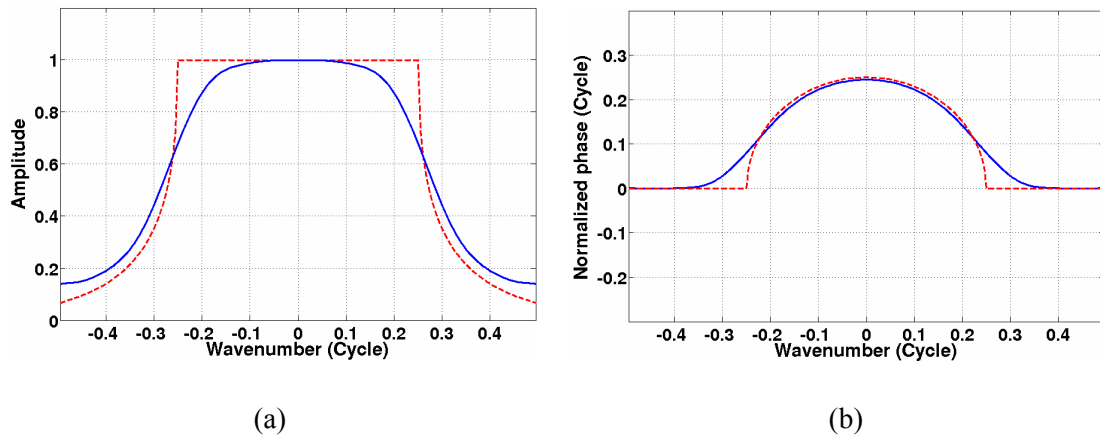


Figure 2.11: (a) Amplitude and (b) phase spectra of a 19-point Hale extrapolator at the frequency of 31.25 Hz (blue lines). The evanescent boundaries are at  $k_x = \pm 0.25$ . The dashed red lines are the amplitude and phase spectra of the desired extrapolator.

## 2.5 Common-source migration and imaging condition

Most of the wavefield-continuation migration methods fall into two major categories: (1) common-source migration<sup>7</sup> and (2) source-receiver migration. A common-source migration is applied to each common-source gather (a collection of the traces that have the same source location) and consists of forward extrapolation of a modeled source and backward extrapolation of the receiver wavefield (i.e., the acquired data). A source-

---

<sup>7</sup> Other standard terms are “shot-profile migration” and “common-shot migration”. To avoid confusion between “shot” and “source”, I use “common-source migration” in this thesis.

receiver migration is based on the concept of survey sinking by which we recursively synthesize datasets at increasing depth. Both of the migration methods require a proper imaging condition at each depth step.

The implementation of a common-source migration is illustrated in Figure 2.12. A reflector at a particular depth step is imaged by (1) forward extrapolating a modeled source wavefield (Figure 2.12a); (2) backward extrapolating the receiver wavefield (Figure 2.12b) and (3) applying an imaging condition (Figure 2.12c). With recursive wavefield extrapolators, the output source and receiver wavefields from one step are used as the input wavefields for the next step. For each common-source gather, a partial image is generated by applying the imaging condition to the source and receiver wavefields. The final depth image is obtained by stacking all the partial images.

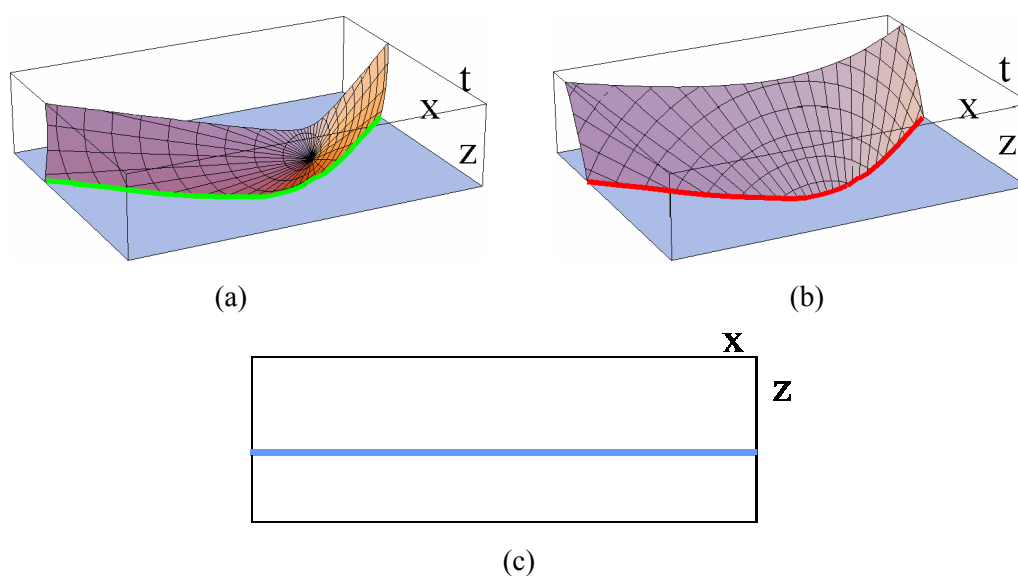


Figure 2.12: Schematic implementation of a wavefield-continuation migration based on the wavefield extrapolation. (a) Forward extrapolate the source wavefield by modeling; (b) backward extrapolate the receiver wavefield; (c) the horizontal reflector is imaged by applying imaging condition (figure courtesy Bancroft).

Given the source and receiver wavefields, an imaging condition is used to obtain

reflectivity of subsurface structures. A practical way to compute the reflectivity, as suggested by Claerbout (1971), is to apply the cross-correlation imaging condition

$$r(x, z) = \sum_{x_s} \sum_{\omega} \hat{p}_R(x, z, \omega, x_s) \hat{p}_S^*(x, z, \omega, x_s), \quad (2.34)$$

where the reflectivity  $r(x, z)$  is obtained by multiplying the extrapolated receiver wavefield  $\hat{p}_R$  by the complex conjugate of the extrapolated source wavefield  $\hat{p}_S$  in the  $x$ - $\omega$  domain, and summing over the frequencies  $\omega$  and source locations  $x_s$ . The right hand side of equation (2.34) can also be interpreted as the zero lag of the cross-correlation of the source and receiver wavefields in the time domain. This is consistent with Claerbout's definition that a reflector exists at the points where the source and the receiver wavefields coincide in time. For relative-amplitude-preserving (RAP) migration, a deconvolution-type imaging condition is required (see, Valenciano et al., 2002; Kelly and Ren, 2003). Since the intent of this thesis is not RAP migration, a simple cross-correlation imaging condition is sufficient.

## 2.6 Chapter summary

The theory of three  $x$ - $\omega$  extrapolators is reviewed in this Chapter. All three are based on the one-way wave equation and approximate the desired extrapolator in different ways. The Rayleigh extrapolator is derived from the analytical formula for the exact constant-velocity phase-shift extrapolator, and has the potential advantage of handling irregular geometry and rough topography of land data. Unfortunately, the Rayleigh extrapolator is not stable when applied in a wavefield-continuation migration. A Gaussian taper, as suggested by Nautiyal, is a straightforward way to stabilize the

Rayleigh extrapolator in the  $x-\omega$  domain. The Hale extrapolator is designed in the  $k_x-\omega$  domain and then implemented in the  $x-\omega$  domain as a convolutional filter. It is sufficiently stable by design. A comprehensive stability and accuracy analysis for all three extrapolators is presented in Chapter 3.

## Chapter Three: STABILITY AND ACCURACY OF THREE EXTRAPOLATORS

A theoretical introduction to three recursive wavefield extrapolators was presented in Chapter 2. Although equations presented there describe these extrapolators, it is worthwhile visualizing the various extrapolators to gain an intuitive understanding of their features. In addition to the illustrations of the 19-point extrapolators in Chapter 2, I also show the 39-point extrapolators in the  $k_x$ - $\omega$  domain and compare them with the desired phase-shift extrapolator.

The main content of this chapter is an analysis of the stability and accuracy of the three extrapolators. A common set of tools has been developed for stability and accuracy analysis, including 3-D error plots, error contours, zero-offset impulse-response, prestack dip accuracy, and complex imaging using the Marmousi dataset. By coding the extrapolators in Matlab<sup>®</sup>/Maple<sup>®</sup> and comparing them using the same set of tools and display methods, a fair judgement can be made of their relative performance.

### 3.1 Three extrapolators in the wavenumber-frequency domain

The three extrapolators are plotted in the  $k_x$ - $\omega$  domain so that a direct comparison can be made with the exact constant-velocity phase-shift operator (Figure 3.1 and Figure 3.2). To be consistent with the literature (e.g., Hale (1991) and Nautiyal et al. (1993)), the operator lengths are chosen as 19 and 39 points. Figure 3.1 is a collection of the figures of the 19-point extrapolators illustrated in Chapter 2. They are duplicated in this chapter for comparison with the 39-point extrapolators (Figure 3.2). The parameters used for the extrapolator calculation are the same as those in Chapter 2.

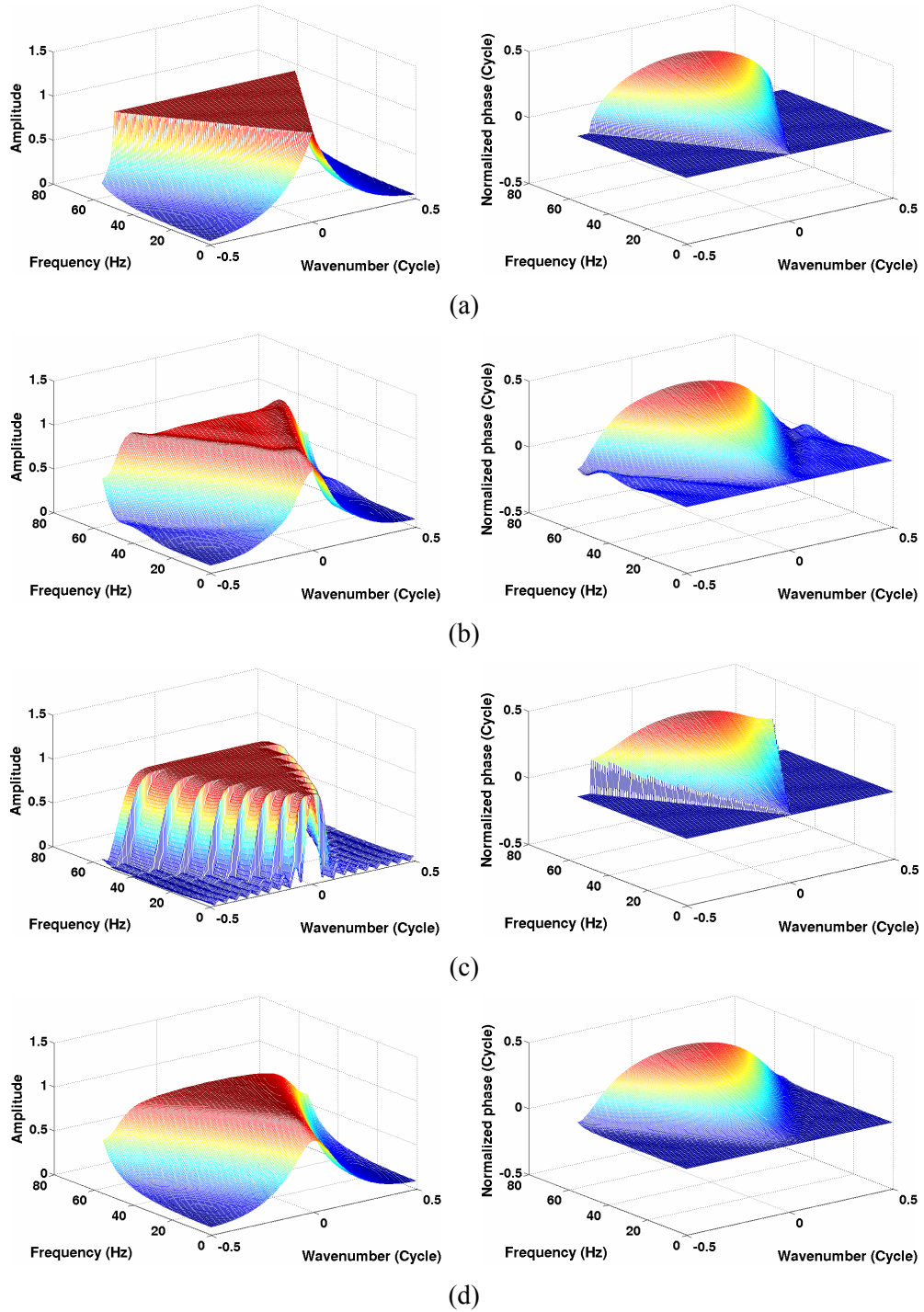
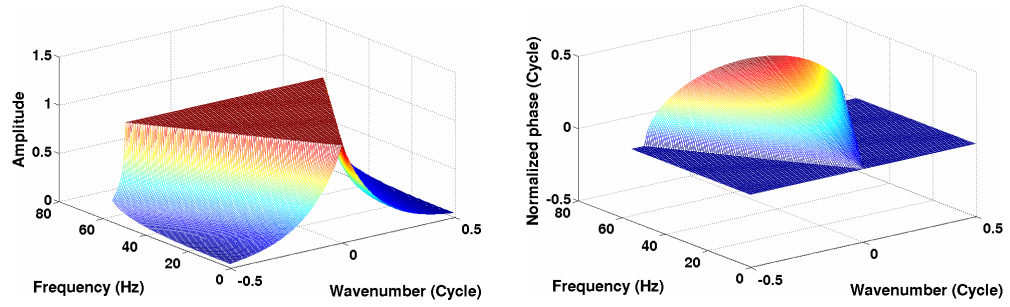
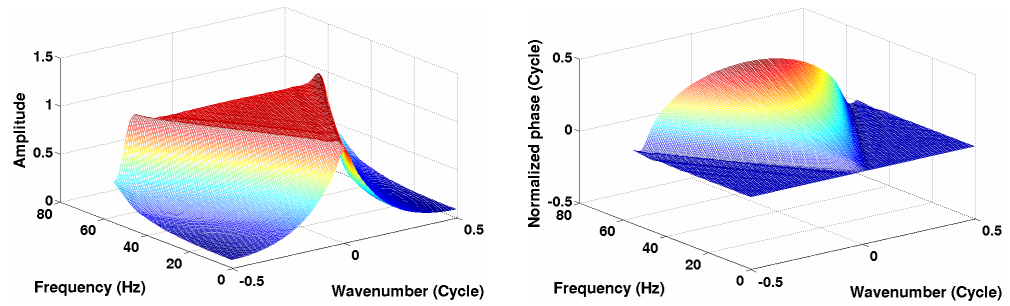


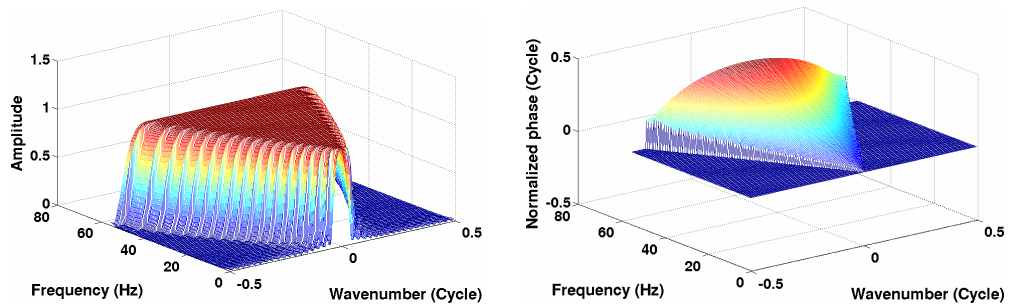
Figure 3.1: 3-D plot of various band-limited extrapolators in the  $k_x$ - $\omega$  domain. Amplitude spectra are on the left, and phase spectra are on the right. (a) The desired extrapolator (from equation (2.21)); (b) the Hanning edge-tapered Rayleigh extrapolator; (c) the Hale extrapolator; (d) the Nautiyal extrapolator. An operator length of 19 points is used by operators (b), (c) and (d) in the space domain. The phase spectrum of the Hale extrapolator is zeroed outside the evanescent boundaries (see discussion in Section 2.3).



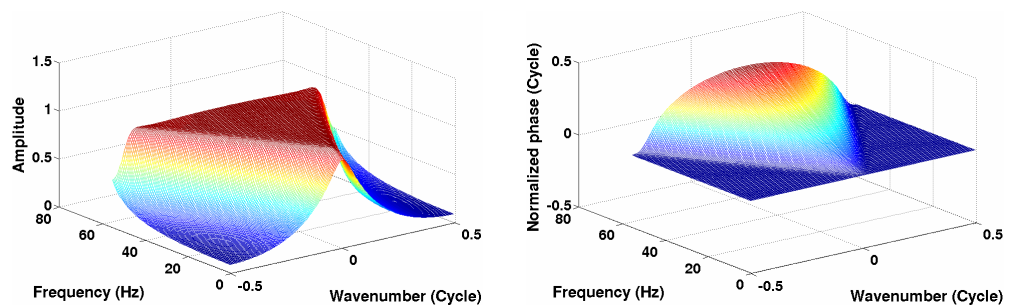
(a)



(b)



(c)



(d)

Figure 3.2: 3-D plot of various band-limited extrapolators in the  $k_x$ - $\omega$  domain. The figures on the left are the amplitude spectra and on the right are the phase spectra. (a) The desired extrapolator; (b) the Hanning edge-tapered Rayleigh extrapolator; (c) the Hale extrapolator; (d) the Nautiyal extrapolator. An operator length of 39 points is used by operators (b), (c) and (d) in the space domain. The phase spectrum of the Hale extrapolator is zeroed outside the evanescent boundaries.

Figure 3.1 and Figure 3.2 illustrate that the various  $x$ - $\omega$  extrapolators approximate the desired phase-shift operator in different ways. Although Thorbecke et al. (2004) has similar 3-D plots of his weighted least-squares extrapolator, I developed this particular visualization of the extrapolators independently in 2003.

Figure 3.1a and Figure 3.2a are the spectra of the desired extrapolator (phase-shift operator) obtained from equation (2.21). Wavenumber and phase are normalized by the factors of  $2\pi/\Delta x$  and  $2\pi$ , respectively. A Hanning edge taper (see equation (2.20)) has been applied to the Rayleigh extrapolators in the space domain (Figure 3.1b and Figure 3.2b). Reasonable taper lengths are 5 points for the 19-point extrapolator and 10 points for the 39-point extrapolator.

### 3.2 Stability analysis

A standard method for assessing the stability of an extrapolator is to evaluate its amplitude spectrum in the  $k_x$ - $\omega$  domain for each frequency (e.g., Nautiyal, 1990). Here I show the extrapolators at an example frequency of 31.25Hz.

The 19-point and 39-point Rayleigh extrapolators with abrupt truncation are shown in Figure 3.3a and Figure 3.3c respectively as thin blue lines. The amplitude oscillation in the wavenumber domain is caused by spatial truncation of the extrapolator and the Gibbs' phenomena. As a result, after 100 extrapolation steps, the wavefield energy at certain wavenumbers will be amplified approximately by a factor of 170 (19-point extrapolator, Figure 3.3b) and 41 (39-point extrapolator, Figure 3.3d). From Figure 3.3a and Figure 3.3c, it is evident that a simple Hanning edge taper applied to the extrapolator in the space domain (thick green lines) attenuates the ripples. However,

stability cannot be guaranteed after a number of extrapolation steps (thick green lines in Figure 3.3b and Figure 3.3d): the longer the extrapolator, the better the stability. In the extreme case where full aperture is used (Figure 3.3e and Figure 3.3f), the instability is much less severe than with the 19- and 39-point extrapolators. Here, full aperture means that the length of the extrapolator is equal to the spatial extent of the finite wavefield (200 points in this example).

Mathematically, a Rayleigh extrapolator can never be stable. As long as the Gibbs' phenomenon is present, the amplitude will increase to an unacceptable level. After a certain number of extrapolation steps, the final image will be distorted. Practically, since the number of extrapolation steps is always finite, we set a tolerance value for the amplitude amplification so that the distortion is acceptable. The tolerance value depends on the number of extrapolation steps, amplitude error, and a personal judgment of acceptable distortion. Given this tolerance value, the Rayleigh extrapolator will be reasonably stable for a finite number of extrapolation steps. Therefore, when we deal with land data that has irregular geometry and rough topography, the Rayleigh extrapolator can be used for the first few steps followed by another stable extrapolator for the remaining steps.

In contrast, the 19- and 39-point Hale extrapolators are sufficiently stable. As depicted in Figure 3.4, the amplitude of the wavefield energy will not grow with recursive wavefield extrapolation. This is obvious from the design of the Hale extrapolator, whose amplitude at each frequency never exceeds  $I + \varepsilon$ , where  $\varepsilon$  is defined in Chapter 2 as a small error tolerance ( $10^{-4}$ ).

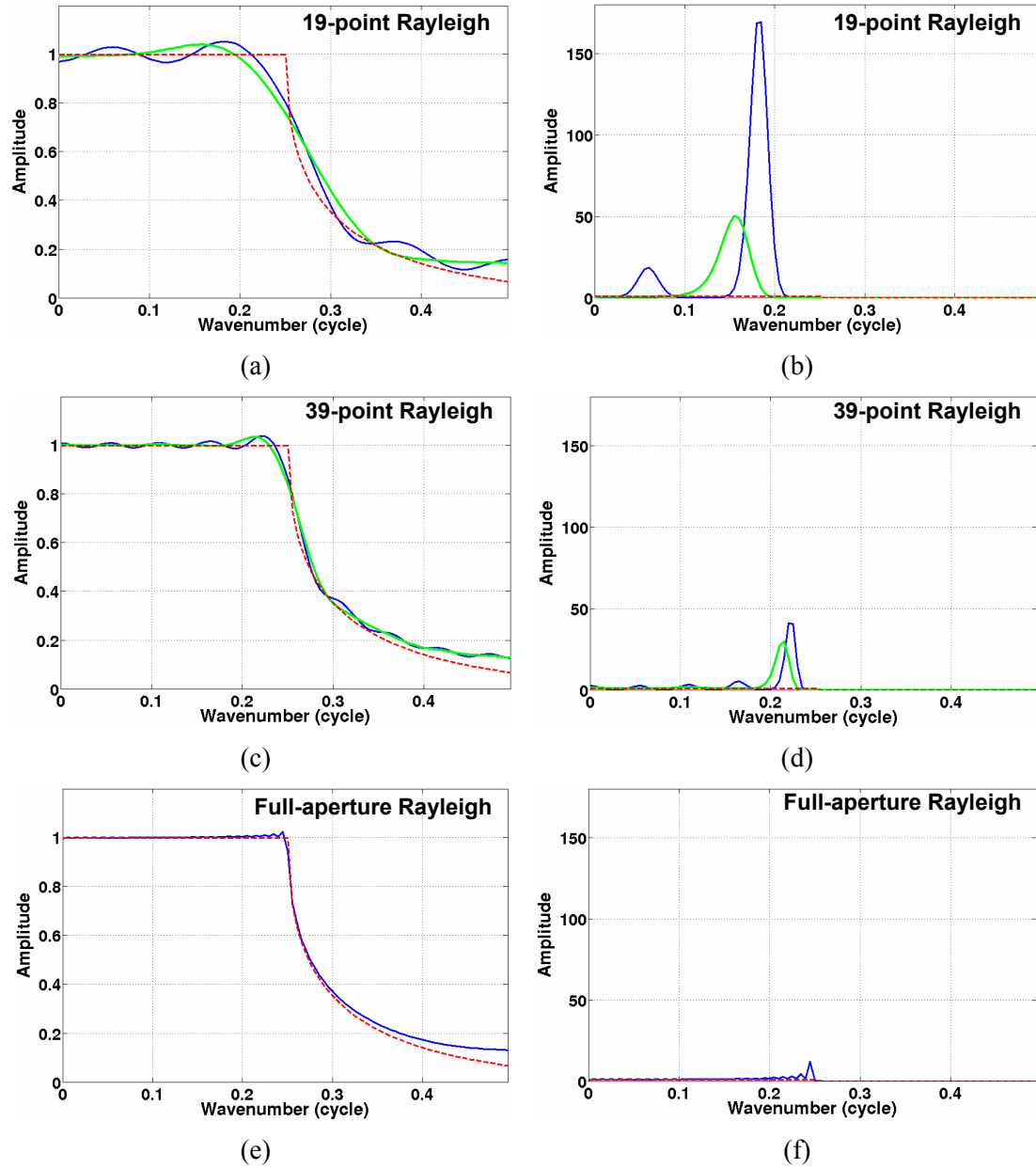


Figure 3.3: Amplitude spectra of the Rayleigh extrapolators at the frequency of 31.25 Hz (only positive wavenumbers are plotted). The evanescent boundary is at  $k_x=0.25$ . The dashed red lines are the amplitude spectra of the desired extrapolator. (a) 19-point Hanning-tapered (thick green line) and truncated extrapolator (thin blue line); (c) 39-point Hanning-tapered (thick green line) and truncated extrapolator (thin blue line); (e) full-aperture extrapolator. The figures on the right ((b), (d) and (f)) show the amplification of the wavefield energy after 100 extrapolation steps.

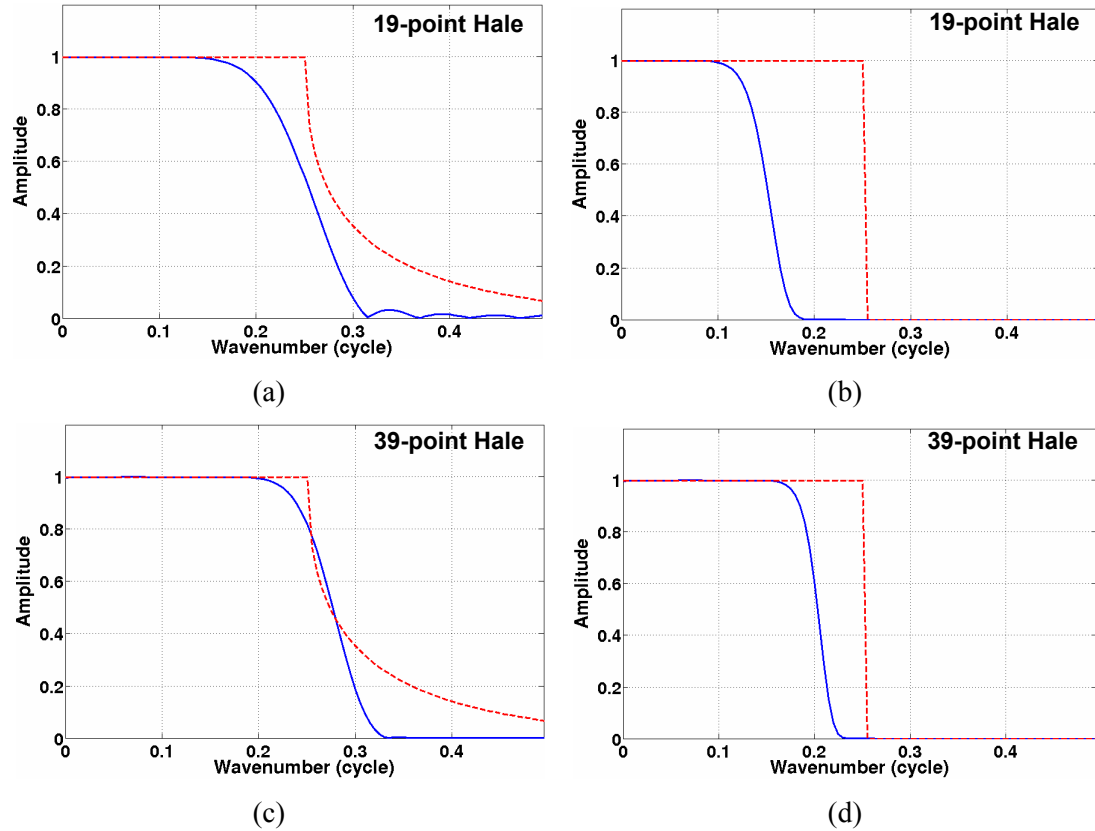


Figure 3.4: Amplitude spectra of the Hale extrapolators at the frequency of 31.25 Hz (blue lines - only positive wavenumbers are plotted). The evanescent boundary is at  $k_x=0.25$ . The dashed red lines are the amplitude spectra of the desired extrapolator. (a) 19-point extrapolator; (c) 39-point extrapolator. Figures on the right ((b) and (d)) show the amplification of the wavefield energy after 100 extrapolation steps.

The Nautiyal extrapolator (Figure 3.5) is reasonably stable after the same number of extrapolation steps when compared to the Hale extrapolator; however, it attenuates more of the wavefield at high-angles of propagation (i.e., at large wavenumbers). It appears that the 39-point Nautiyal extrapolator is starting to amplify the wavefield energy after 100 steps (Figure 3.5d). This can be remedied by adjusting the  $\gamma$  parameter of the Gaussian window (see equation (2.33)). Nevertheless, according to Nautiyal et al. (1993), all the Gaussian windows share a common  $\gamma$  when tapering the extrapolators at various frequencies. Therefore, adjusting  $\gamma$  will result in amplitude amplification/attenuation at other frequencies. Thus, the stability of the Nautiyal extrapolator is achieved at the cost

of accuracy. The truncation of the Gaussian window in the space domain will still cause oscillation in the wavenumber domain. This becomes evident after a number of extrapolation steps (Figure 3.5b and Figure 3.5d). However, by comparing Figure 3.3 and Figure 3.5, the Gaussian window has greatly attenuated the amplitude ripples. Therefore it is more stable than the Hanning edge-tapered Rayleigh extrapolator.

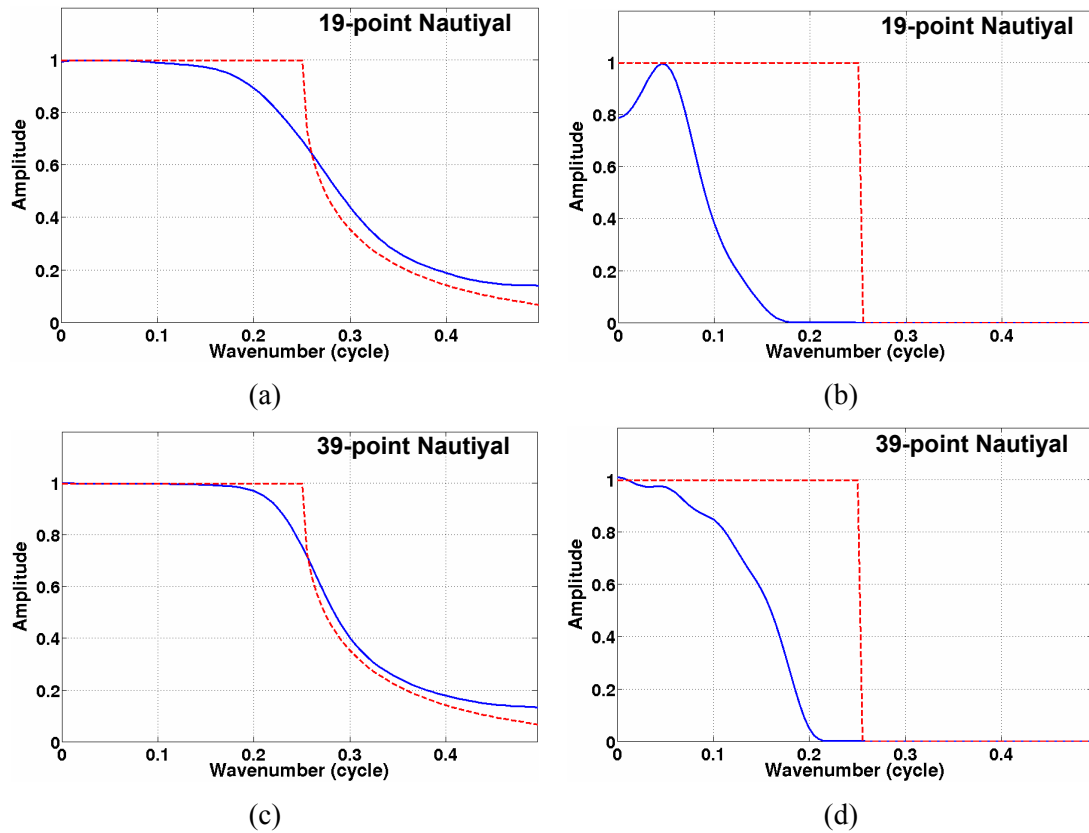


Figure 3.5: Amplitude spectra of the Nautiyal (Gaussian tapered) extrapolators at the frequency of 31.25 Hz (blue lines - only positive wavenumbers are plotted). Evanescent boundary is at  $k_x=0.25$ . The red dashed lines are the amplitude spectra of the desired extrapolator. (a) 19-point extrapolator; (c) 39-point extrapolator. Figures on the right ((b) and (d)) are the amplification/attenuation of the wavefield energy after 100 steps extrapolations.

The analysis also indicates that a full Hanning-tapered Rayleigh extrapolator (where the length of the full Hanning window equals to the length of the extrapolator) is similar to the Nautiyal extrapolator (Figure 3.6). Although it is not guaranteed to be

stable (Figure 3.6b), it is much more stable than the Hanning edge-tapered Rayleigh extrapolator (Figure 3.3). In addition, it preserves more wavefield energy at high wavenumbers and thus is more accurate than the Nautiyal extrapolator.

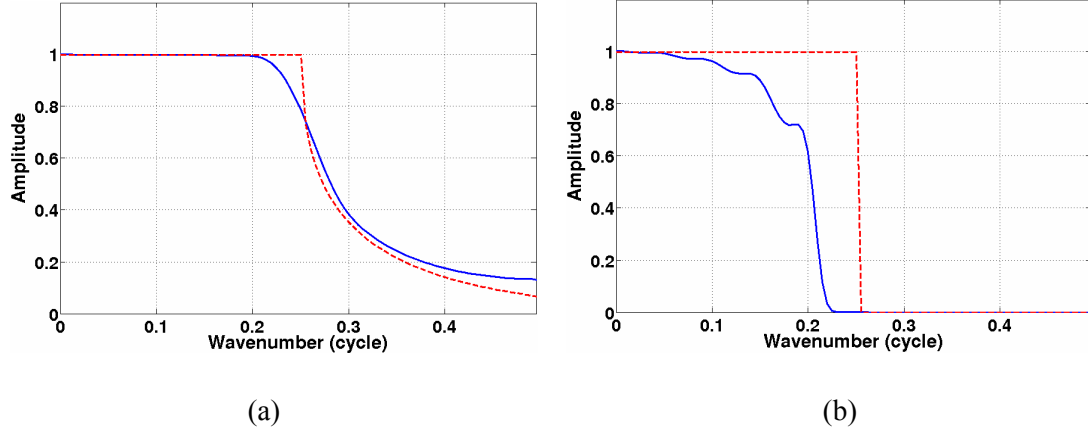


Figure 3.6: Amplitude spectra of the full Hanning-tapered Rayleigh extrapolator at the frequency of 31.25 Hz (blue lines). The evanescent boundary is at  $k_x=0.25$ . The red dashed lines are the amplitude spectra of the desired extrapolator. (a) The 39-point Rayleigh extrapolator; (b) the attenuation of the wavefield energy after 100 extrapolation steps.

### 3.3 Accuracy analysis

In order to conduct analysis of accuracy, 3-D error plots (Figure 3.7-Figure 3.10) are generated by subtracting the desired extrapolator from the various extrapolators. The evanescent boundaries are superimposed on the figures as dashed red lines.

In this thesis, I define the amplitude and phase errors as

$$\Delta A(k_x, \omega) = A_{\text{designed}}(k_x, \omega) - A_{\text{desired}}(k_x, \omega) \quad (3.1)$$

and

$$\Delta \Theta(k_x, \omega) = \Theta_{\text{designed}}(k_x, \omega) - \Theta_{\text{desired}}(k_x, \omega), \quad (3.2)$$

where  $A$  and  $\Theta$  are the amplitude and phase of the extrapolators in the  $k_x$ - $\omega$  domain,

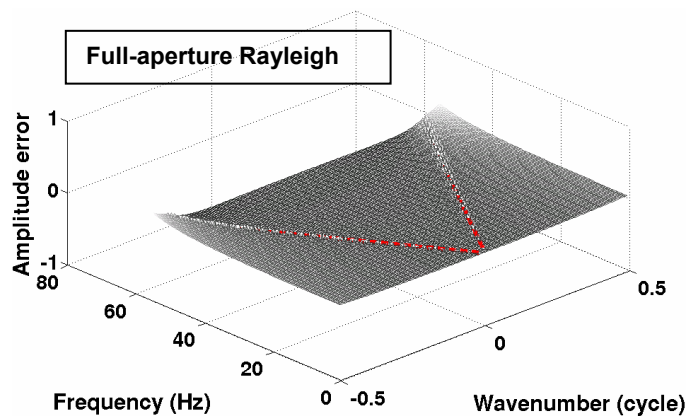
respectively.

The amplitude error and phase error can be explained using the concept of plane wave superposition. Assuming lateral homogeneity, the  $x$ - $\omega$  wavefield extrapolation can be implemented in the  $k_x$ - $\omega$  domain as a multiplication of the input wavefield and the wavefield extrapolator (equation (2.6)). Generally, a 2-D inverse Fourier transform of the extrapolated wavefield from the  $k_x$ - $\omega$  domain to the  $x$ - $t$  domain is equivalent to a wavefield reconstruction by superposing plane waves traveling at various angles. The horizontal wavenumber  $k_x$  and the frequency  $\omega$  are associated with the propagation angle  $\theta$  of plane waves by

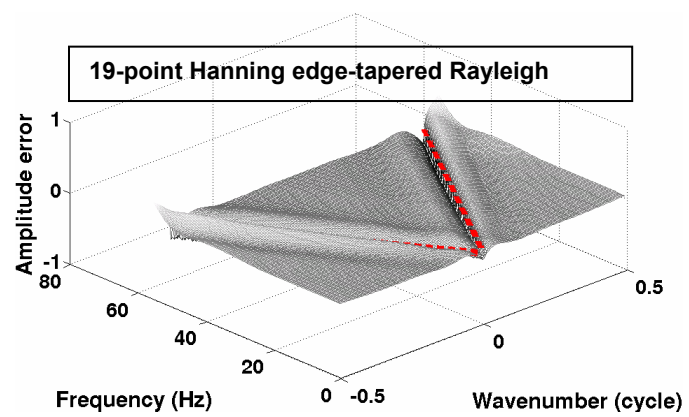
$$k_x = \frac{\omega}{v} \sin \theta, \quad (3.3)$$

where  $\theta$  is the propagation angle measured from the vertical direction. For propagating waves, the wavenumber is subject to the constraint that  $|k_x| < \omega/v$  which is known as the evanescent boundary. From equation (3.1), (3.2) and (3.3), a positive amplitude error  $\Delta A$  at  $(k_x, \omega)$  indicates that the designed extrapolator will exponentially amplify the wave traveling at the angle  $\theta = \sin^{-1}(k_x v / \omega)$ , which makes the extrapolator unstable; whereas a negative amplitude error  $\Delta A$  means that the designed extrapolator tends to attenuate the wavefield at that angle. A correct phase will ensure that plane waves are properly shifted such that they can reconstruct the extrapolated wavefield (through the 2-D inverse Fourier transform) but deconstruct the undesired artifacts. Positive and negative phase errors will incorrectly shift the plane waves. Slight phase errors may result in a reconstructed wavefield with artifacts; serious phase errors may totally distort the

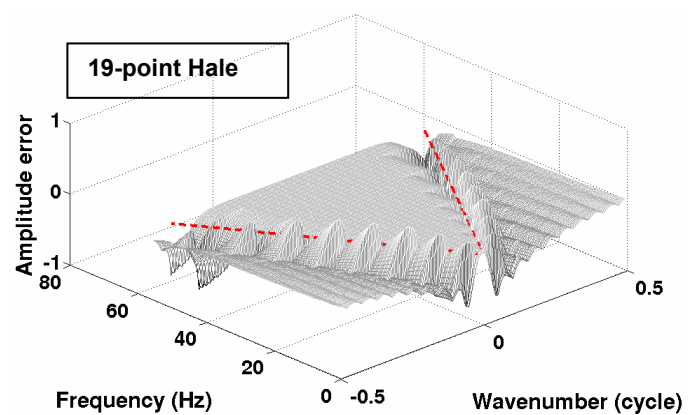
reconstructed wavefield.



(a)



(b)



(c)

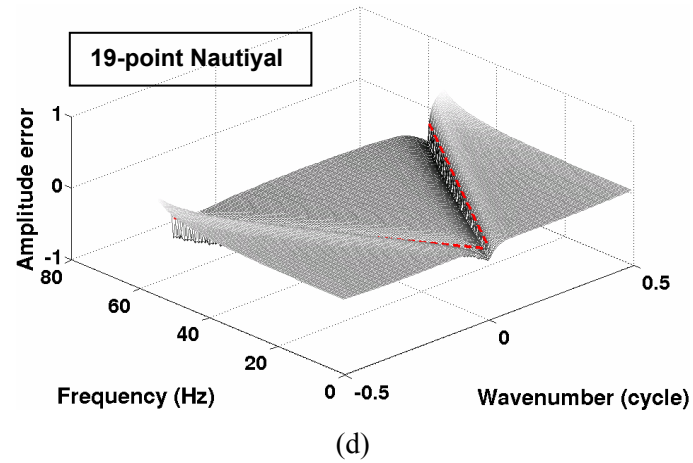
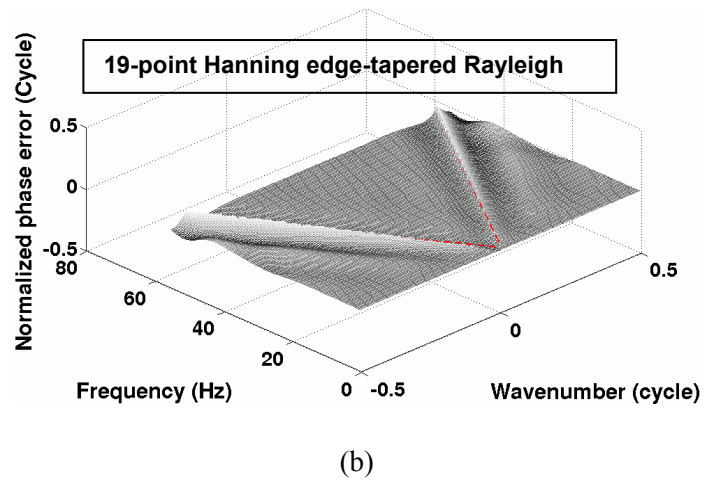
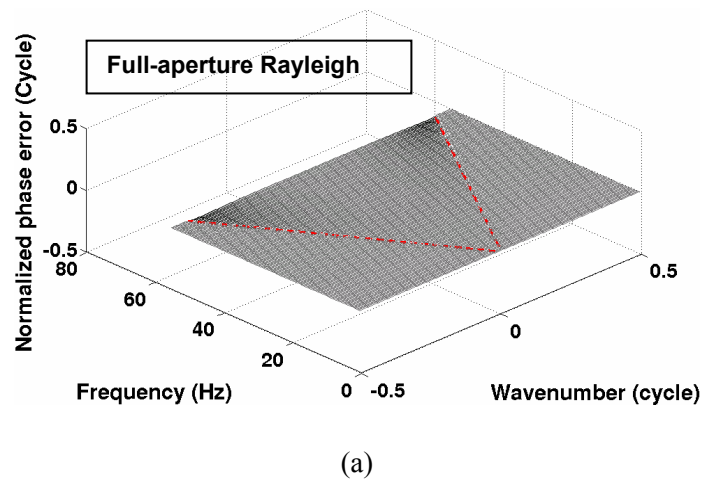
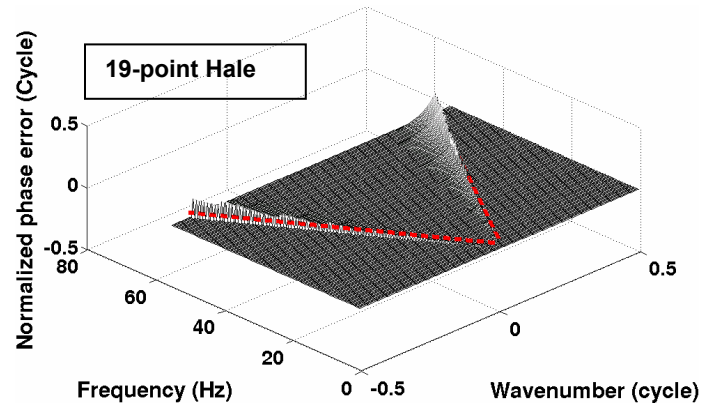
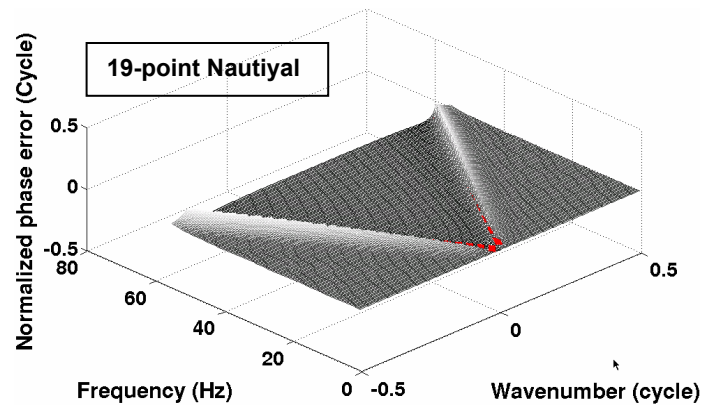


Figure 3.7: Amplitude errors of (a) the full-aperture Rayleigh extrapolator, the 19-point (b) Hanning-tapered Rayleigh extrapolator, (c) Hale extrapolator, and (d) Nautiyal extrapolator. The dashed red lines are the evanescent boundaries.



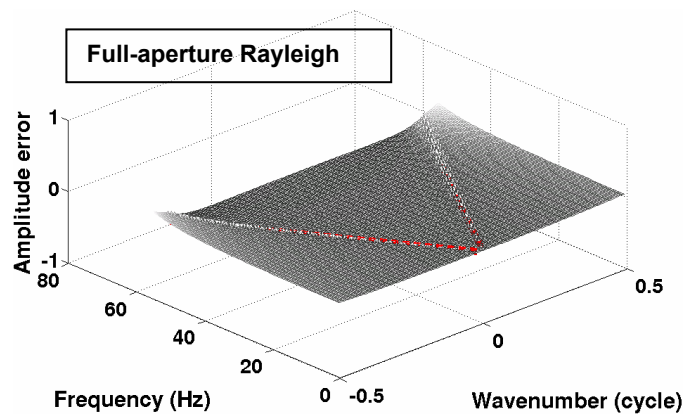


(c)

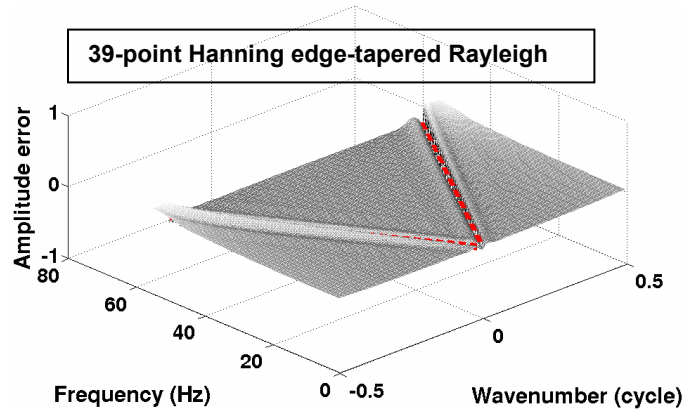


(d)

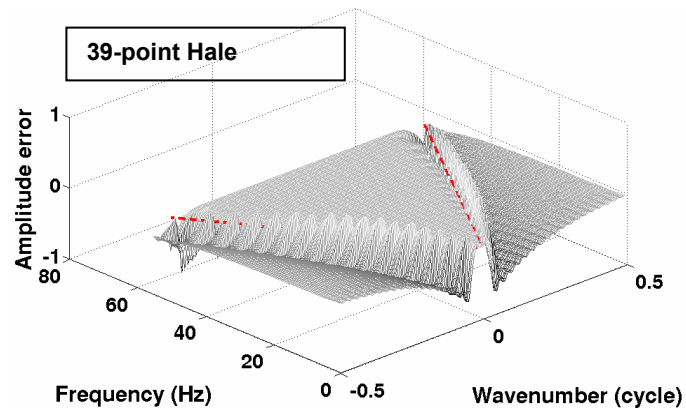
Figure 3.8: Phase errors of (a) the full-aperture Rayleigh extrapolator, the 19-point (b) Hanning-tapered Rayleigh extrapolator, (c) Hale extrapolator, and (d) Nautiyal extrapolator. The dashed red lines are the evanescent boundaries. The phase error spectrum of the Hale extrapolator is zeroed outside the evanescent boundaries (see discussion in Section 2.3).



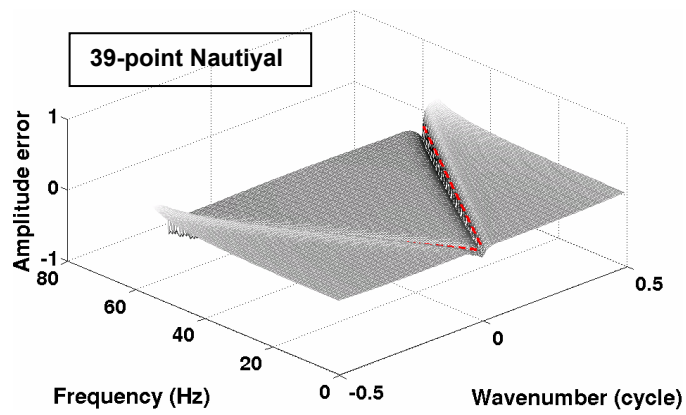
(a)



(b)

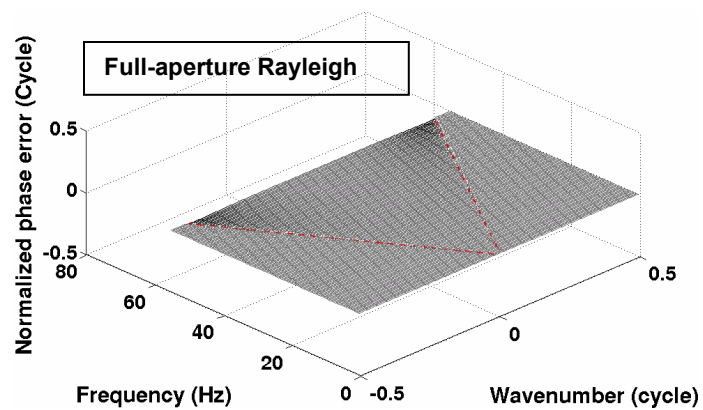


(c)

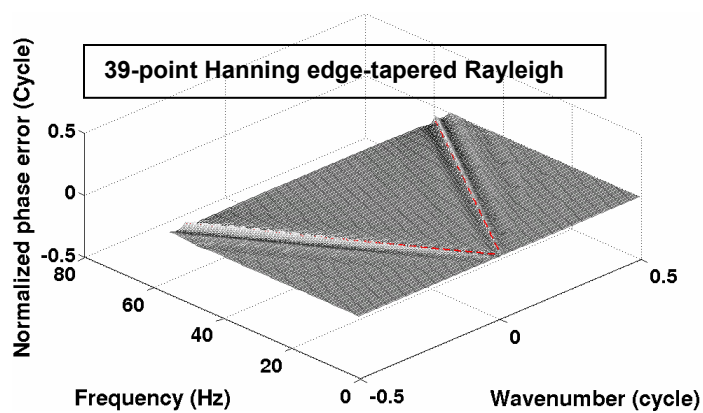


(d)

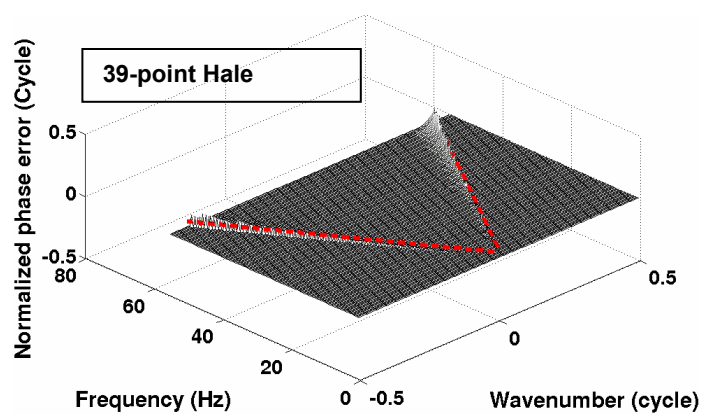
Figure 3.9: Amplitude errors of (a) the full-aperture Rayleigh extrapolator, the 39-point (b) Hanning-tapered Rayleigh extrapolator, (c) Hale extrapolator, and (d) Nautiyal extrapolator. The dashed red lines are the evanescent boundaries.



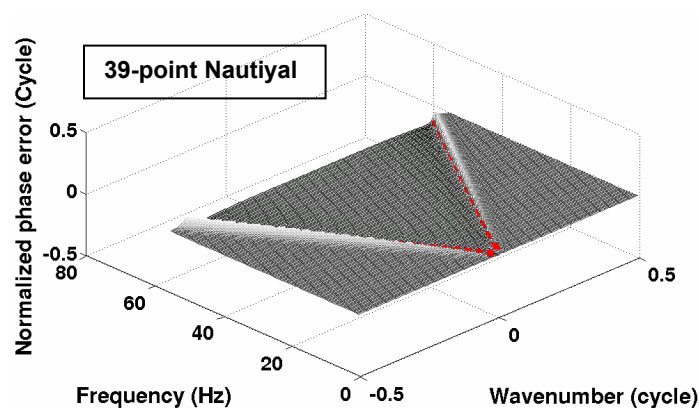
(a)



(b)



(c)



(d)

Figure 3.10: Phase errors of (a) the full-aperture Rayleigh extrapolator, the 39-point (b) Hanning edge-tapered Rayleigh extrapolator, (c) Hale extrapolator, and (d) Nautiyal extrapolator. The dashed red lines are the evanescent boundaries. The phase error spectrum of the Hale extrapolator is zeroed outside the evanescent boundaries (see discussion in Section 2.3).

An evaluation of the error figures indicates that longer extrapolators are more accurate. By comparing the error figures, the full-aperture Rayleigh extrapolator (Figure 3.7a and Figure 3.8a) shows the smallest amplitude and phase errors in comparison to other “limited-aperture” extrapolators<sup>8</sup>. However, there are number of reasons why full-aperture extrapolation is less desirable in practice. First, full-aperture extrapolation is computationally expensive, especially in 3-D. Second, the finite aperture in the space domain causes oscillations in the wavenumber domain with a resultant amplification or attenuation of portions of the wavefield (see Figure 3.3e and Figure 3.3f). Therefore, full-aperture extrapolation can be, at best, only reasonably stable for a finite number of extrapolation steps. Third, it is important to note that, even at infinite aperture, we always choose to attenuate the evanescent region and are thus making errors for inverse extrapolation (see, Wapenaar et al., 1997).

---

<sup>8</sup> Strictly speaking, “full-aperture” is also limited-aperture due to the finite acquisition survey or limited spatial extent of the data after zero padding. In this paper, the “limited-aperture” refers to the case where the full aperture is not used.

Both the Hale extrapolator and the Nautiyal extrapolator are designed to stabilize recursive wavefield extrapolation. However, differences in their design result in differences in accuracy. Taking advantage of the Gaussian window (i.e. the Fourier transform of a Gaussian is another Gaussian), the Nautiyal extrapolator is like a “smoothed” version of the exact extrapolator (Figure 3.1d and Figure 3.2d) where the oscillation is suppressed but high angle propagation of the wavefield (at large wavenumbers) is also attenuated (Figure 3.5). The fact that the phase error is not zero at small wavenumbers (Nautiyal (1993); Figure 2.11b) makes it less accurate. In contrast, the Hale extrapolator achieves better accuracy by matching the first few terms in a Taylor series expansion of the exact extrapolator. Figure 3.7c - Figure 3.10c indicate that the Hale extrapolators are more accurate within the evanescent boundary. Unfortunately, the nature of the design for the Hale extrapolator will cause blocky spectra in the  $k_x$ - $\omega$  domain (Figure 3.1c and Figure 3.2c). As we will see later, the discontinuities between each frequency bands result in high-angle artifacts that would cancel if there were energy in between the high wavenumber gaps. In addition, the Hale extrapolator is not accurate at high propagation angles because it is derived from a Taylor series expansion at  $k=0$ . This loss of accuracy is identified in Figure 3.7c - Figure 3.10c as an increase in amplitude and phase errors at larger wavenumbers.

The method described above for evaluating accuracy of the various extrapolators is qualitative. A quantitative approach is to investigate how the errors are associated with propagation angle. By remapping the error matrices from the  $k_x$ - $\omega$  domain to the frequency-angle ( $\omega$ - $\theta$ ) domain (based on equation (3.3)), the amplitude and phase errors (the designed minus the desired) can be contoured as a function of the frequency and

propagation angle (Figure 3.11). The amplitude error contour values are  $-1/20$  (solid green line),  $-1/200$  (solid black line),  $1/20$  (dashed green line) and  $1/200$  (dashed black line); the phase error contour values are  $\pi/100$  (solid green line),  $\pi/1000$  (solid red line),  $-\pi/1000$  (dashed red line).

In general, the errors from the 39-point Hale extrapolator are more or less independent of frequency. Figure 3.11c indicates that one extrapolation step using the 39-point Hale extrapolator will attenuate waves propagating at about  $55^\circ$  by a factor of 0.995 (i.e.,  $1-1/200$ ) for most frequencies. A 200-step extrapolation will attenuate these waves by a factor of  $0.995^{200} = 0.367$ . Similarly, waves propagating at about  $70^\circ$  will be attenuated by a factor of  $0.95^{20} = 0.359$  after 20 steps. Given that phase errors accumulate, the phase error contour shown by Figure 3.11d indicates that one-half cycle ( $\pi$  radians) phase error will be generated after 1000 extrapolation steps for waves propagating at about  $55^\circ$ , while it only takes 100 steps for the waves propagating at about  $70^\circ$ . Therefore, waves with inaccurate phases are rapidly attenuated during the extrapolation to ensure a proper wavefield reconstruction.

The errors from 39-point Hanning-tapered Rayleigh extrapolator and Nautiyal extrapolator tend to be frequency-dependent. Unlike the error contours of the Hale extrapolator, where amplitude errors are all negative (therefore stable) and phase error are all positive, the error contours of the Hanning-tapered Rayleigh extrapolator are both positive and negative. Figure 3.11a suggested that the 39-point Hanning-tapered Rayleigh extrapolator will attenuate waves propagating at  $60^\circ$ - $70^\circ$  by a factor of 0.367 after 200 extrapolation steps for the normalized frequency range of 0.15-0.5 (see solid black line).

The positive amplitude error (dashed lines in Figure 3.11a) indicates that the waves propagating at lower angles will be amplified by a factor of  $(1+1/200)^{200} = 2.7115$  after 200 steps. This suggests that the lower angle waves will become dominant after a number of steps, which is also an indication of the instability. A half-cycle phase error will be generated after 1000 steps for the wave propagating at 70°-80° degrees (solid red line in Figure 3.11b). However, the waves with positive phase errors are quickly attenuated due to the negative amplitude error, as happens with the Hale extrapolator. The lower angle propagating waves have the opposite phase change due to the negative phase error (dashed red lines in Figure 3.11b). Notice that the negative phase error contour (dashed red lines in Figure 3.11b) covers an angle range similar to the one covered by positive amplitude contour (dashed black lines in Figure 3.11a). Waves propagating at these angles will be amplified due to a positive amplitude error. The amplification of the waves with phase errors makes the Hanning-tapered Rayleigh extrapolator unstable and inaccurate, and therefore not suitable for a large-number of extrapolation steps.

The amplitude errors of the 39-point Nautiyal extrapolator are predominantly negative<sup>9</sup> (Figure 3.11e) which ensures that very few propagating wavefields will be amplified (therefore stable). However, it is probably the least accurate extrapolator as shown by Figure 3.11e and Figure 3.11f. Waves propagating at 35° will be attenuated by a factor of 0.367 after 200 extrapolation steps for the normalized frequency range of 0.15-0.3. The attenuation is even more severe at some low and high frequencies. Again, the waves with positive phase errors will be attenuated quickly, but the attenuation of the

---

<sup>9</sup> There are very small positive errors due to the truncation of Gaussian window.

waves with negative phase errors is not optimal because of the errors are frequency-dependent. The error contours of the full Hanning-tapered Rayleigh extrapolator (Figure 3.11g and h) demonstrate similar behaviours compared to the Nautiyal extrapolator. However, given the same number of extrapolation steps, it has better steep-dip capability as the contours are at higher angles than those of the Nautiyal extrapolator (Figure 3.11e and f).

Based on the above discussion, an accurate extrapolator will:

1. Attenuate most of the propagating waves with phase error.
2. Preserve most of the accurate waves.

The Hale extrapolator meets both criteria, whereas the Hanning edge-tapered Rayleigh extrapolator fails in the first, and the Nautiyal and the full Hanning-tapered extrapolators fail in the second.

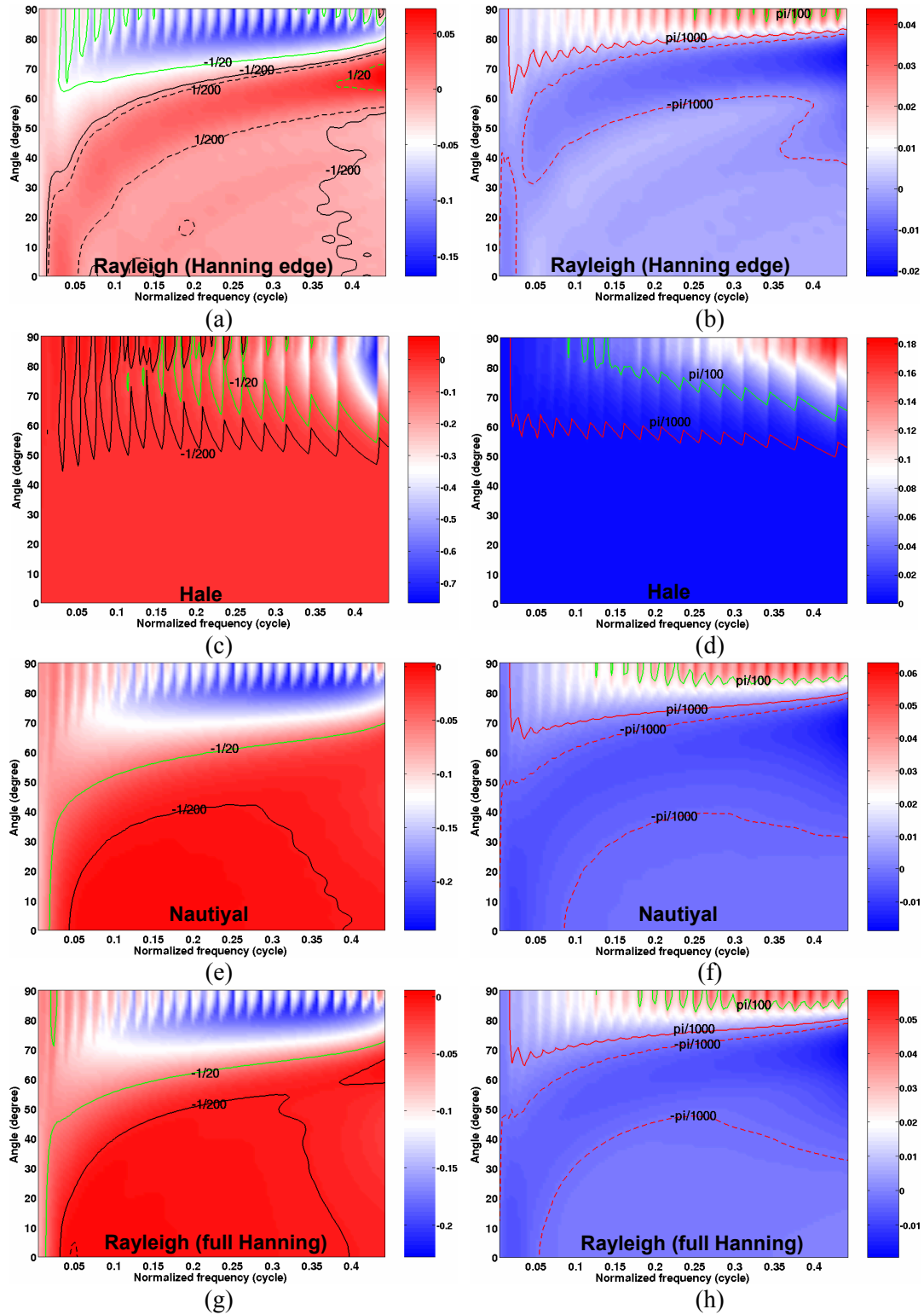


Figure 3.11: Amplitude (left) and phase (right) error contours for the 39-point Hanning edge-tapered Rayleigh extrapolator ((a) and (b)), Hale extrapolator ((c) and (d)), Nautiyal extrapolator (e) and (f), and full Hanning-tapered Rayleigh extrapolator. Frequency is normalized by multiplying  $\Delta x/v$ .

### 3.4 Zero-offset impulse responses

Zero-offset impulse responses are calculated with a half-velocity of 1250m/s, receiver spread of 2000m and maximum extrapolation depth of 2000m. The spatial sampling is  $\Delta x = \Delta z = 10\text{m}$  and the temporal sampling is  $\Delta t = 4\text{ms}$ . Three Ricker wavelets with a dominant frequency of 24Hz are seeded at  $t = 0.16, 0.32$  and  $0.48\text{s}$ , respectively. The impulse response is obtained by backward extrapolating the input wavefield and applying a poststack imaging condition (i.e., simply slice the wavefield at  $t = 0$ ). The results are shown in Figure 3.12 and Figure 3.13, with angular reference lines superimposed on the left half of the figures. The reference lines range from  $0^\circ$  to  $90^\circ$  at the interval of  $10^\circ$ . The impulse response from the exact phase-shift operator is also calculated and displayed here as the reference (Figure 3.12a).

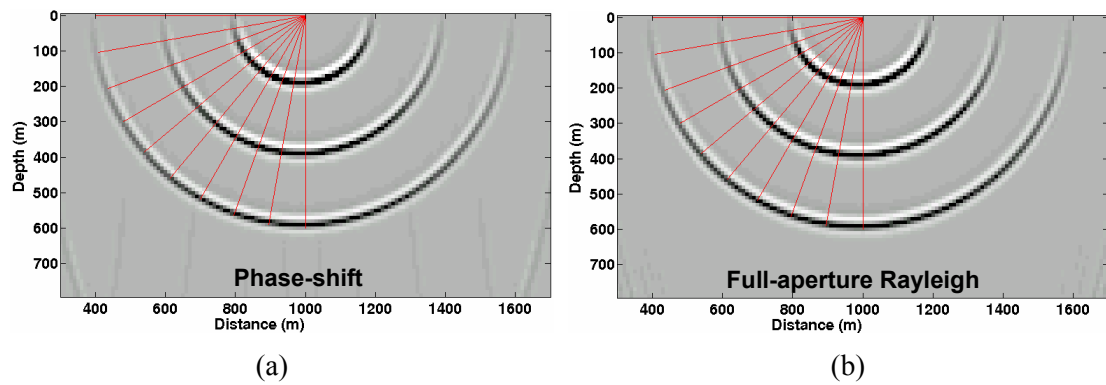


Figure 3.12: Impulse responses (zero-offset migration) of (a) the phase-shift operator and (b) the 200-point full-aperture Rayleigh extrapolator.

After 200 extrapolation steps, the impulse response for the full-aperture Rayleigh extrapolator is reasonably stable and accurate at high propagation angles (Figure 3.12b). It is nearly identical to the impulse response from the phase-shift operator (Figure 3.12a) except that it does not have the spatial wrap-around artifacts that typically appear with the phase-shift operator (see lower corners of Figure 3.12a). However, the computational cost

of a 200-point full-aperture Rayleigh extrapolator is about five times greater than a 39-point extrapolator, and 10 times greater than a 19-point extrapolator (see Figure 3.21).

In general, the 19-point extrapolators (Figure 3.13a, Figure 3.13c, Figure 3.13e and Figure 3.13g) are less accurate than the 39-point extrapolators (Figure 3.13b, Figure 3.13d, Figure 3.13f and Figure 3.13h). The Hanning edge-tapered Rayleigh extrapolators (Figure 3.13a and Figure 3.13b) preserve higher propagation angles than the other three extrapolators, but the higher angle wavefields start to become unstable and phase-rotated – an undesirable feature particularly noticeable with the 19-point Hanning-tapered extrapolator (Figure 3.13a). This confirms our observation from the stability and accuracy analysis – that the Hanning edge-tapered Rayleigh extrapolator is neither stable nor accurate.

As predicted by the error contours, the impulse response from the 39-point Hale extrapolator (Figure 3.13d) shows attenuation at about  $55^\circ$  after 200 extrapolation steps. There are also artifacts present at high propagation angles caused by discontinuities in the extrapolator (Figure 3.13c and Figure 3.13d). The 39-point Hale extrapolator (Figure 3.13d) generates fewer artifacts than the 19-point extrapolator (Figure 3.13c) because the discontinuities in the 39-point extrapolator are less severe than those in the 19-point extrapolator (compare Figure 3.1c and Figure 3.2c).

Although the Nautiyal extrapolators are stable, they have the poorest angular aperture of all tested extrapolators (Figure 3.13e and Figure 3.13f). This is not surprising in view of the amplitude error contours in Figure 3.11e. As discussed previously, tapering by a Gaussian window in the space domain is a compromise between stability and

accuracy. In addition, as indicated by the phase error contour (Figure 3.11f), there is a noticeable phase error with 39-point Nautiyal extrapolator (Figure 3.13f).

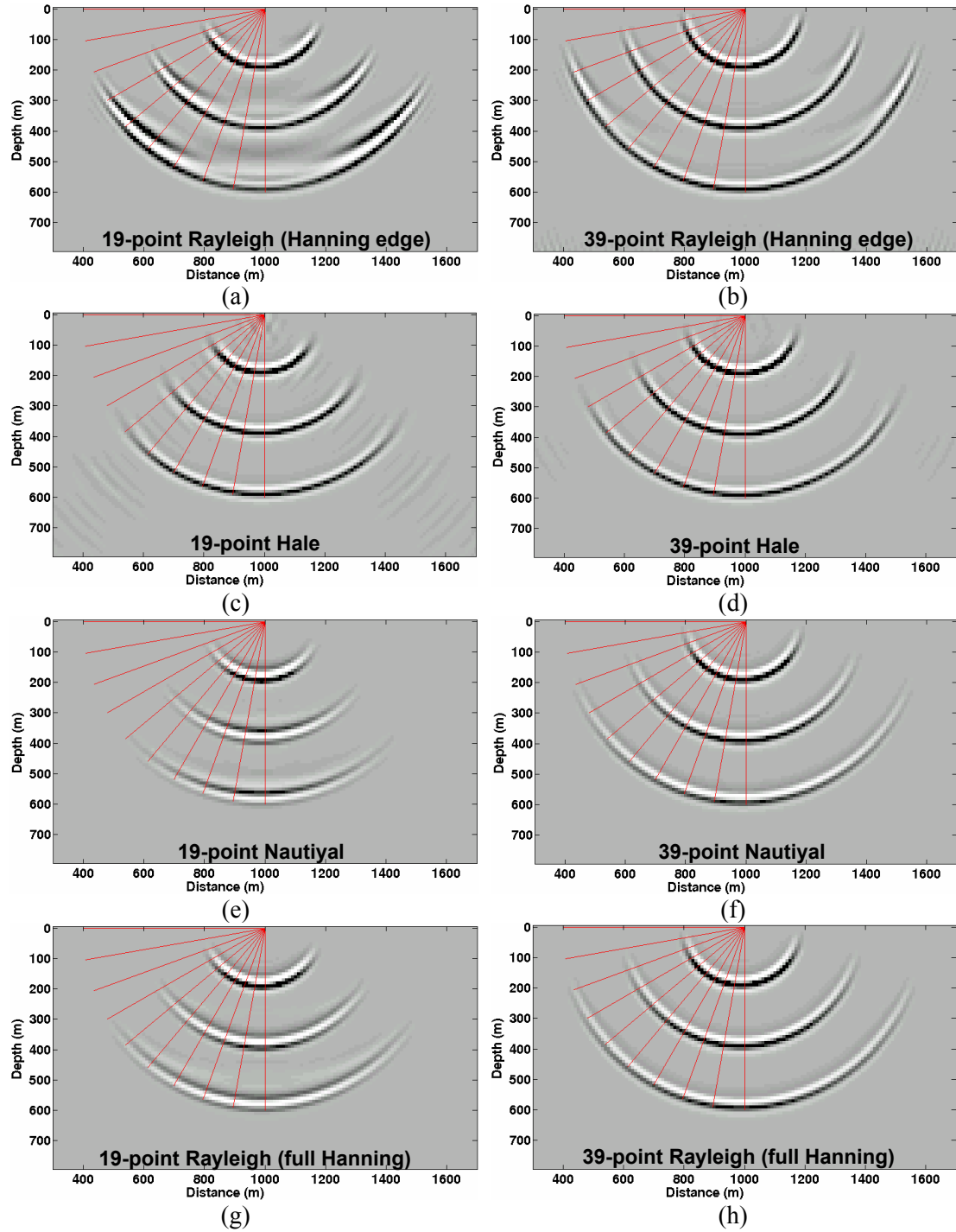


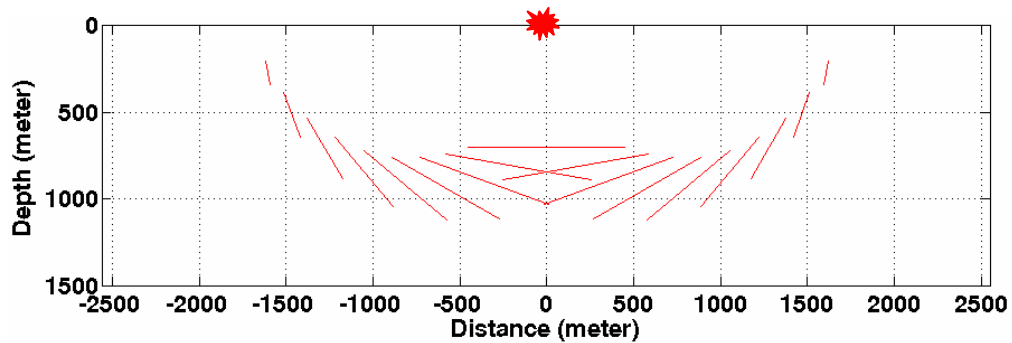
Figure 3.13: Impulse responses of the 19- and 39-point Hanning edge-tapered Rayleigh extrapolators (a and b), Hale extrapolators (c and d), Nautiyal extrapolators (e and f), and full Hanning-tapered Rayleigh extrapolators (g and h).

The full Hanning-tapered Rayleigh extrapolators are more stable than the Hanning edge-tapered ones. Their impulse responses are very similar to the ones from the Nautiyal extrapolators. However, as indicated by the error contours (Figure 3.13g and Figure 3.13h), they have relatively better dip accuracy and less phase rotation than the Nautiyal extrapolators.

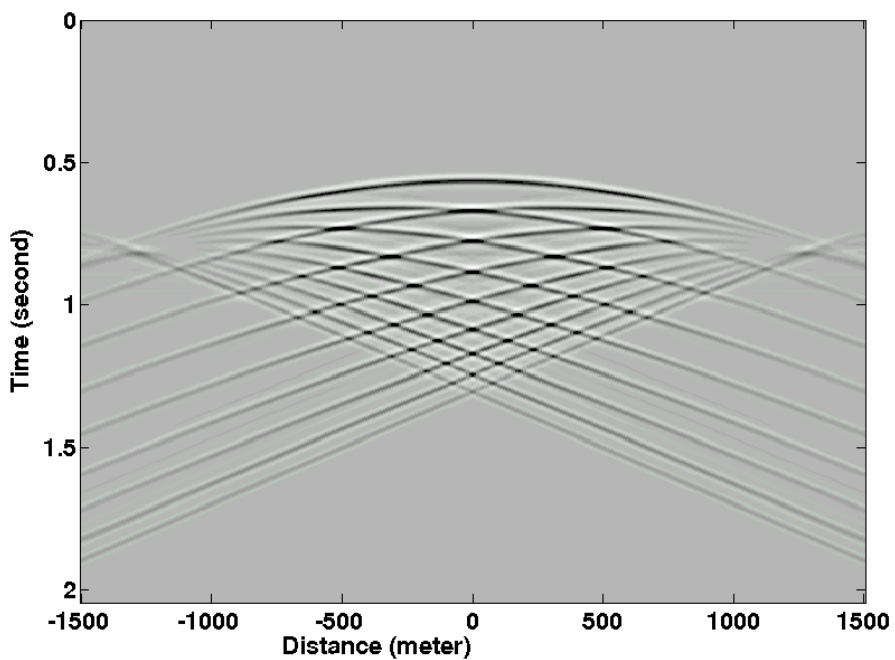
The impulse response test is a good tool for evaluating the performance of the extrapolators applied in poststack migrations. However, it is not sufficient when the extrapolators are used in prestack migrations. In the next section, a synthetic test is used to evaluate the dip accuracy of the extrapolators in prestack migrations.

### **3.5 Prestack synthetic test**

A prestack synthetic test is used to examine the accuracy of prestack depth migration based on the wavefield extrapolators studied in this thesis. The model has only one shot located at  $x=0$ . A synthetic source record (Figure 3.14b) is generated from the homogeneous model ( $v=2500\text{m/s}$ ) depicted in Figure 3.14a. The spatial sampling is  $\Delta x=\Delta z=10\text{m}$  and the temporal sampling is  $\Delta t=4\text{ms}$ . The model contains 17 dipping reflectors at the dip angles of  $0^\circ$ ,  $10^\circ$ ,  $20^\circ$ ,  $30^\circ$ ,  $40^\circ$ ,  $50^\circ$ ,  $60^\circ$ ,  $70^\circ$  and  $80^\circ$ . The position of each reflector is carefully chosen so that the normal to the center of the reflector projects through  $x=0$  where the source point is also located. Thus the maximum dip imaged will provide a coarse quantitative measure of the angular aperture of both the forward propagating source wavefield and the backward propagating receiver wavefield (Geiger, pers. comm.). The migration results are shown in Figure 3.15, with the dipping reflectors superimposed on the left half of the figures.

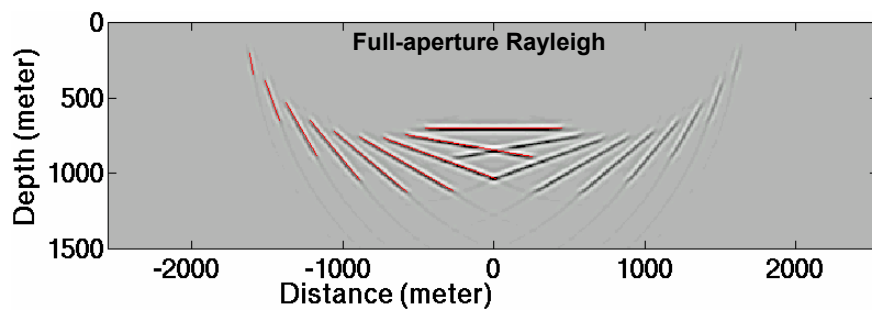


(a)

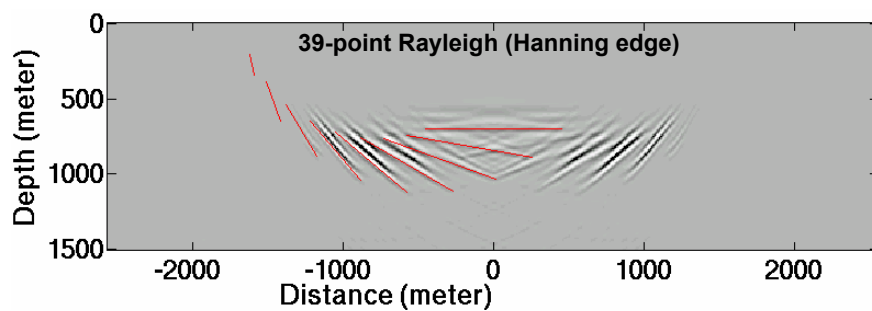


(b)

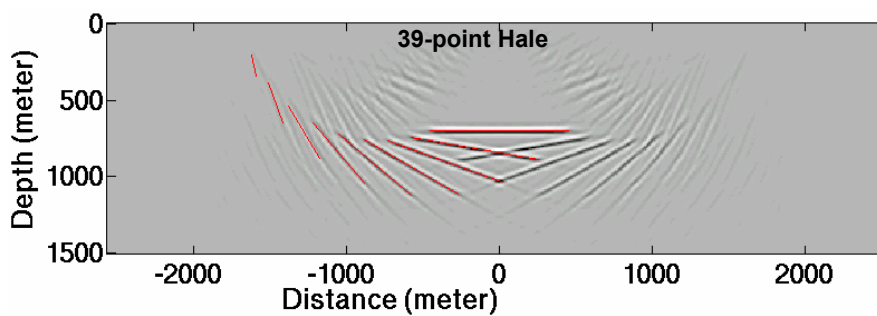
Figure 3.14: (a) A constant velocity earth model containing 17 dipping events. For a better comparison, reflectors are symmetric with  $x=0$ . (b) Synthetic common-source gather of the model with the source located at  $x=0$ .



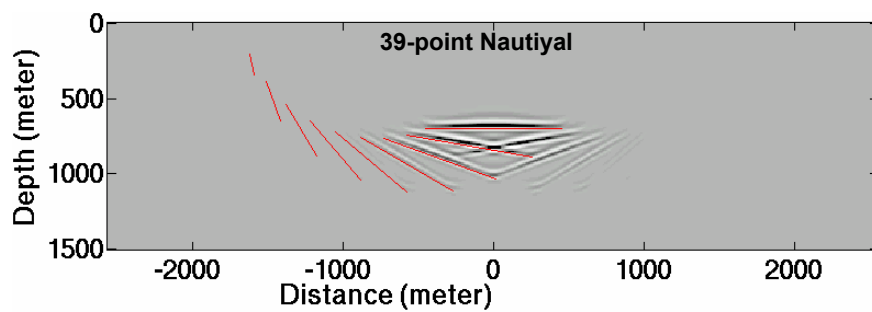
(a)



(b)



(c)



(d)

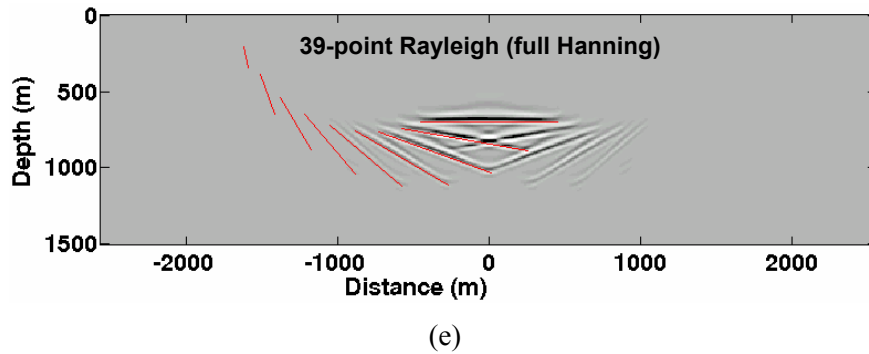


Figure 3.15: Migration of prestack synthetic data by using (a) the full-aperture Rayleigh extrapolator, the 39-point (b) Hanning edge-tapered Rayleigh extrapolator, (c) Hale extrapolator, (d) Nautiyal extrapolator, and (e) full Hanning-tapered Rayleigh extrapolator.

The migration based on the 39-point Hanning edge-tapered Rayleigh extrapolator yields a poor image with most of the reflectors incorrectly positioned (Figure 3.15b). Even the horizontal reflector is poorly positioned due to phase rotation of the wavelet during propagation. It is evident that the  $30^\circ$ ,  $40^\circ$  and  $50^\circ$  reflectors have stronger amplitudes and significant phase errors. As discussed before, this is caused by amplification of waves with phase error – an indication of both instability and inaccuracy. The 39-point Hale extrapolator images reflectors up to a dip angle of  $60^\circ$  (Figure 3.15c). Noise in Figure 3.15c is a consequence of the notched design of the Hale extrapolator discussed previously. Figure 3.15d shows that a prestack depth migration based on the 39-point Nautiyal extrapolator is stable but less accurate. It only imaged the reflectors with a maximum dip angle of  $30^\circ$ . The phase also deviates from the desired full-aperture result (Figure 3.15a). In contrast, the full Hanning-tapered Rayleigh extrapolator imaged the reflectors with the dip angles up to  $40^\circ$  (Figure 3.15e).

All the tests conducted so far assume a homogeneous medium, which is rarely the case in the real world. Thus it is essential to test the extrapolators using a complex model that has structures and velocities similar to the real subsurface.

### 3.6 Marmousi synthetic test

The 2-D acoustic Marmousi dataset was created at the Institut Français du Pétrole (IFP), and is based on a profile through the North Quenguela trough in the Cuanza basin, Angola (Versteeg and Grau, 1991). With the presence of complex reflectors, steep dips and strong velocity gradients, it is widely recognized as an ideal synthetic dataset to test the competence of seismic imaging algorithms.

The Marmousi dataset was generated using a typical 2-D end-on marine survey geometry. The line was shot from west to east with a shot interval of 25 meters and source depth of 8 meters. The first and last shot points are respectively located at 3000 and 8975 meters from the west edge of the model. The streamer (at 12m depth) was composed of 96 hydrophone groups with an offset range from 200 meters to 2575 meters. The distance between two consecutive groups is 25 meters. The velocity model (Figure 3.16) was originally defined with a grid size of 4 meters and contains 160 layers.

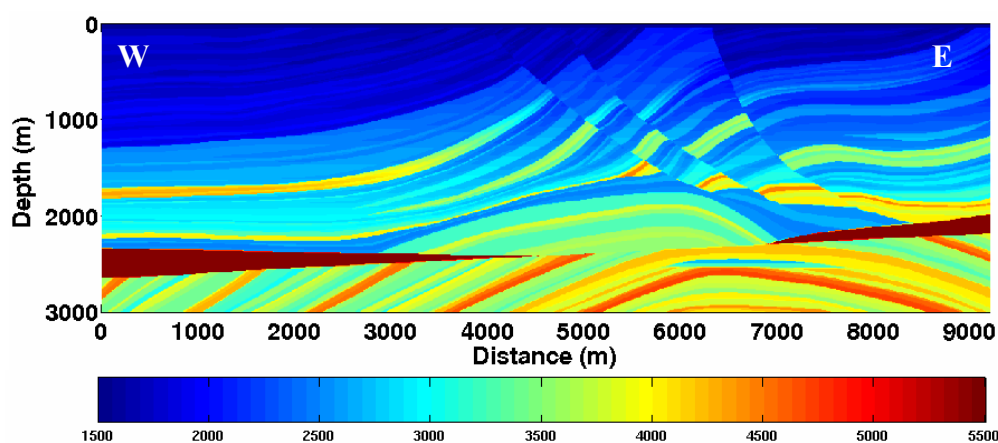


Figure 3.16: Marmousi velocity model. There is also a density model not shown here.

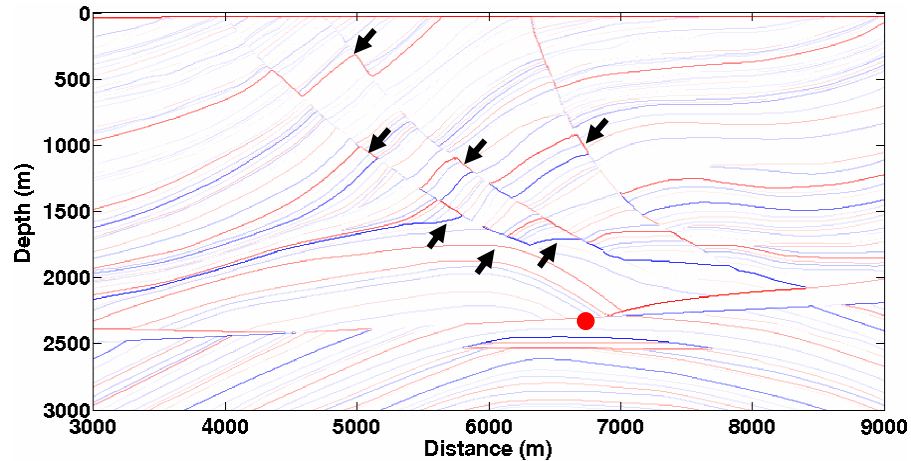


Figure 3.17: Pseudo-reflectivity of Marmousi model. Black arrows indicate the structures that impose challenges to the imaging techniques. The imaging target (reservoir) is denoted by red circle.

Figure 3.17 shows the pseudo-reflectivity computed from the velocity model (Figure 3.16) and the density model (not shown here). The reflectivity is “pseudo” because we assume a normal incident wave when computing reflectivity. The black arrows in Figure 3.17 indicate the major structures that may pose difficulties for the imaging algorithms. The imaging task is to locate the reservoir denoted by the red circle in Figure 3.17.

In order to achieve an optimal image, the Marmousi dataset needs to be carefully preprocessed to obtain a maximum bandwidth zero-phase wavelet with no time delay. Moreover, an accurate source modeling is essential to account for amplitude effects of source arrays, ghosting and near surface multiple effects, and near-surface variable velocity subsurface. The implementation of preprocessing and source modeling is described by Geiger et al.(2003), and will not be discussed in detail here.

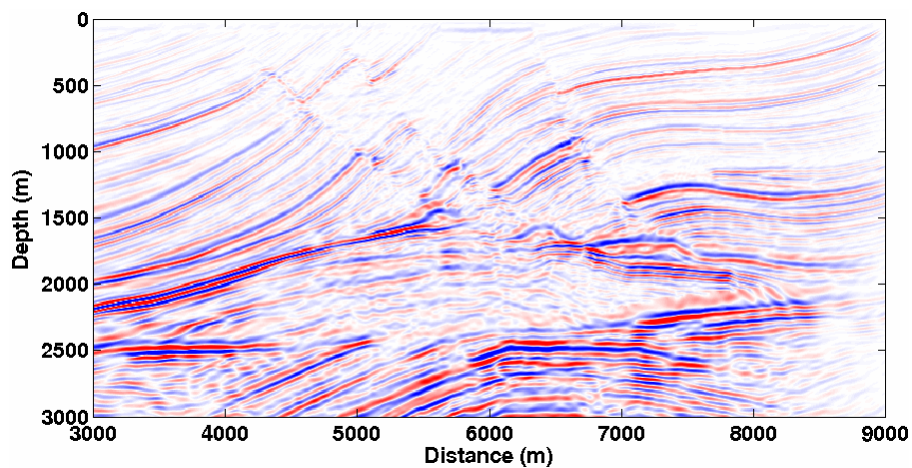
A common-source migration of Marmousi dataset can be computationally expensive, especially with Matlab<sup>®</sup>, which interprets user-defined functions line by line.

A parallel implementation of Matlab<sup>®</sup> on a Linux cluster significantly decreases the elapsed time required to migrate all 240 shots by distributing the common-source gathers to the cluster and migrating a number of gathers concurrently. The final image is then obtained by stacking all the images from each common-source migration. Although the parallel Matlab<sup>®</sup> implementation is not as efficient as parallel C-MPI, it is easy to implement and takes advantage of Matlab's sophisticated functions and visualization capabilities.

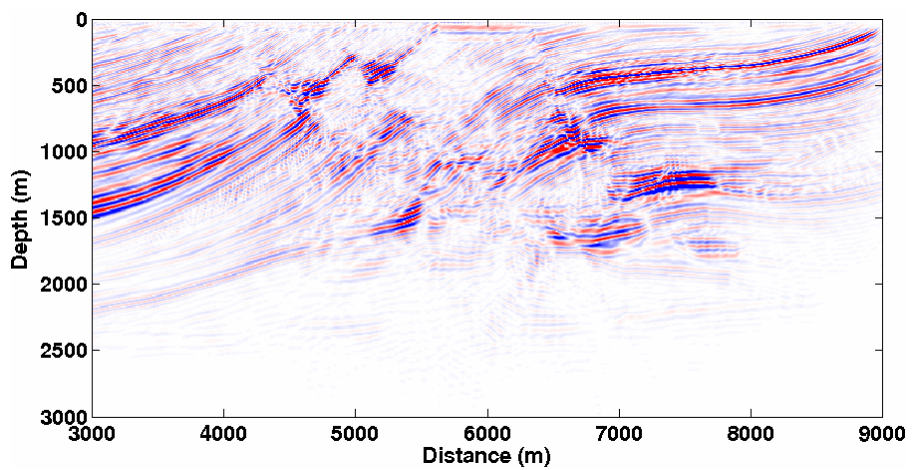
To make the comparison fair, all the tests are based on the same preprocessed data, extrapolation parameters, imaging condition (cross-correlation) and display method. The final migration results are compared in Figure 3.18 (full images), Figure 3.19 (partial images showing the major structures) and Figure 3.20 (partial images showing the imaging target).

Based on the previous analysis, there is no surprise that the 512-point full-aperture Rayleigh extrapolator generates the best overall image (Figure 3.18a). It correctly images the faults, steeply dipping reflectors and reservoir target (Figure 3.20). However, it is computationally too expensive to be practical. The 39-point Hale extrapolator generates a comparable image (Figure 3.18c) with much less cost. The artifacts due to the notched design of the Hale extrapolator are not as evident as seen in the single-shot prestack test (Figure 3.15c). The possible explanations are (1) some of the artifacts will not accumulate in the inhomogeneous medium; (2) the final stack suppresses some of the artifacts. The close-up display (Figure 3.19d) indicates that the image from the Hale extrapolator is slightly phase-rotated. This can be attributed to the phase error of the Hale extrapolator discussed in the previous section. The Hale

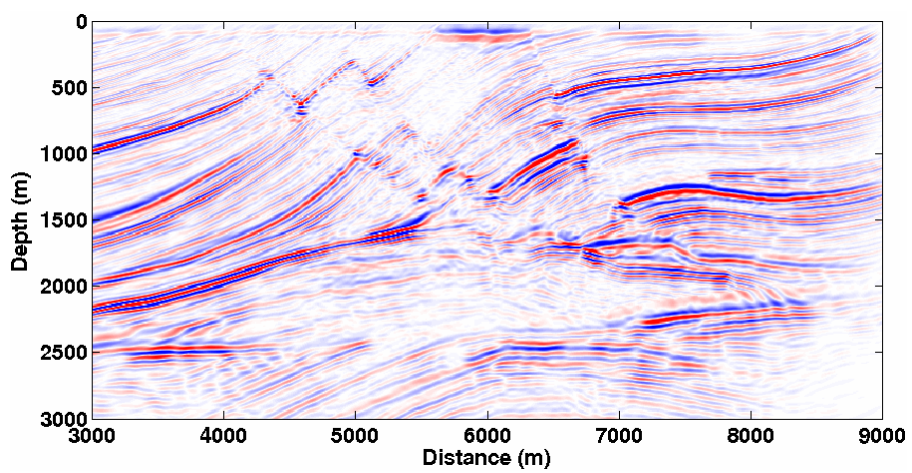
extrapolator successfully images the target reservoir (Figure 3.20).



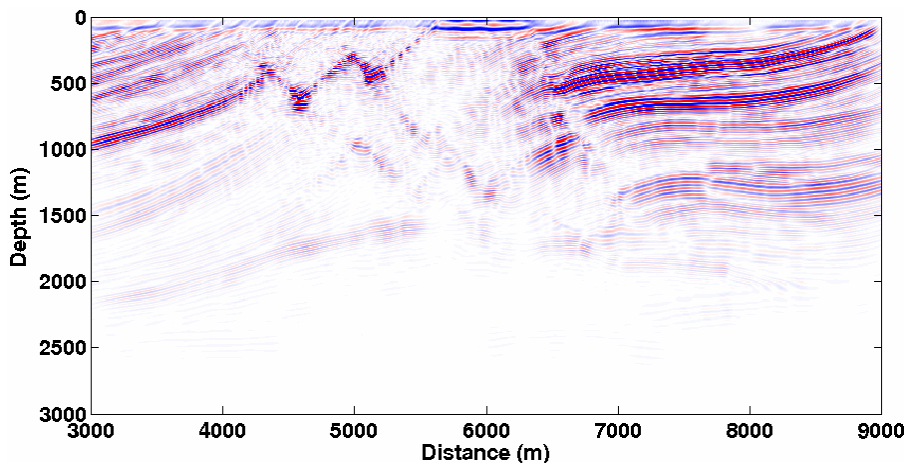
(a)



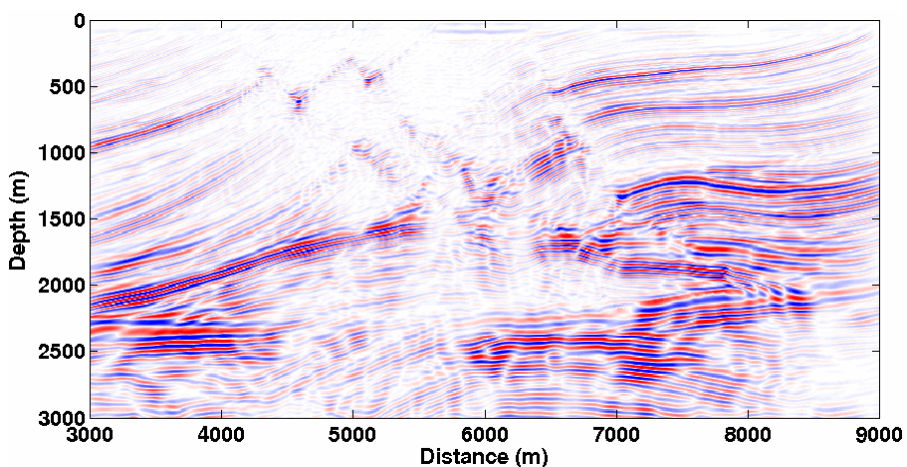
(b)



(c)



(d)



(e)

Figure 3.18: Common-source migration of Marmousi dataset using (a) the full aperture (512-point) Rayleigh extrapolator, the 39-point (b) Hanning edge-tapered Rayleigh extrapolator, (c) Hale extrapolator, (d) Nautiyal extrapolator and (e) full Hanning-tapered Rayleigh extrapolator. All the figures are displayed using identical scaling values.

The Hanning edge-tapered Rayleigh extrapolator, the Nautiyal extrapolator and the full Hanning-tapered Rayleigh extrapolator (Figure 3.18b, Figure 3.18d and Figure 3.18e) generate poor images. All of them fail to image the target reservoir correctly. As shown by the error contours of the Hanning edge-tapered Rayleigh extrapolator, the instability and inaccuracy rapidly accumulate during downward continuation, resulting in a distorted image. Even the gentle dipping reflectors in the deeper section are not

properly imaged (Figure 3.18b and Figure 3.19c). The Nautiyal extrapolator fails to image steeply dipping reflectors (Figure 3.18d and Figure 3.19e). This is caused by severe attenuation of the wavefield propagating at high angles, a result of the Gaussian window applied to ensure stability. However, compared to the Hanning edge-tapered Rayleigh extrapolator, the Nautiyal extrapolator yields better phase accuracy in the deeper part of the image. The full Hanning-tapered Rayleigh extrapolator generates the “best” image among the three spatially-tapered extrapolators (Figure 3.18e and Figure 3.19f). Although it is more stable and accurate than the others, instability and inaccuracy are still evident in the deeper part of the section.

The observations from the Marmousi test are consistent with those from the single-shot prestack test, except that the Hale extrapolator generates a better image in the multi-shot Marmousi test because the artifacts due to the notched design are suppressed. This suggests that the single-shot constant-velocity prestack test is a quick and effective tool for evaluating an extrapolator before they are applied to the complex models.

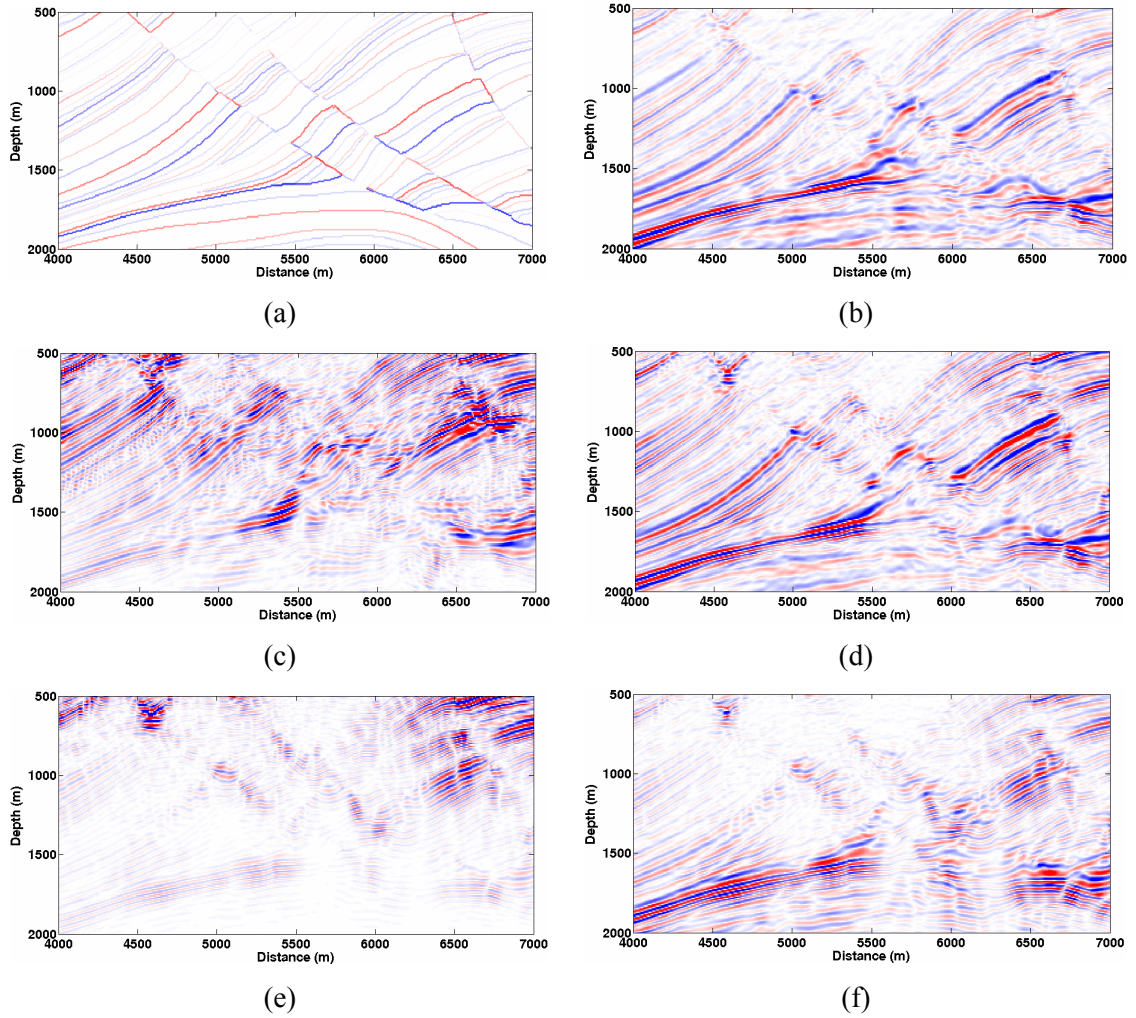


Figure 3.19: Comparison of the major faults of images in Figure 3.18. (a) Pseudo-reflectivity; (b) images from the full-aperture Rayleigh extrapolator; images from the 39-point (c) Hanning edge-tapered Rayleigh extrapolator, (d) Hale extrapolator, (e) Nautiyal extrapolator and (f) full Hanning-tapered Rayleigh extrapolator.

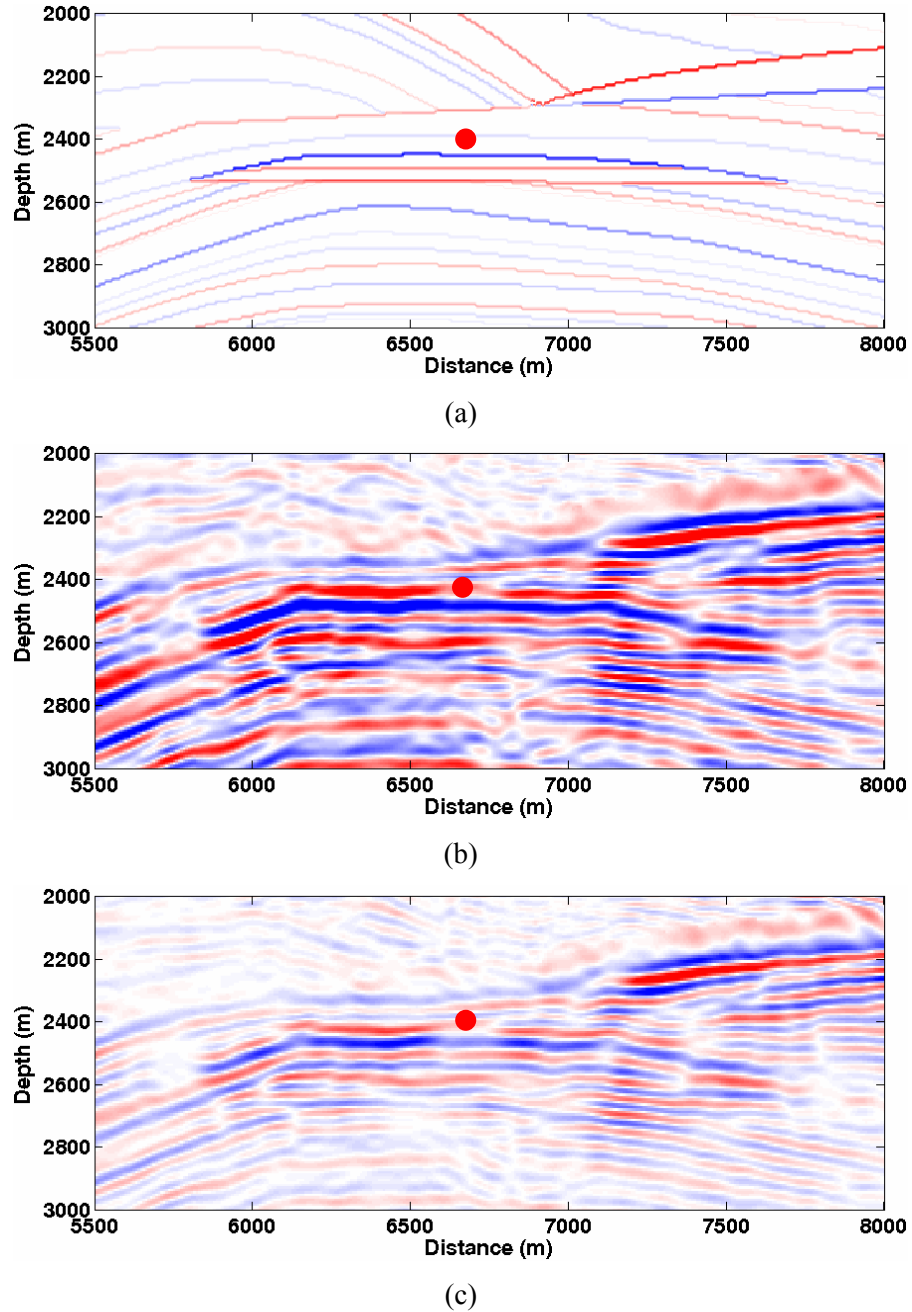


Figure 3.20: The comparison of image target (reservoir). (a) Pseudo-reflectivity; image from (b) the full-aperture Rayleigh extrapolator and (c) the 39-point Hale extrapolator.

### 3.7 Computation costs

The computation costs of various extrapolators in a constant velocity zero-offset impulse response test are shown in Figure 3.21. The coefficients of the three

extrapolators are computed in Matlab<sup>®</sup> (the Rayleigh and Nautiyal extrapolator) and Maple<sup>®</sup> (the Hale extrapolator), and then implemented in Matlab<sup>®</sup> using a table-lookup scheme for the wavefield extrapolation. The test is conducted with a dataset containing 200 traces (512 time samples/trace) and run on a Linux system (3GHz CPU and 2GB RAM) with 200 extrapolation steps.

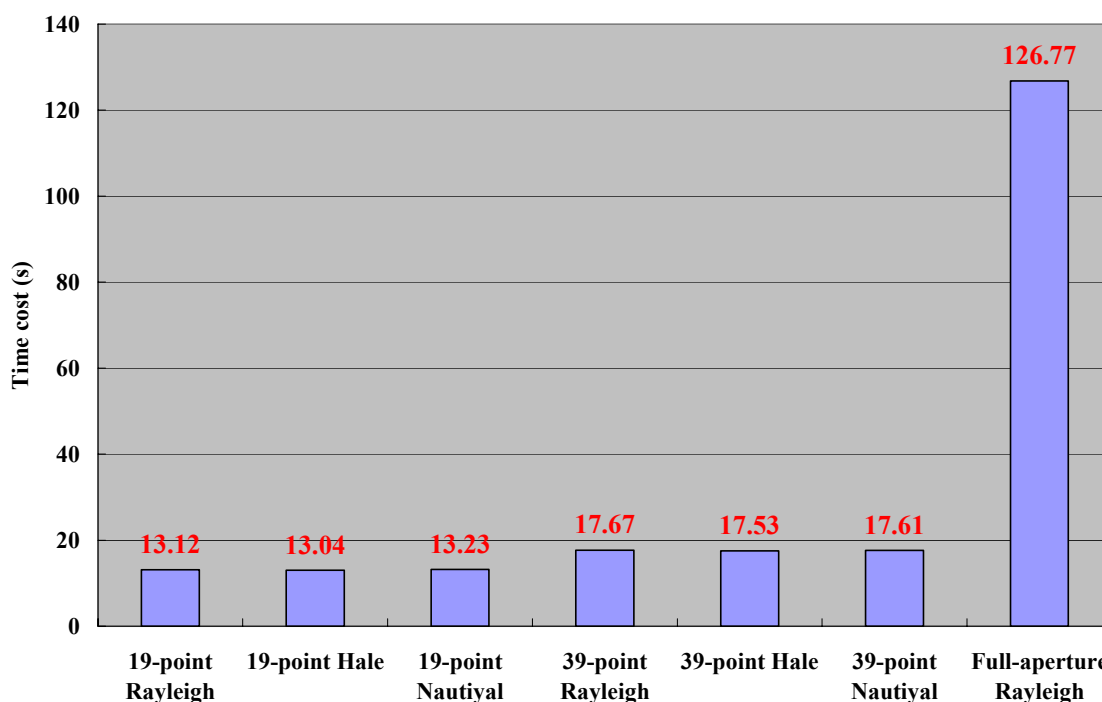


Figure 3.21: Computation costs of the three extrapolators.

The computational cost of implementing the various wavefield extrapolators (not including cost of computing coefficients for table-lookup) is shown in Figure 3.21. A general observation is that longer extrapolators are more expensive. The full-aperture (200-point) Rayleigh extrapolator is the most expensive, suggesting that it is less practical for commercial applications. Given the same extrapolator length, the time costs for the three extrapolators are very similar. This is because all three limited-aperture

extrapolators are calculated in advance and implemented in the  $x$ - $\omega$  domain as convolutional filters.

It is not practical to compare the computational costs of creating the table for the three extrapolators because the Hale extrapolator is computed in Maple<sup>®</sup> and the other two are computed in Matlab<sup>®</sup>.

### 3.8 Chapter summary

Stability and accuracy are two important aspects of the wavefield extrapolators. A stable extrapolator may not be accurate (e.g., the Nautiyal extrapolator), while an accurate extrapolator is not guaranteed to be stable (e.g., full-aperture Rayleigh extrapolator). The behavior of the extrapolators can only be fully understood by careful stability and accuracy analysis. In this chapter, a common set of tools are used to conduct the comprehensive stability and accuracy analysis of the three extrapolators. The tools and their purposes are listed in Table 1.

<b>Tool</b>	<b>Purpose</b>
3-D plot of the extrapolators in the $k_x$ - $\omega$ domain	Help understand the extrapolators intuitively
3-D error plots in the $k_x$ - $\omega$ domain	Evaluate the extrapolators qualitatively
Amplitude analysis in the $k_x$ - $\omega$ domain	Stability analysis
Amplitude and phase error contours	Quantitative stability and accuracy analysis
Zero-offset impulse response test (constant velocity)	Evaluate the stability and accuracy of extrapolators in poststack migrations
Prestack dip accuracy test (constant velocity)	Evaluate the stability and accuracy of extrapolators in prestack migrations
Common-source migration of the Marmousi dataset (variable velocity)	Evaluate the capability of extrapolators with complex structures

Table 1: Tools of stability and accuracy analysis in this thesis and their purposes.

A comparison of the three extrapolators indicates that the Hale extrapolator is the best. Although the full-aperture Rayleigh extrapolator can produce comparable images, it is too expensive to be practical. The limited-aperture and spatially-tapered (either by Hanning or Gaussian window) Rayleigh extrapolator is not able to generate acceptable images of either the simple prestack model or the complex Marmousi model. A qualitative comparison is shown in Table 2.

	$x$ - $\omega$ extrapolators	Stability	Accuracy	Efficiency
Aperture limited	Hale extrapolator	★ ★ ★	★ ★ ★	★ ★ ★
	Nautiyal extrapolator	★ ★ ★	★	
	Rayleigh extrapolator (Hanning edge taper)	NO	NO	
	Rayleigh extrapolator (full Hanning taper)	★ ★	★ ★	
Full aperture	Full aperture Rayleigh	★ ★ ★	★ ★ ★	★

Table 2: Comparison of stability, accuracy and efficiency of various extrapolators. More stars is better.

## **Chapter Four: ADAPTIVE TAPERING IN WAVEFIELD EXTRAPOLATION**

Seismic reflection field data are always discontinuous at the bounds of the recorded survey, and, as described previously, any practical implementation of a wavefield extrapolator has finite length and is therefore discontinuous at the bounds of the operator. A proper handling of the discontinuities during seismic imaging is required to obtain an optimum image (Claerbout, 1985).

In recursive wavefield extrapolation, artifacts caused by discontinuities may interfere destructively and therefore become negligible after a number of depth steps. However, these artifacts could still be significant in the shallow image and may interfere with some processing or imaging operations (e.g., creating near surface velocity models). A reasonable procedure for dealing with discontinuities is particularly important for the first extrapolation step, where the field data are typically padded with zero traces out to the desired size of the migration aperture. Note that there are two discontinuities in the first extrapolation step (Figure 4.1):

1. A discontinuity between the acquired data and zero traces (survey truncation).
2. A discontinuity as a result of the truncation of extrapolation aperture (extrapolator truncation).

The standard method for handling a finite survey aperture is to apply tapers to the data edges prior to extrapolation (Sheriff, 2002, p. 347-348). However, it is not clear if this static tapering is necessary, as it may introduce additional inaccuracies (Claerbout, 1985). The typical remedy for extrapolator truncation is to apply a taper to the

extrapolator. Although the spatial-tapered extrapolator is not stable (as discussed in Section 3.2), it could be useful for the first few steps where the instability can be neglected.

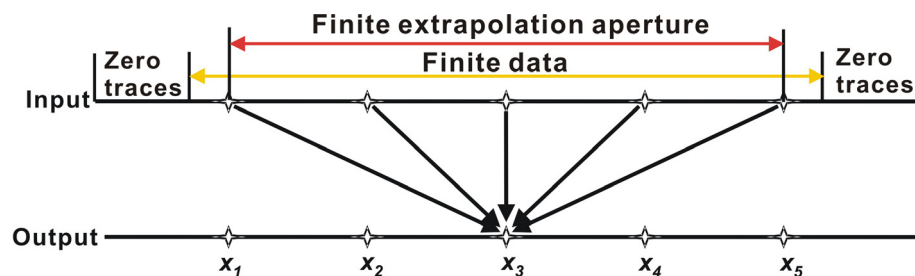


Figure 4.1: The discontinuities in the first extrapolation step.

A simple 2-D synthetic test can be used to show the truncation artifacts created by the first extrapolation step. Figure 4.2a illustrates a synthetic input section that consists of three dipping events, with  $dx=18m$ , and  $dt=4ms$ . For this test, a constant velocity of 2000m/s is assumed for convenience, but the general results are also applicable to variable velocity. Before extrapolation the data are padded with null traces at the edges so that events can be extrapolated beyond the original extent of the survey. The angular aperture of the extrapolator is limited to 70 degrees, which is equivalent to setting a maximum scattering angle ( $\theta = \cos^{-1}(z/r)$ ) of 70 degrees. The input wavefield is then upward extrapolated with a single depth step of 200m. Figure 4.2b shows the output wavefield with no survey or extrapolator tapers. The two truncation artifacts are readily apparent in Figure 4.2b: artifacts labelled “1” and “2” are from the survey and extrapolator truncation, respectively. The conventional approach to reducing artifacts is to apply tapers to both the data and the extrapolator.

Figure 4.3 shows that most of the artifacts are removed. However, this kind of

static survey tapering may cause unnecessary accuracy losses, as the data are then double-tapered (by both survey and extrapolator tapers) when the extrapolation operator reaches the edge of the data (Figure 4.4). This observation motivates the design of an adaptive tapering scheme that can dynamically handle the data and extrapolator truncations with minimal loss of accuracy.

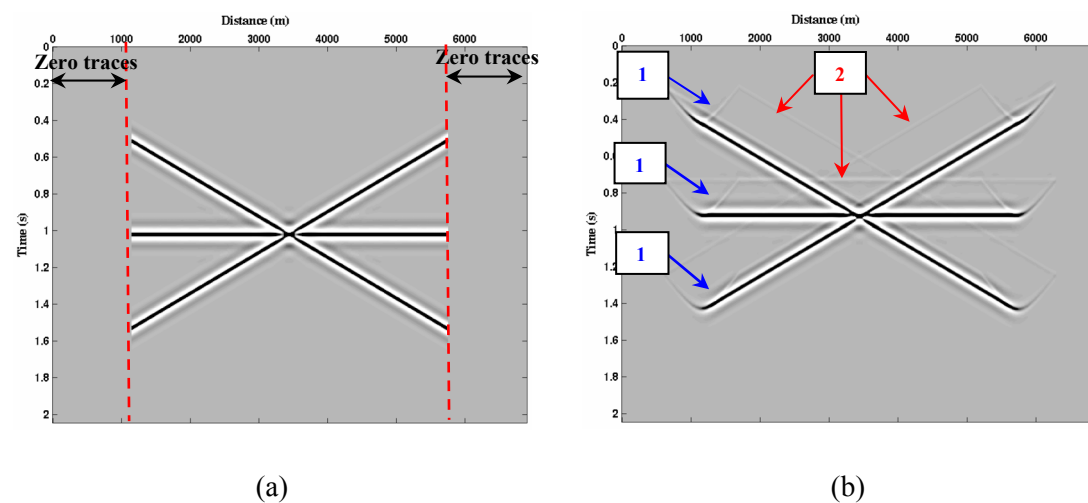


Figure 4.2: (a) Synthetic section padded with zero traces on each side. (b) The wavefield in Figure 4.2a is upward extrapolated using a Rayleigh extrapolator. Without any treatment of the truncations, artifacts occur on the output section.

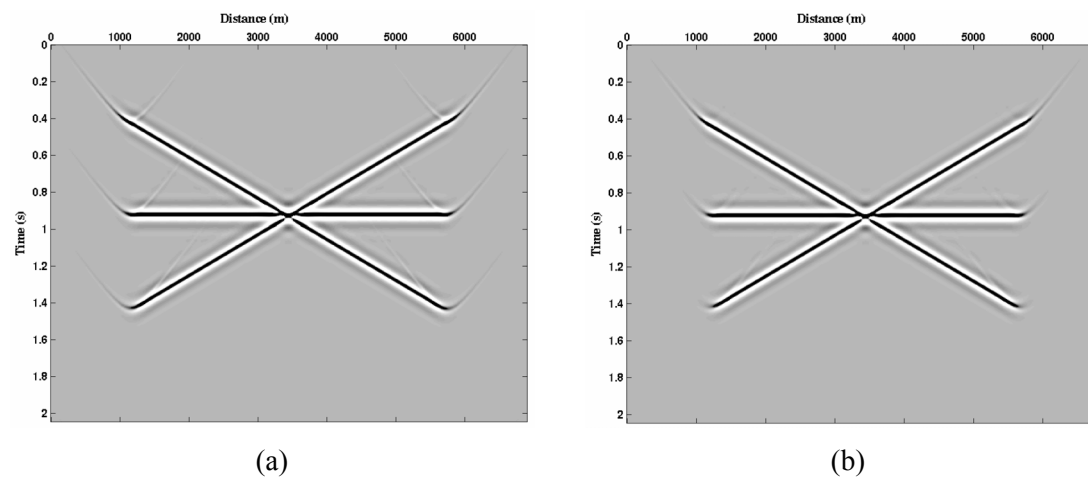


Figure 4.3: The effects of conventional tapering. (a) After a Hanning taper to the extrapolator, artifacts 2 have been removed. (b) After applying Hanning tapers to both data and extrapolator, most of the artifacts are removed.

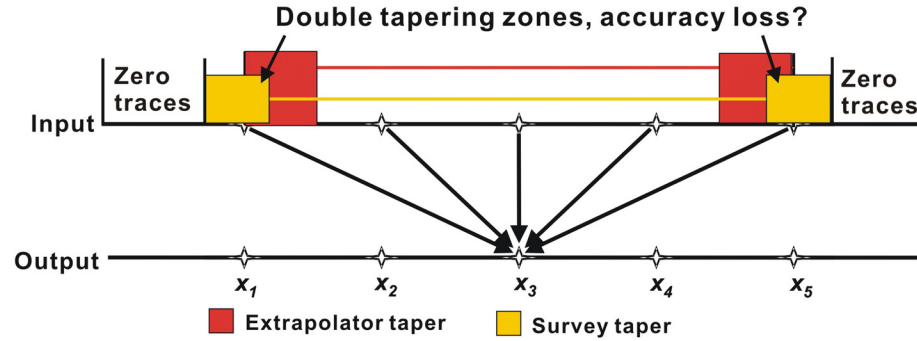


Figure 4.4: Conventional tapering may cause accuracy loss.

#### 4.1 Adaptive tapering for the first extrapolation step

Figure 4.5 illustrates how the extrapolation operator incorporates an adaptive taper that varies with output location. The percent ratio of the taper angle to the maximum scattering angle is the key parameter that controls both the survey and extrapolator taper. To implement the adaptive taper, the output locations are divided into three zones: the left padding zone, the data zone, and the right padding zone, corresponding to MH, HI and IN in Figure 4.5.

When the output point  $O_1$  lies in the left padding zone (MH), the taper scheme is shown in Figure 4.5b. The angle  $BO_1C$  and  $DO_1E$  are responsible for taper control and chosen such that they have the same percentage of angle  $KO_1B$  and  $\theta$ . Once the taper zones (BC and DE) are determined, the tapers can be immediately calculated and applied to the input wavefield. A minimum taper width is specified in case the angle  $BO_1C$  is too small to taper the data edge effectively; When the output point  $O_2$  lies in the data zone (HI in Figure 4.5c), the angle  $B'O_2C$  and  $DO_2E$  are chosen to be the same percentage of angle  $\theta$ . Thus, taper zones  $B'C$  and DE can be identified similar to when the output point  $O_3$  lies in the right padding zone (IN in Figure 4.5d), except that the sign of the angle is

negative.

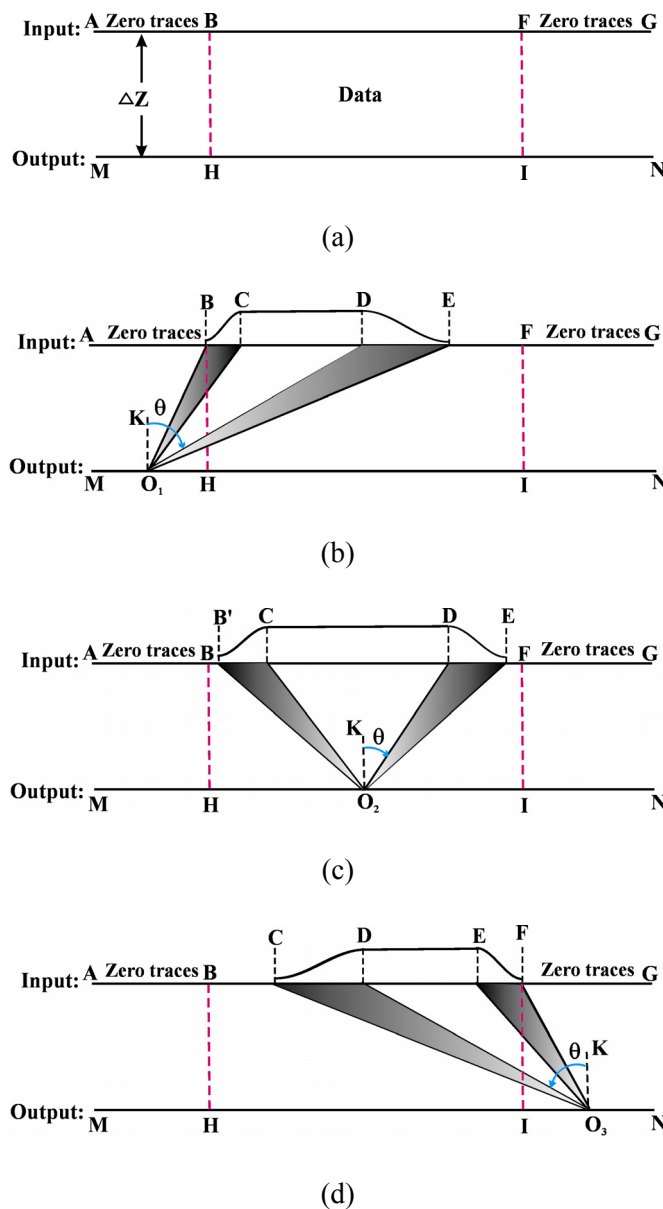


Figure 4.5: The adaptive tapering schemes that are dependent on the output point locations.

## 4.2 Synthetic tests

Figure 4.6a and Figure 4.6b provide a comparison between the extrapolation using conventional survey taper plus extrapolator taper scheme and the extrapolation using the adaptive taper. To make them comparable, a data taper width of 10 samples is

used in Figure 4.6a, which is equal to the minimum adaptive taper width in Figure 4.6b. The taper function used is the half Hanning window (equation (2.20)). Both the extrapolators in Figure 4.6a and Figure 4.6b have the same angular aperture. The wavefield in Figure 4.6a is obtained by first tapering the synthetic section (Figure 4.2a) at the data edges, and applying an extrapolator taper. Although some artifacts are attenuated as compared to Figure 4.2b, the survey truncation artifacts are still observable, and are strongest from the dipping events. The artifacts can be reduced by increasing the length of the survey taper, but the cost is a loss of accuracy in the extrapolated wavefield. In comparison, extrapolation using the adaptive taper (Figure 4.6b) better attenuates the artifacts with less loss of accuracy in the extrapolated wavefield.

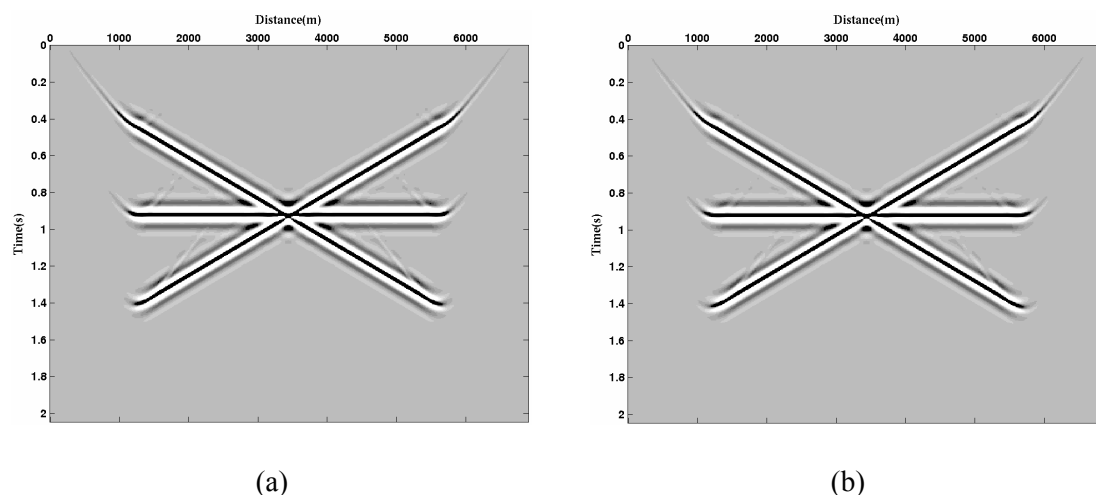
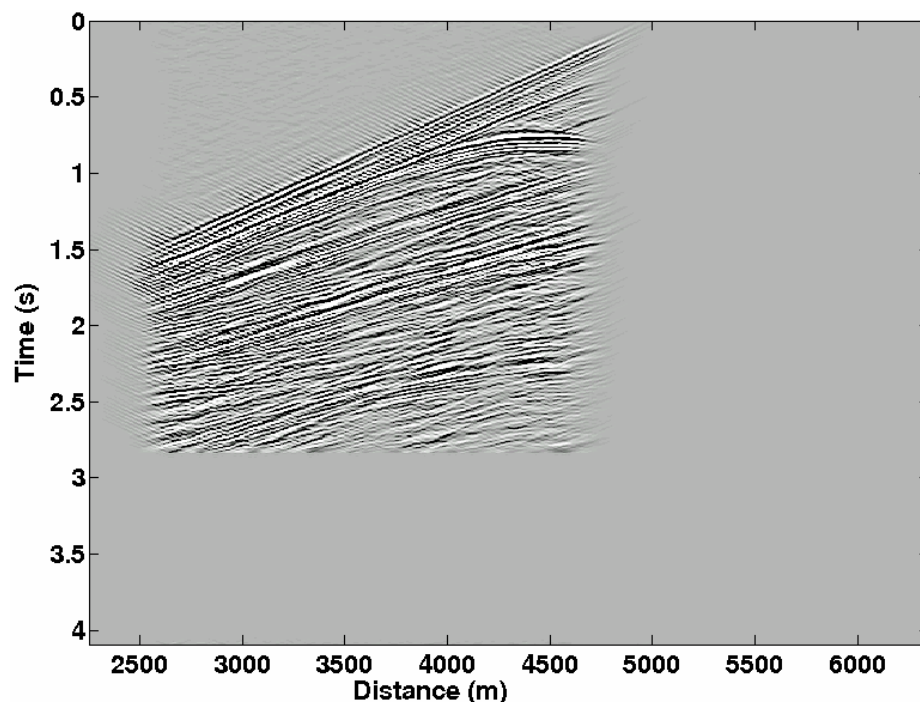


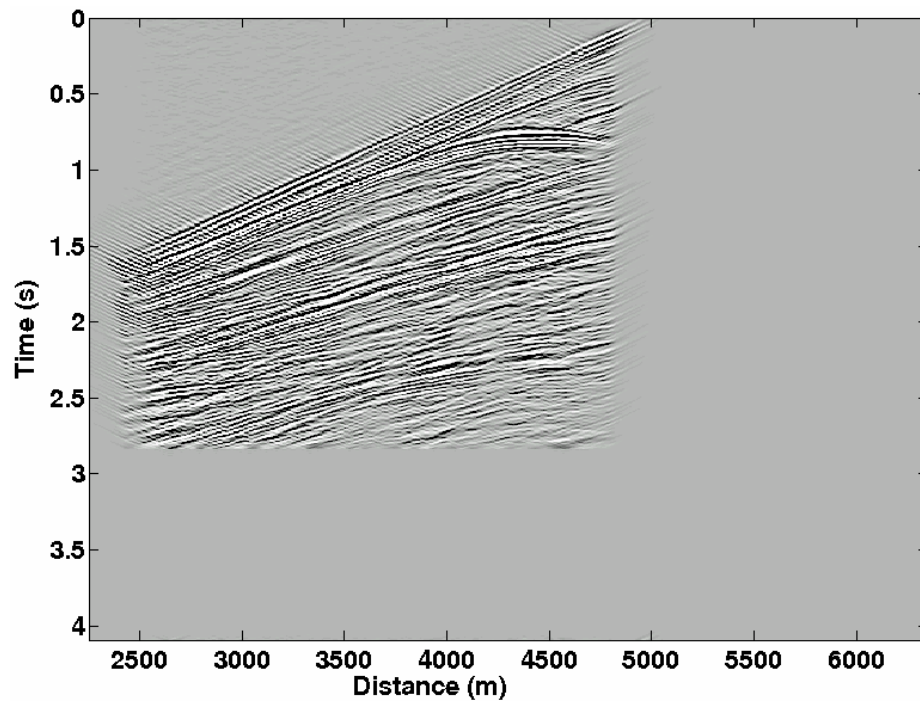
Figure 4.6: (a) Conventional extrapolation with separate data and extrapolator tapers; (b) Extrapolation with the adaptive taper. In order to make a better comparison, figures are displayed with a less clip value (therefore stronger amplitudes) than the one used in Figure 4.3.

Figure 4.7a and Figure 4.7b show the wavefields (in the  $x-t$  domain) generated by the first extrapolation step of a common-source gather of Marmousi dataset. The survey taper width and the minimum adaptive tapering width are both chosen as 15 traces. It is evident that the conventional tapering scheme double-tapers the data edge (Figure 4.7a)

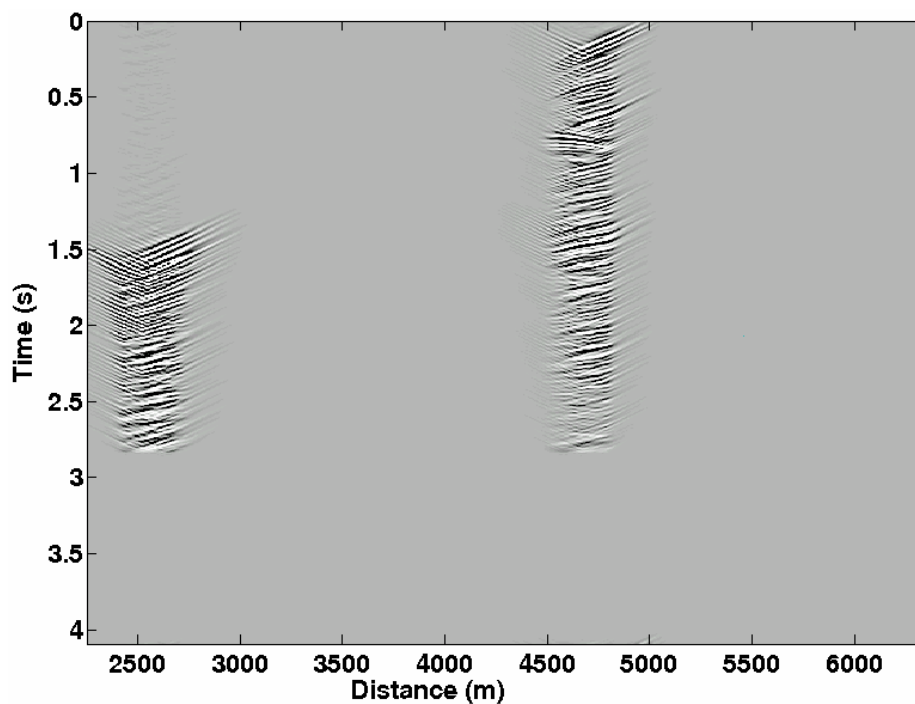
and will cause accuracy loss (see Figure 4.7c).



(a)



(b)



(c)

Figure 4.7: The results from first (backward) extrapolation step of a Marmousi common-source gather (shot point at 5000m) with (a) conventional tapering and (b) adaptive tapering. Difference ((b) minus (a)) is plotted in (c). The common-source gather is padded with zero traces on both sides and zeros in the bottom (for fast Fourier transform).

Images from the common-source migration of Marmousi dataset are shown in Figure 4.8. The images are generated by applying conventional tapering (Figure 4.8a) and adaptive tapering (Figure 4.8b) to the Rayleigh extrapolator for the first extrapolation step and then switching to the Hale extrapolator for the remaining steps to ensure stability. The image from adaptive tapering (Figure 4.8b) has a better illumination of the shallow structures than the one from the conventional tapering (Figure 4.8c). Improved illumination and better event continuity could help with correlation of near surface reflectors with surface geology, which would be an important interpretation benefit when imaging seismic datasets from complicated structural areas such as the Canadian Foothills. However, it is difficult to determine whether the image created using the

adaptive tapering scheme has comparable artifact suppression as seen in the synthetic test (Figure 4.6). The final stack used in the common-source migration may cancel some random artifacts and minimize the difference.

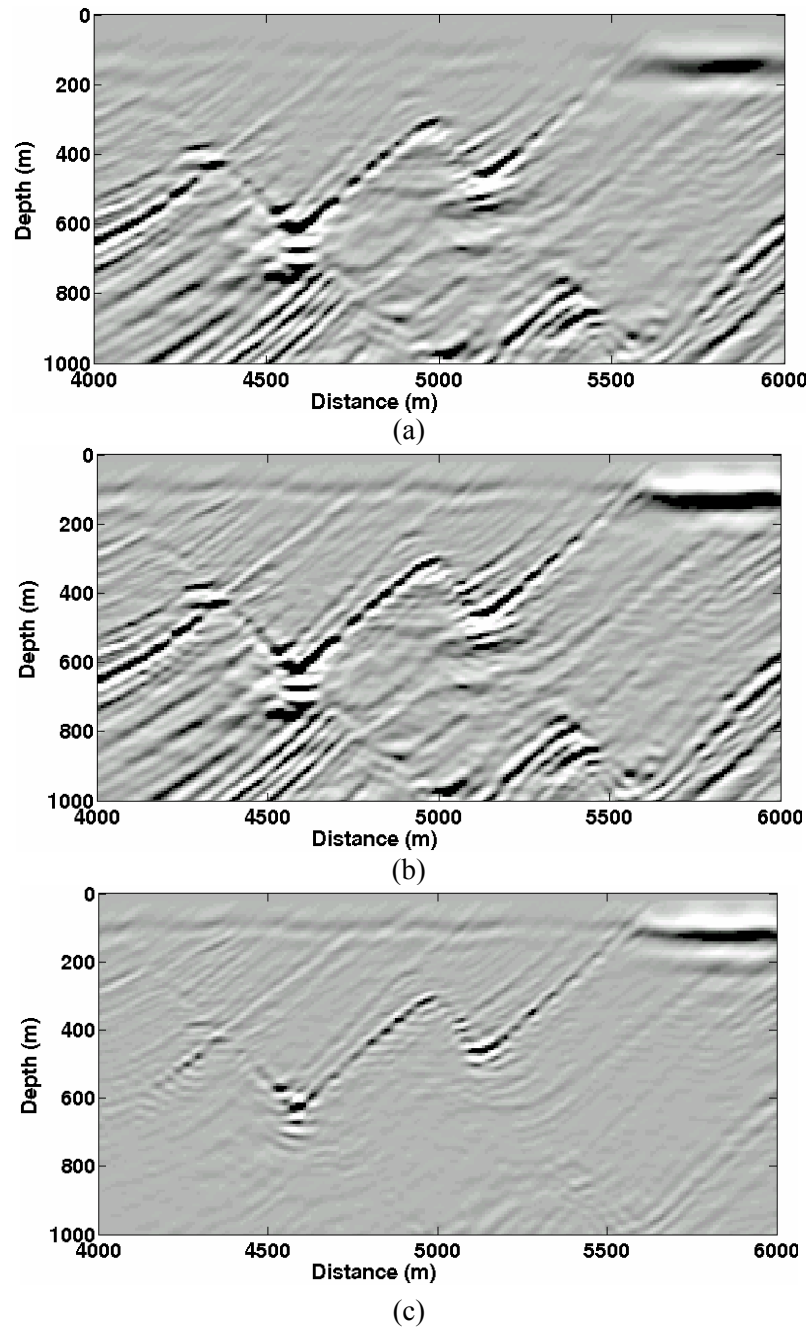


Figure 4.8: Shallow images of Marmousi dataset generated by (a) conventional tapering and (b) adaptive tapering. Difference ((b) minus (a)) is plotted in (c). All the figures are displayed using identical scaling values.

### **4.3 Chapter summary**

A new adaptive tapering scheme is proposed. Simple and complex synthetic tests indicate that adaptive tapering can be applied in the first extrapolation step to produce a better shallow image than the conventional tapering scheme.

## Chapter Five: CONCLUSIONS AND FUTURE WORK

Both stability and accuracy are important considerations for the design of  $x$ - $\omega$  domain wavefield extrapolators used in wavefield-continuation migration. Instabilities may arise when the recursive extrapolator is spatially truncated and its amplitude oscillates about unity. Inaccuracies may also occur when the amplitude and phase of the designed extrapolator deviate from those of the desired ideal extrapolator. Many extrapolators have been developed with various stability and accuracy features. To fully understand the behaviour of extrapolators and better evaluate their performance, a comprehensive stability and accuracy analysis is required. In this thesis, I compared the stability and accuracy of a Rayleigh extrapolator, Hale extrapolator, and Nautiyal extrapolator.

The implementation of the three extrapolators in Matlab<sup>®</sup> was designed to ensure that the analysis and comparison was fair. The parallel Matlab<sup>®</sup> implementation has provided a way to facilitate the coding and debugging process as well as to achieve better efficiency compared to the traditional serial Matlab<sup>®</sup> implementation.

A common set of tools that are either intuitive or quantitative has been used for stability and accuracy analysis, including 3-D error plots, error contours, zero-offset impulse response test, prestack dip accuracy, and complex imaging using the Marmousi synthetic dataset. All the tools were designed to supplement each other, and were utilized to illustrate the capabilities of the three extrapolators in both a homogeneous medium and strong heterogeneous environments.

The amplitude and phase error contours in the  $\omega$ - $\theta$  (frequency-angle) domain clearly describe the behaviours of the extrapolators. These observations are in turn confirmed by the poststack zero-offset impulse test and the prestack dipping-event tests. The error contour analysis provides detailed quantitative information about the performance of an extrapolator compared to the desired exact response. A key observation is that a limited-aperture extrapolator should be designed to preserve as much of the propagating wavefield as possibly, but must attenuate propagating waves where there is significant phase error.

The constant velocity dipping-event prestack test has proved to be a very useful tool for testing wavefield extrapolators. The observations from the constant velocity prestack test are consistent with those from the Marmousi test, where strong heterogeneity is present. Therefore, this test is an effective tool for evaluating the performance of extrapolators in a prestack depth migration before they are applied to a complex model.

In general, the tools used in this thesis proved to be effective and therefore can be used for the further testing of newly developed extrapolators.

The stability and accuracy analysis shows that the Hale extrapolator, widely considered to be an industrial standard, is stable and accurate. Although the limitations on propagation angle and the artifacts caused by its inherently blocky design make it less than perfect, the Hale extrapolator still produces a superior image compared to the other two extrapolators. The full-aperture Rayleigh extrapolator is accurate, but it is computationally expensive and not guaranteed to be stable for a large-number of

extrapolation steps. The limited-aperture Hanning edge-tapered Rayleigh extrapolator turned out to be neither stable nor accurate. The amplification of the propagating waves, combined with phase errors, turns out to be the main cause of its instability and inaccuracy. The full Hanning-tapered Rayleigh extrapolator is more stable and accurate than the Hanning edge-tapered one, but it can not produce an acceptable image in the complex model test. The Nautiyal extrapolator represents another straightforward way to stabilize the Rayleigh extrapolator in the space domain, and is easy to implement. Unfortunately, its stability compromises its accuracy.

Some important observations are documented in this thesis, including the derivation error of the Hale extrapolator, the artifacts associated with the Hale extrapolator, and the poor accuracy of the Nautiyal extrapolator.

A new adaptive tapering scheme is proposed in this thesis and is compared with the conventional tapering method using both simple and complex models. The results show that adaptive tapering can be applied during the first extrapolation step to improve the image from a common-source migration at shallow depth.

Although the spatially-tapered Rayleigh extrapolator produces the poorest image, it could be still useful for regularizing land data with irregular geometry and/or in areas of rough topography. The Rayleigh extrapolator could be applied for the first few steps (where the effects of instability and inaccuracy do not accumulate sufficiently to be of concern) followed by an alternate stable and accurate extrapolator (such as the Hale extrapolator) for later depth steps. In addition, the adaptive tapering scheme can be further improved and combined with the Rayleigh extrapolator to enhance the imaging of

land data with irregular acquisition geometry and rough topography. These would be interesting topics for the future research.

**REFERENCES**

- Berkhout, A. J., 1981, Wave field extrapolation techniques in seismic migration, a tutorial: *Geophysics*, **46**, 1638-1656.
- , 1982, *Seismic migration: imaging of acoustic energy by wave field extrapolation*: Elsevier.
- Bevc, D., 1997, Imaging complex structures with semirecursive Kirchhoff migration: *Geophysics*, **62**, 577-588.
- Bevc, D. and Biondi, B., 2002, Which depth imaging method should we use? A road map in the maze of 3-D depth imaging: 72nd Ann. Internat. Mtg., Soc. of Expl. Geophys., Expanded Abstracts, 1236-1239.
- Biondi, B., 2003, *3-D seismic imaging: Course notes*, Stanford Univ.
- Blacquiere, G., debye, H. W. J., Wapenaar, C. P. A. and Berkhout, A. J., 1989, 3D table-driven migration: *Geophysical Prospecting*, **37**, 925-958.
- Claerbout, J. F., 1971, Toward a unified theory of reflector mapping: *Geophysics*, **36**, 467-481.
- , 1985, *Imaging the earth's interior*: Blackwell Scientific Publications.
- Etgen, J. T., 1994, Stability of explicit depth extrapolation through laterally-varying media: 64th Ann. Internat. Mtg., Soc. of Expl. Geophys., Expanded Abstracts, 1266-1269.
- Ferguson, R. J. and Margrave, G. F., 2002, Prestack depth imaging by symmetric nonstationary phase shift: *Geophysics*, **67**, 594-603.
- Gazdag, J., 1978, Wave equation migration with the phase shift method: *Geophysics*, **43**, 1342-1351.

- Gazdag, J. and Sguazero, P., 1984, Migration of seismic data by phase shift plus interpolation: *Geophysics*, **49**, 124-131.
- Geiger, H. D., Margrave, G. F., Foltinek, D. S. and Langlois, J. M., 2002, Parallel 3D prestack depth migration using recursive Kirchhoff extrapolation: CREWES Research Report, **14**, 1-20.
- Geiger, H. D., Margrave, G. F., Liu, K. and Daley, P. F., 2003, Depth imaging using slowness-averaged Kirchhoff extrapolators: CREWES Research Report, **15**, 1-14.
- Godfrey, R. J., Muir, F. and Claerbout, J. F., 1979, Stable extrapolation: SEP-16, 83-87.
- Hale, D., 1991, Stable explicit depth extrapolation of seismic wavefields: *Geophysics*, **56**, 1770-1777.
- Holberg, O., 1988, Towards optimum one-way wave propagation: *Geophysical Prospecting*, **36**, 99-114.
- Kelly, S. and Ren, J., 2003, Key elements in the recovery of relative amplitudes for prestack, shot record migration: 73rd Ann. Internat. Mtg.: Soc. of Expl. Geophys., 1110-1113.
- Maeland, E., 1994, On the evaluation of explicit 2-D extrapolation operators: *Geophys. J. Int.*, **116**, 85-94.
- Margrave, G. F. and Daley, P. F., 2001, Recursive Kirchhoff extrapolators: CREWES Research Report, **13**, 617-646.
- Margrave, G. F. and Ferguson, R. J., 1999, Wavefield extrapolation by nonstationary phase shift: *Geophysics*, **64**, 1067-1078.
- Margrave, G. F. and Geiger, H. D., 2002, Wavefield resampling during Kirchhoff extrapolation: CREWES Research Report, **14**, 1-17.

- Mittet, R., 2002, Explicit 3D depth migration with a constrained operator: 72nd Ann. Internat. Mtg, Soc. of Expl. Geophys., Expanded Abstracts, 1148-1151.
- Nautiyal, A., 1990, Limitations in recursive wavefield continuation with spatial wavelets: Inst. Electr. Electron. Eng., Trans. Geosci. Remote Sensing, GE-28, 272-274.
- Nautiyal, A., Gray, S. H., Whitmore, N. D. and Garing, J. D., 1993, Stability versus accuracy for an explicit wavefield extrapolation operator: Geophysics, **58**, 277-283.
- Notfors, C. D. B., 1995, Accurate and efficient explicit 3-D migration: 65th Ann. Internat. Mtg, Soc. of Expl. Geophys., Expanded Abstracts, 1224-1227.
- Press, W. H., Teukolsky, S. A., Vetterling, W. T. and Flannery, B. P., 1992, Numerical recipes in C: Cambridge Univ. Press.
- Robinson, E. A. and Silvia, M. T., 1981, Digital foundation of time series analysis: wave equation space-time processing: Holden-Day.
- Sheriff, R. E., 2002, Encyclopedic Dictionary of Applied Geophysics: Soc. of Expl. Geophys.
- Soubaras, R., 1996, Explicit 3-D migration using equiripple polynomial expansion and Laplacian synthesis: Geophysics, **61**, 1386-1393.
- , 2002, Comparison of Kirchhoff and wave-equation prestack migration on OBC data: 72nd Ann. Internat. Mtg., Soc. of Expl. Geophys., Expanded Abstracts, 1244-1247.
- Stoffa, P. L., Fokkema, J. T., de Luna Freire, R. M. and Kessinger, W. P., 1990, Split-step Fourier migration: Geophysics, **55**, 410-421.
- Thorbecke, J. W. and Rietveld, W. E. A., 1994, Optimum extrapolation operators - A

comparison: 56th Ann. Internat. Mtg. Eur. Assn. Geosci. Eng., P105.

Thorbecke, J. W., Wapenaar, C. P. A. and G., S., 2004, Design of one-way wavefield extrapolation operators, using smooth functions in WLSQ optimization: *Geophysics*, **69**, 1037-1045.

Valenciano, A. A., Biondi, B. and Guitton, A., 2002, Multidimensional imaging condition for shot profile migration: SEP-111, Stanford University.

Versteeg, R. and Grau, G., 1991, Practical aspects of seismic data inversion, the Marmousi experience: Proceedings of the 1990 EAGE Workshop on Practical Aspects of Seismic Data Inversion, 1-194.

Wapenaar, C. P. A., Fokkema, J. T. and Thorbecke, J. W., 1997, Inverse wavefield extrapolation revisited: Limitations of single- and multi-valued operators: 67th Ann. Internat. Mtg. Soc. of Expl. Geophys., 1509-1512.

Weyl, H., 1931, The theory of groups and quantum mechanics: Dover edition.

Zauderer, E., 1989, Partial differential equations of applied mathematics: John Wiley.